

Towards Mechanical Intelligence In Soft Robotics
Model-based Design of Mechanically Intelligent Structures

Chen, Qianyi

DOI

[10.4233/uuid:5ce04f3d-6a0a-4c7c-90b0-8babba7a4512](https://doi.org/10.4233/uuid:5ce04f3d-6a0a-4c7c-90b0-8babba7a4512)

Publication date

2025

Document Version

Final published version

Citation (APA)

Chen, Q. (2025). *Towards Mechanical Intelligence In Soft Robotics: Model-based Design of Mechanically Intelligent Structures*. [Dissertation (TU Delft), Delft University of Technology].
<https://doi.org/10.4233/uuid:5ce04f3d-6a0a-4c7c-90b0-8babba7a4512>

Important note

To cite this publication, please use the final published version (if applicable).
Please check the document version above.

Copyright

Other than for strictly personal use, it is not permitted to download, forward or distribute the text or part of it, without the consent of the author(s) and/or copyright holder(s), unless the work is under an open content license such as Creative Commons.

Takedown policy

Please contact us and provide details if you believe this document breaches copyrights.
We will remove access to the work immediately and investigate your claim.

Towards Mechanical Intelligence In Soft Robotics:

**Model-based Design of Mechanically
Intelligent Structures**

Qianyi Chen

陈芊屹



**Towards Mechanical Intelligence In Soft Robotics:
Model-based Design of Mechanically Intelligent
Structures**

Qianyi Chen

Delft University of Technology

Towards Mechanical Intelligence In Soft Robotics: Model-based Design of Mechanically Intelligent Structures

Proefschrift

ter verkrijging van de graad van doctor

aan de Technische Universiteit Delft,

op gezag van de Rector Magnificus Prof. ir. T.H.J.J. van der Hagen,

voorzitter van het College voor Promoties,

in het openbaar te verdedigen op Woensdag 30 April 2025 om 10:00 uur

door

Qianyi CHEN

Master of Traffic and Transportation Engineering,

Wuhan University of Technology, Wuhan, China

geboren te Henan, China

Dit proefschrift is goedgekeurd door de promotoren.

Samenstelling van de promotiecommissie:

Rector Magnificus	voorzitter
Prof. dr. ir. D.L. Schott	ME, Technische Universiteit Delft, promotor
Dr. J. Jovanova	ME, Technische Universiteit Delft, copromotor

Onafhankelijke leden:

Prof.dr.ir. P. Breedveld	ME, Technische Universiteit Delft
Prof.dr.ir. J.L. Herder	ME, Technische Universiteit Delft
Prof. Dr.-Ing. Paul Motzki	Saarland University
Prof. dr. Cecilia Laschi	National University of Singapore



This research presented in this thesis was supported by TU Delft and China Scholarship Council doctoral programme.

TRAIL Thesis Series no. T2025/10, the Netherlands Research School TRAIL

TRAIL

P.O. Box 5017

2600 GA Delft

The Netherlands

E-mail: info@rsTRAIL.nl

ISBN: 978-90-5584-365-7

Copyright © 2023 by Qianyi Chen

All rights reserved. No part of the material protected by this copyright notice may be reproduced or utilized in any form or by any means, electronic or mechanical, including photocopying, recording or by any information storage and retrieval system, without written permission from the author.

Printed in the Netherlands

Summary

Soft robotics, a multidisciplinary engineering field, emerged from the promise of flexibility and adaptability to execute tasks in unstructured environments. However, significant challenges still remain, including the conflict of stiffness and compliance, multifunctionality, and adaptive performance. The concept of mechanical intelligence, embedding intelligence directly into structures by design, presents an alternative way to address these limitations, alongside complex assemblies and control systems. To achieve mechanical intelligence, embodying smart materials into morphing structures offers a potential design approach. However, there is lack of comprehensive design framework to integrate multiple smart materials, stimuli, and structural design together to support the advancement of mechanical intelligence. Thus, research objective of this thesis is to develop a model-based design framework for mechanically intelligent morphing structures. This will enable smart materials to be embedded into soft robotics for execution of adaptive functions.

Smart materials hold significant potential for advanced engineering applications due to their ability to respond to external stimuli such as temperature, light, pressure, electric and magnetic field. These materials can exhibit a wide range of adaptable behavior enabling functionalities like variable stiffness and/or tailored deformation. However, the nonlinear nature of smart materials and their complex interplay with the environmental conditions pose challenges in accurately modelling this interaction. Modeling approaches can contribute to novel solutions by describing the nonlinear behaviors of smart materials. These insights lay the foundation for design frameworks that enable the design of mechanically intelligent structures.

A model-based design framework for design of mechanically intelligent morphing structures is proposed in this thesis. The framework integrates smart material properties, structural geometry, and external stimuli into modular "building blocks". These building blocks were proposed as the fundamental units for creating adaptive morphing structures. The numerical methods, including finite element method (FEM), discrete element method (DEM), and coupling method, are employed to simulate interactions between materials and external stimuli. Using this

framework, a conceptual design for variable stiffness bending building blocks was developed. By incorporating rigid particles or smart hydrogels, these bending building blocks are capable of reversible deformations and varying stiffness. The findings show that larger bending angles in the rigid particle-based design are achieved by increasing the particle diameter ratio and membrane stiffness, while in the hydrogel particle-based design, larger bending angles are achieved by adding more particle layers or decreasing membrane stiffness. Additionally, the rigid particle-based design allows for a six-fold stiffness increase. For the hydrogel-based design, when combined with low melting point alloy strips, a twenty-fold stiffness increase was demonstrated.

Building on the conceptual design, the integration of multiple smart materials into a single building block is developed through the model-based design framework, enabling the morphing structure to exhibit self-actuation and adaptive behavior. By combining pH-sensitive hydrogels and shape memory polymers (SMPs), the building blocks are assembled into a morphing structure. In this morphing structure, self-actuation is triggered by an increase in pH, while stiffness is enhanced by lowering the temperature. The structure is capable of a variety of deformations, including bending, curling, and elongation, with the geometric parameters of the SMP frame playing a significant role in these behaviors. Moreover, when the SMP transitions to its glassy state, the bending stiffness increases by a factor of ten compared to its rubbery state.

Building on the design of multiple smart materials, an integrated system has been developed to enable collaborative operation by embedding a thermal control system into a shape memory materials-based structure. This system allows for coordinated responses to the same external stimulus. The structure, which features shape memory alloy (SMA) springs and an SMP frame, achieves self-actuation and stiffness variation through the shape memory effects. The embedded thermal control system enables the materials to actuate in response to temperature changes, allowing the morphing structure to perform a variety of actions with consistent operation. Using this integrated system, the morphing structure can undergo a sequence of motions, including bending, stiffness enhancement, and recovery, all within a continuous 110-second cycle.

In conclusion, the proposed model-based design framework shows feasibility for developing mechanically intelligent morphing structures. The framework systematically integrates smart materials and structural geometries into the morphing structures actuated by external stimuli, enabling self-actuation and adaptive functionality. Furthermore, the synchronized operation of the integrated system enhances the potential for practical applications of mechanically intelligent morphing structures in the field of soft robotics. Future work should focus on improving accuracy of the numerical modeling, and developing dynamic control system for stability. Additionally, fatigue analysis is essential for improving the durability in industrial applications.

Content

Summary	i
1 Introduction	1
1.1 From soft robotics to mechanical intelligence.....	1
1.2 Problem statement	3
1.3 Research objective and scope	4
1.4 Research questions	5
1.5 Outline of the thesis.....	5
2 State-of-the-art of smart materials in classification, properties, and modeling approaches*	9
2.1 Robotic materials that move: overview of smart materials	10
2.2 Types of smart materials.....	10
2.2.1 Classification of smart materials.....	11
2.2.2 Mechanism of smart materials.....	11
2.3 Modeling of smart materials.....	18
2.3.1 Modeling methods	18
2.3.2 Constitutive models for smart materials	22
2.4 Potentials of the model-based design for mechanically intelligent structures.....	31
2.5 Conclusion.....	32
3 Model-based design framework for mechanically intelligent morphing structure*	35
3.1 Introduction	36

3.2 Design process based on building blocks	37
3.3 Methodology.....	37
3.3.1 FEM model	38
3.3.2 FEM-DEM model.....	40
3.3.3 FEM-MBD model.....	41
3.4 Case study.....	42
3.4.1 Smart materials and smart mechanism building blocks.....	42
3.4.2 Multiple smart materials based building blocks	44
3.5 Conclusion.....	46
4 Conceptual design of variable stiffness soft bending building blocks*	47
4.1 Introduction	48
4.2 Conceptual design of the smart building blocks.....	49
4.2.1 Theoretical background	49
4.2.2 Building blocks design.....	50
4.3 Methodology.....	55
4.3.1 FEM-DEM model and implementation	56
4.3.2 FEM model and implementation	60
4.4 Results and discussion.....	63
4.4.1 Sensitive analysis of rigid particle-based building block	63
4.4.2 Sensitive analysis of smart hydrogel particle-based building block.....	70
4.5 Conclusion.....	77
5 Model-based design of a mechanically intelligent morphing building block by multiple materials*	79
5.1 Introduction	80
5.2 Methodology.....	81
5.2.1 The pH-sensitive hydrogel modeling.....	81
5.2.2 SMP modeling	83
5.2.3 Simulation setup	84
5.3 Mechanical intelligent structure design and validation.....	85
5.4 Results and discussion.....	86
5.4.1 Case studies: bending, curling and elongation structures.....	86
5.4.2 Stiffness variation of the morphing structure.....	91
5.5 Conclusion.....	92

6 Integrated system design of the collaborative smart materials in a building block*....	95
6.1 Introduction	96
6.2 Design of the building block and integration system	97
6.2.1 Structural design	97
6.2.2 Control circuit design.....	98
6.3 Methodology.....	99
6.3.1 Numerical modeling	99
6.3.2 Experimental setup	101
6.3.3 Sensing and control algorithm	102
6.4 Results and discussion.....	105
6.4.1 Verification of the control system and motions of morphing structure	105
6.4.2 System Initialization and Standby Mode	106
6.4.3 Analysis of working modes.....	107
6.5 Conclusion.....	109
7 Conclusions and Recommendations	111
7.1 Conclusions	111
7.2 Recommendations	114
Bibliography	117
Nomenclature.....	135
Acknowledgements.....	137
Curriculum Vitae.....	139
Samenvatting	141
TRAIL Thesis Series	145

1 Introduction

1.1 From soft robotics to mechanical intelligence

Traditional rigid robots face challenges when it comes to flexibility, safety, and versatility in dynamic unstructured environments. The rigid structures they are made of, limit their ability to handle fragile objects or to interact with unpredictable surroundings without causing damage. Additionally, their limited number of degrees of freedom decreases their performances for tasks requiring flexibility or shape change [1]. The emergence of soft robotics, constructed from soft materials with Young's modulus ranging from 10^4 to 10^9 Pascals, offers potentials to address these challenges. Soft robotics is a branch of robotics that designs flexible, compliant systems to safely interact with dynamic environments or various of different objects [2]. As shown in Figure 1.1, soft robots can deform continuously with enhanced flexibility, which has promised to execute tasks in unstructured environments, such as grasping irregular or fragile objects in offshore, logistics or agriculture engineering, and exploration or interaction in underwater scenarios [3]. However, broad acceptance in real world commercial applications has not been achieved due to the lack of design tools and challenges in manufacturing [4, 5].

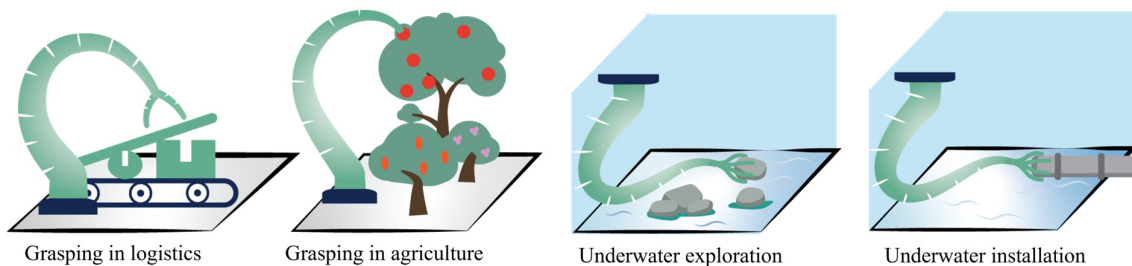


Figure 1.1 Potential applications of soft robotics

The first key challenge is to combine stiffness with adaptability. Soft robots produce output forces that are less than one-tenth of those generated by similarly sized rigid robots [2]. This limitation comes from the low stiffness of soft actuators. However, increasing stiffness to enhance force output typically reduces flexibility [6, 7]. Thus balancing stiffness and flexibility

to achieve adaptive performance remains a key obstacle for soft robots. The second key challenge is utilizing the soft materials. Although soft materials allow soft robots to deform freely and perform complex movements, it complicates the execution of tailored deformations [8].

Soft robotics allows to implement mechanical intelligence, enabling them to adapt to complex tasks. Thus, embedding advanced mechanical intelligence into soft robotics to address the challenges. In terms of soft robotics, mechanical intelligence refers to the adaptive behaviors that come from the interactions between the body and the environment, reducing the need for sensing or control systems. This concept emphasizes the robot's ability to respond to external stimuli through its material properties, structural design, and morphology, enabling the adaptation to changing conditions [9-11]. Mechanical intelligence enables structures to exhibit different deformations and variable properties. These can be achieved by using the mechanical design or existing properties that change in response to conditions, without relying on external systems [10, 12, 13]. For instance, a standard soft robotic gripper displays mechanical intelligence if it can adapt its shape to different objects without affecting its functional performance. The development of mechanical intelligence relies on the combination of complex geometry and smart materials, i.e. a complex geometry can form the foundation of morphing structure, while smart materials can support the actuation process.

Morphing structures, illustrated in Figure 1.2, are structures designed to change shape in a required and reversible manner, enabling different functionalities [14]. Morphing structures can change into different shapes that enable soft robots to adapt for different tasks. However, morphing structures are actuated typically by an external driving component [15]. Thus, to equip morphing structures with mechanical intelligence, the required functions of self-actuation need to be embedded, which achieves active responses and behaviors by environment change or external stimuli without the need for external driving components.

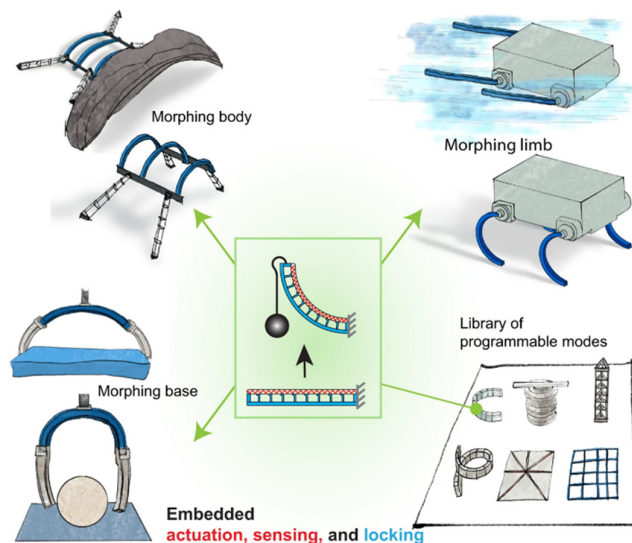


Figure 1.2 Morphing structures with variable functionalities [14]

To achieve variable stiffnesses and allow morphing structures to reconfigure on their own, integrating smart materials into the morphing structure is a strategy to embed mechanical intelligence into soft robotics. Smart material is defined as responsive material that can significantly change properties by external stimuli, including pH value, temperature, electricity, magnetic fields, light, humidity, or chemical reactions [16-20] (cf. Figure 1.3). This allows smart material actuating the morphing structure, while the responsiveness to external stimuli offers the potential for self-actuation. However, soft robotic designs require the integration of multiple types of smart materials embedded into designed morphing structures to achieve variable deforming modes.

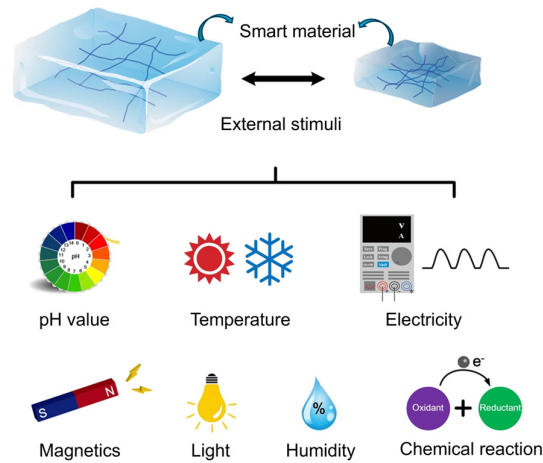


Figure 1.3 Illustration of smart materials triggered by various stimuli

Given the complexities of designing mechanical intelligence embedded soft robotic systems with morphing structures and smart materials, model-based design provides an alternative to physical experimental trial and error prototyping. Model-based design relies on creating mathematical or computational representations of the soft robotics, enabling visualizing the overall structure and predictions of its performance [21]. Model-based are based on developing numerical models to evaluate smart materials simultaneously. Current research mainly focuses on two aspects, one is explaining the constitutive models of smart materials to describe the nonlinear properties, the other is to predict the performance of smart materials embedded flexible structures [22, 23]. However, there is no comprehensive model-based design framework that can integrate multiple smart materials and external stimuli to support the design of morphing structures. Thus, an integrated design framework is needed to develop mechanical intelligence, which enables to investigate the interactions between (multiple) smart materials, (multiple) structures, and (multiple) stimuli.

1.2 Problem statement

Embedding mechanical intelligence into soft robotics can enhance the adaptability to complex tasks. In addition, the model-based design framework shows potential for developing mechanically intelligent structures. However, there are still challenges to be addressed to create and improve the mechanical intelligence:

- (1) Modeling smart material actuating morphing structures for tailored deformations is challenging due to the requirements of adaptation to geometric structures and the response of smart materials to diverse conditions. Thus, a comprehensive model-based design strategy is needed for supporting the design process to apply the smart materials to actuate the morphing structures achieving mechanical intelligence.
- (2) Morphing structures still face the challenge of balancing stiffness and flexibility. Thus, developing mechanically intelligent morphing structures that not only enable adaptable deformations, but also provide variable stiffness are needed to broaden the range of applications for soft robots.
- (3) The absence of an integrated framework for combining multiple smart materials within a single morphing structure limits the achievement of multiple functionalities. Thus, an integration system is needed to develop the adaptive morphing structures actuated by multiple smart materials as the embedded mechanical intelligence for soft robotics with multiple functionalities.

1.3 Research objective and scope

To address the challenges outlined in Section 1.3, the objective of this research is to establish a model-based design framework that incorporates mechanical intelligence. This framework integrates smart materials and morphing structures into mechanical intelligence design, enabling self-actuation and improved adaptability. The study focuses on creating a practical and achievable framework and develop embedded mechanical intelligence, with the assumptions and limitations defined as:

- (1) This study will employ existing modeling approaches and coupling methods to develop the model-based design framework. Thus, developing new modeling methods are not in the scope of this thesis.
- (2) The study emphasizes the mechanical behavior of novel morphing structures, excluding material-specific attenuation factors and optimization processes for practical applications.
- (3) The design framework is developed for structures ranging from millimeters to meters in scale. Phenomena or interactions occurring at smaller scales, such as nano-scale interactions, are outside the scope of this research.
- (4) Mechanical intelligence holds the potential to achieve fully self-actuating systems powered entirely by natural stimuli, which requires integrating multiple disciplines such as control, sensing, biology, and materials science. However, this study focuses only on exploring mechanically intelligent behaviors triggered by external stimuli in a controllable laboratory setting. Thus, the stimuli used in this research are sourced from human intervention rather than directly from natural environmental inputs.

1.4 Research questions

Based on the research objective, the main research question is stated:

How to develop a model-based design framework for integrating mechanically intelligent morphing structure into soft robotics?

To answer the main research question, the following four sub-questions are addressed in this thesis.

Q1: What is the state-of-the-art of smart materials? How are they classified, what are their properties and how are they modeled?

Q2: How can smart materials be applied into the development of a model-based design framework?

Q3: How can the model-based design framework be utilized to design mechanically intelligent morphing structure?

Q4: How can the morphing structure achieve self-actuation by integrating multiple smart materials?

Q5: How to develop an integrated system with multiple smart materials to respond collaboratively to the same stimulus, enabling multifunctionality for mechanical intelligence?

1.5 Outline of the thesis

The outline of this dissertation is shown in Figure 1.4. The chapters are related to research questions and the main contents (Chapter 2-6) consist of two aspects considering the model-based design framework of mechanically intelligent morphing structures. The first aspect (Chapter 2-4) elaborates the model-based design strategy and conceptual designs of the mechanical intelligence involving modeling approaches, geometry structures, and smart materials. Based on this, the second aspect (Chapter 5 and Chapter 6) develops the mechanical intelligence with multiple functionalities applied on soft robotics.

Chapter 2 reviews the state-of-the-art in smart materials. First, different types of stimuli are specified to classify different smart materials. Second, the properties of different smart materials are summarized for different applications. In addition, the modeling methods used to describe the smart materials properties are evaluated and analyzed, and the potential modeling approaches that can be used in a model-based design framework are proposed.

Chapter 3 builds the model-based design framework, this framework supports to develop the morphing structures embedding mechanical intelligence. Utilizing the results in Chapter 2, this chapter integrates smart materials' properties, external stimuli, and modeling approaches into the design process to establish the model-based design framework. Additionally, the concept of a "building block", which is a modular unit combining structural geometry, smart materials, and external stimuli, is introduced to finalize the framework tailored specifically for mechanical intelligence.

Chapter 4 utilizes the model-based design framework to construct the building block for developing the mechanically intelligent morphing structures. Initially, a conceptual design of a bending building block is developed based on the model-based framework, enabling different bending configurations. Then, using similar conceptual structure, the smart hydrogels combined with variable stiffness layers is developed to achieve both bending deformations and stiffness variation.

Chapter 5 builds on the results of Chapter 4 and expands to the multiple smart materials building block. Rather than only relying on smart hydrogel, this chapter combines a pH-sensitive hydrogel with a shape memory polymer (SMP) frame to create the building block. By assembling the building blocks and using different stimuli conditions, the morphing structures are constructed that achieve tailored deformations by self-actuating process.

Chapter 6 combines multiple smart materials to work collaboratively within the same external stimulus. Building on the Chapter 5, this chapter incorporates shape memory polymer (SMP) and shape memory alloy (SMA) to create a functional building block. An integration system is developed by combining this building block with a temperature control system. The integration system is evaluated by analyzing different deformations and stiffness variations via self-actuation.

Chapter 7 presents the overall conclusions and future outlooks.

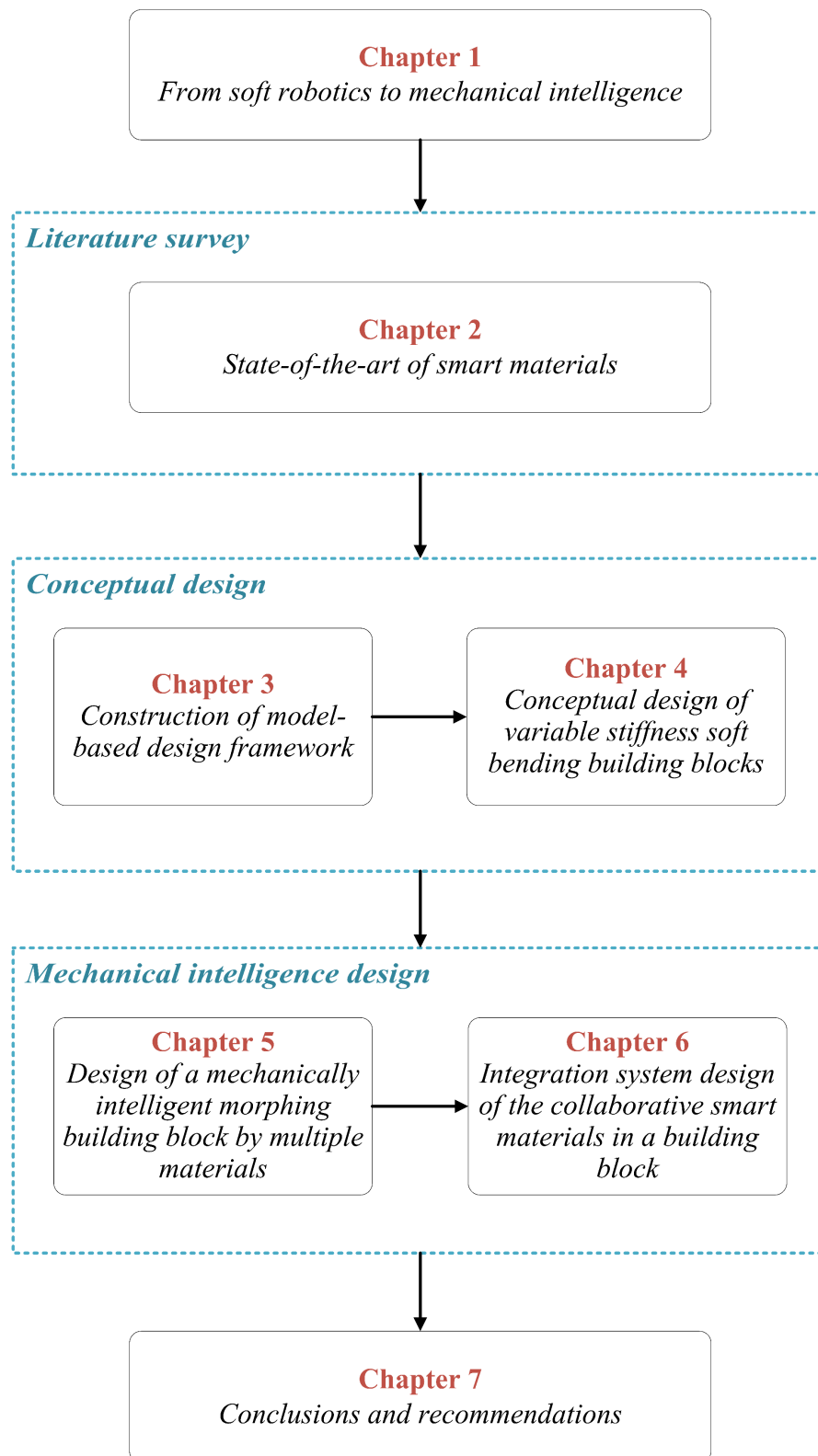


Figure 1.4 Outline of this dissertation

2 State-of-the-art of smart materials in classification, properties, and modeling approaches*

Smart materials are upcoming in many industries due to their unique properties and wide range of applicability. These materials have the potential to transform traditional engineering practices by enabling the development of more efficient, adaptive, and responsive systems. However, smart materials are characterized by nonlinear behavior and complex constitutive models, posing challenges in modelling and simulation. Therefore, understanding their mechanical properties is crucial for model-based design. To utilize smart materials, this chapter comprehensively reviews the current state-of-the-art of smart materials from different aspects. Section 2.1 gives a general definition and description of smart materials. Section 2.2 summarizes various types of smart materials and their properties. Section 2.3 analyzes the existing numerical methods used to describe the nonlinear properties for these smart materials. This analysis is crucial as understanding nonlinear behavior is often key to accurately predicting the performance of smart materials in practical applications. Section 2.4 discusses the potentials of model-based design framework based on smart materials. Section 2.5 concludes the classification, properties, and modeling approaches of smart materials.

* This chapter is based on Q. Chen, T. Kalpoe, and J. Jovanova, “Design of mechanically intelligent structures: Review of modeling stimuli-responsive materials for adaptive structures,” *Heliyon*, 2024 (10), 14, e34026. DOI: 10.1016/j.heliyon.2024.e34026

2.1 Robotic materials that move: overview of smart materials

Smart materials are increasingly attracting the attention of researchers due to their unique properties, offering significant potential for advanced engineering applications. These materials have unique properties that allow them to adapt to changes in their environment. This adaptability makes them highly useful in many different applications [24]. Smart materials have emerged as a revolutionary force, offering unprecedented possibilities for innovation and advancement in many fields from aerospace and automotive engineering to electronics and biomedical devices [25-30]. Smart materials have evolved into a needed aspect for a variety of structures due to their ability to adapt and modify their properties when subjected to external stimuli [31]. Unlike conventional materials, with fixed characteristics, smart materials can undergo reversible or irreversible changes in their physical or mechanical properties, enabling them to perform specific functions or tasks autonomously [32]. External stimuli including pH, stress, temperature, electric voltage and magnetic field can result in a change of size, viscosity or color [33, 34]. Hence, the aforementioned parameters can be used to achieve tailored functions of the smart material's applications, such as sensors, actuators and medication delivery [35-37]. These materials have the potential to transform traditional engineering practices by enabling the development of more efficient, adaptive, and responsive systems [38]. Nevertheless, smart materials have several aspects which can be improved upon. The performance of these materials is susceptible to environmental conditions, some materials have a specific activation range and can not always function as efficiently when needed. Furthermore, durability issues with degradation and fatigue can reduce their lifespan. Additionally, these materials are often expensive due to their complexity in production and the need for specialized raw materials. Lastly, the implementation of these materials in existing systems can be challenging, requiring specialized expertise and has the potential for improvement with further research [24, 39, 40]. Therefore, the successful design and implementation of smart materials require a comprehensive understanding of their complex behavior. Model-based design relying on solid modeling, finite-element analysis and optimization provides a potential solution, which makes the corresponding material and structure geometry selection easier [41]. Smart materials are meticulously modelled with advanced software tools suited for numerical simulations, facilitating the utilization of constitutive equation-based models [42]. Depending on the complexity of the model and various other considerations, such as the material's mechanical properties, these models are tailored to accurately describe nonlinear behaviors of smart materials [43, 44].

2.2 Types of smart materials

Materials fulfil different roles for several applications while taking costs and environmental influences into consideration. With aspects such as efficiency, innovation and safety being more prominent than ever before, smart materials are needed [45].

2.2.1 Classification of smart materials

Smart materials, also known as intelligent or responsive materials, are materials that exhibit adaptive or dynamic properties in response to external stimuli such as temperature, light, pressure, electric fields, or magnetic fields [46, 47]. These materials can be classified into several categories based on their underlying mechanisms and functionalities. The inner workings of smart materials are mimicking biological systems [48]. Smart materials gather information from their surroundings by sensing and creating chemical or physical effects for brain decision-making control. Smart materials are classified to provide a systematic framework for understanding and categorizing their unique properties and behaviors. Classification allows researchers and engineers to organize and differentiate smart materials based on their stimuli or response types, enabling a clearer understanding of their capabilities and potential applications. By categorizing smart materials, specific applications are achievable by tailoring the design and optimizing the performance of smart materials. Moreover, the classification of smart materials facilitates knowledge sharing and collaboration within the scientific community, for establishing a common language and reference point to understand smart materials. The most significant distinction made in smart materials is between the main classes ‘active’ and ‘passive’. Passive smart materials are responsive to external stimuli but do not actively generate a response. Instead, their properties change passively in reaction to specific environmental conditions. Passive materials can transfer energy, for instance when used as fiber optic [49]. However, while being ‘smart’ they do not possess the characteristics to transduce energy. They are mostly used to function as a sensor instead of an actuator or transducer [50]. Subsequently, active materials can change their characteristics when exposed to external effects. Furthermore, some of the active smart materials can convert energy from one form such as thermal, mechanical or chemical to another form. Active smart materials possess some properties which distinguish them from other materials such as immediacy: short response time, self-actuation: form and shape can be changed due to external stimuli, self-diagnostic: imperfections or cracks can be detected and self-healing: materials can repair themselves when damaged.

2.2.2 Mechanism of smart materials

The main types of smart materials will be listed and elaborated on briefly in this section.

2.2.2.1 Piezoelectric Materials

Piezoelectric materials generate an electric charge when subjected to mechanical stress and, conversely, undergo deformation when an electric field is applied [51]. For a material to exhibit piezoelectric behavior, the material needs to be dielectric, meaning nonconducting and without a center of symmetry in the structure [52]. When an electric charge/voltage is applied as the response to mechanical forces/pressures, this is called the direct piezoelectric effect. In addition, when an electric charge is applied and leads to deformation, it is called the inverse piezoelectric field. Similarly, piezoelectric actuators can convert electrical signals into mechanical motions which is used commonly in the automotive industry. For instance in lenses and positioning of mirrors. They are also used in sensors and energy harvesting devices, such as flexible piezoelectric devices [53-56]. Potential improvements for these materials can be found in their brittleness, many piezoelectric materials are ceramic, which are prone to cracking. Additionally,

improving their performance under high temperatures could lead to more robust and reliable applications [57, 58].

2.2.2.2 Photostrictive Materials

Photostrictive materials undergo mechanical deformation when exposed to light. These materials use the combined effects of piezoelectric and photovoltaic properties present in the material. Through the photovoltaic effect, these materials produce an electric charge when exposed to light, and the piezoelectric effect causes strain or deformation [59, 60]. One of the most commonly studied photostrictive materials is BaTiO₃ [61]. These materials have a distinct advantage of wireless actuation since no external electrical power sources are needed to cause mechanical changes. This makes these materials highly suitable for applications with remote control, such as microelectrochemical systems (MEMS), solar energy harvesting, actuators and optomechanical devices [62-64]. Photostrictive materials present opportunities for enhancement in efficiency and environmental resilience. Further research could focus on improving their performance under prolonged exposure to light and varying environmental conditions [65].

2.2.2.3 Electrostrictive Materials

Electrostrictive materials are a category of smart materials that experience a change in shape or size when subjected to an electric field [66]. This phenomenon, known as the electrostrictive effect, occurs due to the alignment of electric dipoles within the material under the influence of the electric field. As the dipoles align, the material undergoes mechanical strain, resulting in the dimensions changing [67]. One of the key characteristics of electrostrictive materials is the ability to respond rapidly to changes in the applied electric field. The precision and responsiveness of electrostrictive materials enable the development of advanced devices in robotics, aerospace, and biomedical engineering, including actuators, sensors, and tunable lenses [68-70]. Electrostrictive materials face difficulties in non-linearity, the response of these materials is often not linear. This makes control very hard in potential applications. Furthermore, hysteresis during operation can lead to energy losses, which leads to lower efficiencies [71, 72].

2.2.2.4 Magnetostrictive Materials

Magnetostrictive materials are a class of smart materials that exhibit mechanical deformation in response to changes in magnetic fields [73]. This phenomenon, known as the magnetostrictive effect, is characterized by the alignment and reorientation of magnetic domains within the material, leading to changes in its shape or size. Terfenol-D, comprised of terbium, dysprosium, and iron, stands as a prominently utilized magnetostrictive material [74]. Terfenol-D demonstrates significant magnetostrictive properties, making it a popular choice for various applications, including high-precision actuators, sensors, and vibration energy harvesters [75]. Magnetostrictive materials offer several advantages, such as high force output, fast response times, and excellent energy conversion capabilities. These properties make them ideal for applications where precise and efficient motion control is required, such as in robotics and adaptive structures [76]. There are opportunities to improve these materials by addressing the formation of eddy currents at high frequencies, which can impede the excitation of the material core. Additionally, enhancing circuit design can help manage current leakage and demagnetization more effectively [77, 78].

2.2.2.5 *Thermoelectric Materials*

Thermoelectric materials are a class of smart materials that can convert heat into electricity or vice versa [79]. These materials exhibit the thermoelectric effect, where a temperature gradient across the material generates an electric potential, leading to the conversion of heat energy into electrical power [80]. The thermoelectric effect relies on the unique properties of thermoelectric materials, such as high electrical conductivity combined with low thermal conductivity. This combination allows them to efficiently transport electric charge while impeding the flow of heat, resulting in the creation of a temperature difference when one side of the material is exposed to heat [81]. Thermoelectric materials have gained significant attention in various applications due to their ability to harness waste heat and convert it into useful electrical power. They have potential uses in powering electronic devices, remote sensors, and even generating electricity from industrial processes or automotive exhausts [82-84]. Thermoelectric materials have the potential for an expanded operating range. Further research into the use of alloys could significantly enhance this aspect [85, 86].

2.2.2.6 *Electrochromic Materials*

Electrochromic materials are a category of smart materials that undergo reversible changes in their optical properties when subjected to an electrical stimulus [87, 88]. These materials are particularly desirable for applications such as smart windows, displays, and privacy glass because they can change color or transparency in response to an applied voltage or current [89]. Electrochromic devices usually include several layers, including an electrochromic layer, an ion-conducting electrolyte, and electrodes. When an electric potential is supplied, ions migrate within the electrochromic layer, causing its optical characteristics to alter [90]. Electrochromic materials' capacity to alter light transmission and reflection makes them energy efficient and adaptable, allowing them to provide benefits such as customizable shade, glare reduction, and privacy options in a variety of industries [91, 92]. These materials offer opportunities for enhancement by expanding the range of compatible materials. Additionally, increasing the spectrum of available colors would benefit applications requiring diverse colors, such as displays. Further research into hybrid materials could also improve their efficiency and compensate for their shortcomings [93, 94].

2.2.2.7 *Photochromic Materials*

Photochromic materials are a form of smart material that change their optical characteristics when exposed to light [95]. These materials can change color or transparency when exposed to specific light wavelengths, making them valuable for applications like photochromic lenses, eyeglasses, and smart windows [96]. The presence of photochromic molecules inside the structure of photochromic materials is responsible for their behavior. When these molecules absorb photons, they undergo a reversible chemical rearrangement, resulting in a change in their electronic configuration and a visible change in color or transparency [97]. The primary advantage of photochromic materials is their ability to flip between different optical states in real-time. They enable automatic light adaptation by darkening when exposed to direct sunlight and reverting to their former condition when the intensity of the light drops [98]. Typically, chromic materials exhibit sensitivity to both visible and ultraviolet light, with color variations contingent upon the intensity of the respective radiation spectrum. A prominent drawback of

photochromic applications is poor durability and endurance. Free radicals produced by exposure to UV light play a big role in the degradation of these devices. Coatings could improve durability and provide protection to these devices [99, 100].

2.2.2.8 Hydrogel

Hydrogels are three-dimensional networks of polymer chains that can absorb and retain large amounts of water or other solvents. As smart materials, they exhibit significant swelling or shrinking in response to environmental factors such as temperature, pH, light, or the presence of certain chemicals [101]. Instead of making use of the Shape Memory Effect (SME), hydrogel makes use of the Shape Change Effect (SCE). This effect takes place when switching between two states is instant, or close to instant. Hydrogels may form via diverse physical interactions or chemical reactions, contingent upon the specific application requirements [102]. For example, a majority of hydrogel that exists of poly(*n* isopropylacrylamide) (PNIPAM) can swell and shrink in water due to temperature variations [103]. Even under pressure, the absorbed water can almost not be removed. Due to this property hydrogels are widely utilized in different fields. For instance, photo-responsive hydrogels are used to mimic the changing nature of biomechanics in living tissues [104]. Recently hydrogels have been used in electronics and electronic devices [105]. Hydrogels have applications in drug delivery, tissue engineering, and soft robotics [106-109]. Furthermore, they are used as gel actuators, water-blocking tape in the field of biochemicals or agriculture engineering [110-112]. Key improvements can be made to make the material less highly sensitive to environmental conditions, reducing the altering of the properties of hydrogel. Further research could also be performed to reduce the deterioration, which is caused by repeated cycles of swelling and shrinking [113].

2.2.2.9 Shape Memory Materials (SMMs)

SMMs have the ability to “remember” their original shape and recover it when subjected to certain stimuli such as heat, stress, or magnetic fields, this mechanism is also known as the SME [114]. SMMs are one of the most commonly used intelligent materials for industrial purposes. SMMs have a lot of common groups such as shape memory Alloys (SMAs), shape memory polymers (SMPs) and shape memory ceramics (SMCs) [115, 116].

(1) Shape Memory Alloys (SMAs)

One of the common groups of SMMs is SMAs. These are metallic alloys with mechanical properties that alter with temperature. When heated, they revert to their previous shape by transitioning between stable crystalline phases such as martensitic or austenitic [117]. At high temperatures, the crystalline structure of the material is densely packed, having a hexagonal lattice (austenite). While at low temperatures, the structure is more loose having a body-centered lattice resulting in Martensite. SMAs have two distinct features, one being the SME and the other one being superelasticity (SE). Due to SE, the alloys can endure large strains, up to 8-10%, and still recover their original shape [118]. This effect happens at high temperatures and this results in the storage of energy. SME on the other hand provides motion and force. Looking at the reversibility of the SME, two common groups of SMAs can be found. The first one is a one-way SME and the other one is a two-way SME. The one-way SMAs have deformed to an irreversible state and the two-way SMAs are able to return to the original shape [119]. Nickel-titanium or copper-based alloys are commonly used to make SMAs. Few applications

of SMAs can be found in industrial engineering [120]. SMAs are utilized to strengthen concrete beams in structural applications to decrease damage caused by corrosion, fire or mechanical loads [121]. In the aerospace sector, SMAs could be potentially used as sensors and controls [122]. In the marine industry, SMAs can be used in the shipyard for manufacturing and combining pipes [123]. Furthermore, applications can be found in the biomedical field as dental diagnosis or neurosurgical stents [124, 125]. Yet, SMAs also face difficulties in their potential applications. One of the biggest improvements can be made in the high costs associated with SMAs made from nickel-titanium, they are expensive and difficult to manufacture.

(2) Shape Memory Polymers (SMPs)

A specific type of SMM is the SMP. SMPs maintain a permanent shape at room temperature, when exposed to a higher transition temperature they deform. After cooling down, the initial shape/form is obtained. Currently, the SME can be activated in SMPs by essentially three types of external stimuli, which consist of heat (thermo-responsive SMPs), chemicals (chemo-responsive SMPs) and the last one being light (photo-responsive and photo-thermal responsive SMPs) [126]. However, most SMPs are thermally responsive [127]. Currently, many studies have been conducted on one-way, two-way and multiple SMPs [128]. The first kind, one-way, can be traced in conventional crosslinked polymers [129]. Two-way SMPs are also known as reversible SMPs. This term refers to polymers which can deform at high temperatures and return between two shapes at low temperatures. The last of the three SMPs, multiple SMPs, are polymers which are able to memorize more than one temporary shape. The multiple-shape memory phenomenon enables the polymer to switch between different shapes by programming [130]. Applications are mostly affiliated with heat-shrinkable objects, such as heat-shrinkable tubes or labels. Examples of more high-tech devices include self-deployable hinges or biomedical devices, such as smart surgery devices [131, 132]. SMPs allow for more deformation compared to SMAs, lower costs, tunable stiffness and ease of fabrication. Recently, the mechanical properties have been improved enormously due to the reinforcement with other materials, leading SMPs to gain more attention. Furthermore, new research on the effect of printing parameters on SMPs has been conducted, leading to a broader aspect for future applications [133].

Additionally, another aspect of printing SMPs worth mentioning is the rise of 4D printing, which is an advanced Additive Manufacturing (AM) process [134]. It is the process of a 3D-printed object is capable of changing or modifying its structure due to external influences, such as light or temperature. Therefore making smart or stimuli-responsive materials one of the most important components needed for 4D printing [135]. The big difference with standard 3D printing is that a new function is added to change shape over time. Making the structure capable of self-healing. For instance, in the case of a damaged pipe, the structure possesses the ability to self-heal. A specific example would be, the 4D printing of polyvinyl chloride (PVC) with good shape memory effects [136]. Another example would be self-assembling. This could take place when small components are moved through tiny holes in the human body, the structure will be able to assemble later for medical purposes when needed [137-139]. Nevertheless, SMPs are associated with lower structural properties, such as their mechanical strength. Therefore, incorporating a second material or creating a composite is often beneficial for most applications.

(3) Shape Memory Ceramics (SMCs)

The last common group of SMMs are SMCs. They provide many advantages compared to metallic alloys, such as higher strength and higher operating temperatures [140]. SMCs are less likely to degrade due to creep and oxidation at higher temperatures than SMAs. Compared to SMAs a higher actuation stress and strain can be exhibited, with a bigger transformation temperature range. Shape memory behavior is seen by a reversible martensitic phase transformation. Out of the current SMCs, ceramics based on zirconia (ZrO_2) have gained a lot of interest, due to the similarity to SMAs regarding thermo-mechanical capabilities [45, 141]. Ceramics that are zirconia-based consist of the largest family of SMCs with shape memory behavior and mechanisms similar to SMAs [142]. Brittleness of SMCs can still be improved, since this would make the material more suitable for potential applications. Further research could also find a solution for the activation energy needed for SMCs, which is higher than for other SMMs.

2.2.2.10 Electro-Rheological Fluids and Magneto-Rheological Fluids

Electro-rheologic fluid (ERF) is a type of material that exhibits changes due to its ‘flow behavior’ impacted by an applied electric field [143]. When an electric field is applied to a suspension of minuscule particles in an electrically insulating fluid, they rapidly form a structure which is similar to a solid, aligned in the direction of the electric field [144]. Depending on the application of the electric field, the initial state can be obtained such as gel or liquid, making it undergo rapid changes in viscosity [145]. ERFs can be very stiff, they have a high dielectric constant, and varying damping coefficient depending on the field and interfacial bond strength. ERFs are applied in vibration isolators, in automotive applications such as the clutch of shock breakers. In addition to this, they are also utilized in base-isolation for buildings and electro-active actuators, due to their ability to overcome imperfections caused by sedimentation and particle aggregation [146].

Electro-rheologic fluid (ERF) is a type of material that exhibits changes due to its ‘flow behavior’ impacted by an applied electric field. When an electric field is applied to a suspension of minuscule particles in an electrically insulating fluid, they rapidly form a structure which is similar to a solid, aligned in the direction of the electric field. Depending on the application of the electric field, the initial state can be obtained such as gel or liquid, making it undergo rapid changes in viscosity. ERFs can be very stiff, they have a high dielectric constant, and varying damping coefficient depending on the field and interfacial bond strength. ERFs are applied in vibration isolators, in automotive applications such as the clutch of shock breakers. In addition to this, they are also utilized in base-isolation for buildings and electro-active actuators, due to their ability to overcome imperfections caused by sedimentation and particle aggregation [146]. Magneto-rheologic fluid (MRF) is a type of smart material that exhibits changes in its rheology due to the application of a magnetic field. MRFs are two-phase composites consisting of solid particles which are magnetically polarizable and that are suspended in a non-magnetic medium. Once the magnetic field is turned on or applied, the materials transition from a Newtonian fluid to a solid state [147]. Due to this MRFs are also known as magneto-sensitive smart materials. Just like ERFs, MRFs were used commonly as dampers, buffers and clutches in the automotive industry. Specifically, MREs are still used regularly in vibration absorbers [148]. In recent years,

MRFs are largely used for finishing purposes in the manufacturing industry. MRFs combined with abrasive particles are used as a finish, since using fluid is an efficient method to achieve manipulation [149]. MRFs are similar to ERFs with varying viscosity depending on the field applied. The viscosity when a magnetic field is applied, is several orders higher than in its fluid state [150, 151]. One area for enhancement in these rheological fluids is their tendency to thicken over time, necessitating periodic replacement. Additionally, their high density presents an opportunity to innovate towards more lightweight applications [152].

Table 2.1 Smart material types with respective inputs and outputs

Material	Input	Output
Piezoelectric	Electric field	Mechanical strain
	Mechanical load	Electric potential
Photostrictive	Incident light	Mechanical strain
Magnetostrictive	Magnetic field	Mechanical strain
	Mechanical load	Magnetization
Electrostrictive	Electric field	Mechanical strain
	Mechanical load	Electric potential
Thermoelectric	Thermal load	Electric potential
	Electric field	Electric potential
Shape memory materials	Thermal load	Temperature change
	Magnetic load	Mechanical strain
Photovoltaic	Incident light	Electric potential
Magneto- rheological fluids	Magnetic field	Mechanical strain
Electro- rheological fluids	Electric field	
Photo- chromic	Incident light	
Thermo- chromic	Thermal load	
Magneto- chromic	Magnetic field	Color change
Electro- chromic	Electric field	

The field of smart materials is diverse and continuously evolving, with new materials and functionalities being discovered and developed. Overall, the classification of smart materials promotes efficient utilization, integration, and advancement in various industries. The mentioned examples can be found in Table 2.1 among others with their respective outputs and inputs. In Figure 2.1 some applications can be found regarding the main classes mentioned.

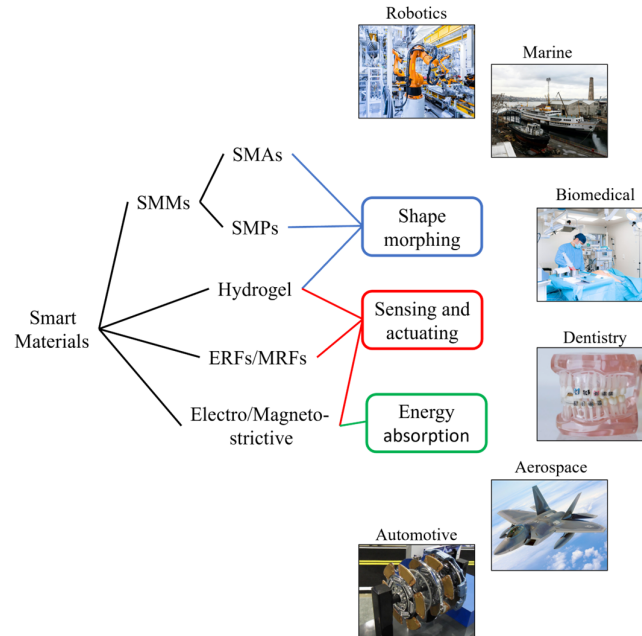


Figure 2.1. Potential applications of the main types of smart materials

2.3 Modeling of smart materials

2.3.1 Modeling methods

In recent years, major developments have been made in computer science and in particular simulations. Computer simulations have become more relevant in the development of new materials. As the demand for modeling and simulation grows, they are not only used for system analysis but also for designing and optimization. The relevance of modeling is discussed here below referencing different aspects concerning smart materials [153]:

Understanding Material Behavior: Smart materials exhibit unique properties and behaviors that can be difficult to predict and control without proper modeling. By developing accurate models, engineers can gain insights into the underlying mechanisms and behavior of smart materials, enabling them to design more effective systems.

Performance Optimization: Modeling allows engineers to explore and optimize the performance of smart material systems before physical prototyping. By simulating the behavior of the materials and their interaction with the surrounding environment, designers can identify the optimal configuration and dimensions to achieve desired performance objectives [154].

Cost and Time Savings: In a lot of cases, it is not feasible to assemble an experimental setup or configuration due to costs or environmental constraints. Building physical prototypes of smart material systems can be time-consuming and expensive. By using models, engineers can quickly evaluate different design alternatives and iterate on them virtually, reducing the need for multiple physical prototypes and associated costs [155].

Risk Mitigation: Smart materials often have complex responses and can exhibit nonlinear behavior. By using models, engineers can analyze and predict how the material will behave under various operating conditions and external stimuli. This enables them to identify potential risks and mitigate them in the design stage, improving overall system reliability.

Scalability and Generalization: Since smart materials are often utilized in various applications, models provide a framework for capturing the fundamental behavior of smart materials, allowing their application in different systems and scenarios. Once a reliable model is developed, it can be used as a basis for designing a wide range of smart material-based systems, saving time and effort in each new application.

Overall, modeling empowers engineers to understand, optimize, and control the behavior of smart materials, leading to more efficient and reliable systems while reducing development time and costs. The specific modeling approach can vary widely depending on the type of smart material and the intended application. Advanced numerical tools and specialized modeling techniques are often employed to accurately capture the behavior of these materials [156-158].

2.3.1.1 Finite element analysis (FEA)

FEA is based on the Finite Element Method (FEM), which is unquestionably one of the most commonly used numerical tools for understanding physical systems with complicated boundary conditions [159, 160]. Therefore, FEA is an efficient approach to investigate the nonlinear behaviors of smart materials. Due to its broad application, the implementation of constitutive equations in FE software, such as COMSOL, ABAQUS and ANSYS has been gaining a lot of attention [161]. Modeling smart materials using FEA involves several steps [162, 163]:

For each material or structure the geometry needs to be defined. The geometry is discretized into smaller elements by meshing. The material properties need to be specified and will depend on the type of smart material being modelled. For instance, for SMMs, phase transformations would be needed in combination with corresponding temperatures and mechanical properties.

To model industrial scenarios appropriate boundary conditions need to be applied. This consists of fixing nodes/surfaces, applying loads and adding thermal/electrical boundary conditions. A suitable solver needs to be chosen within the FEA algorithm since they can vary in terms of speed and accuracy. Smart materials often have complex constitutive models that relate various physical parameters. It is important that FEA algorithm supports the constitutive equations for integration and implementation.

The software/solver will solve the equations governing the material behavior of the smart material based on the given material properties, boundary conditions and geometry. In addition, convergence of the solution is essential to establish stability and acceptability. Furthermore, data visualization through plots and quantitative data extraction are imperative for analysis. Subsequently, comparison with experimental data will validate the results, prompting adjustments in parameters. Finally, conducting sensitivity analysis will explain the impact of material properties and other parameters on the desired behavior within the model [164].

The accuracy of the FEA model depends on the fidelity of the material properties, the mesh quality, the chosen solver, and the adequacy of boundary conditions. The physics associated

with the model needs to be included as accurately as possible to create a precise model. For instance, FEM is also used to account for nonuniformities of the electric field used to model actuation performance. This is an approach useful for dynamic modeling with enhanced robustness [165, 166]. Additionally to the FEM, other numerical methods are also known as alternatives for FEA. Boundary Element Method (BEM): This method is based on an integral equation formulation of a boundary value problem. BEM is more useful for concise 3D objects but has more difficulties with vast geometries. This method is more focused on the boundary instead of the entire geometry [167, 168]. Finite Difference and Finite Volume Methods: These methods also make use of a boundary value problem, but instead of the integral equation formulation, the focus lies on the differential formulation. They are mostly used in computational fluid dynamics and heat transfer scenarios, serving as effective tools for conserving laws of physics [169, 170].

2.3.1.2 Multiscale modeling

Smart materials' intricate microstructures affect their behavior, making multiscale modeling a vital method for investigating both macroscopic and microscopic phenomena in these materials [171]. Stimuli-responsive polymers are the types of smart material where Multiscale modeling would seem more suitable. By looking at different scales a broad scope of the material could be researched. Each length scale is also associated with a different simulation method, which can be seen in Figure 2.2 [172, 173]. In this section three simulation methods of Multiscale modeling are briefly discussed based on different scales applicable to stimuli-responsive polymers [174].

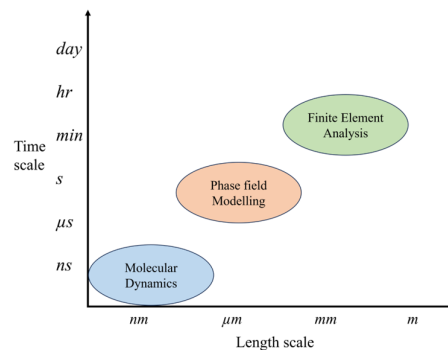


Figure 2.2. Different types of length and time scales associated with the methods of simulations

(1) All-Atom Molecular Dynamics (AAMD)

AAMD is a method used for studying the characteristics of polymers at an atomic level. This method calculates particle locations over time using the classical Newton's equation of motion. The time scales of AAMD are typically in the tens to hundreds of nanoseconds range, with length scales in the tens of nanometers [175]. AAMD is mostly used to explore the response of the stimuli-responsive polymers. This technique regulates the interactions between particles by using a special energy function, often known as a force field, which consists of bonded (bond angles, bond lengths, etc.) and non-bonded components (van der Waals) parameters [176].

(2) Coarse-Grained Molecular Dynamics (CGMD)

For comparatively bigger polymer systems, AAMD will be constrained by computing time and resources. It is not suitable for use in bigger polymer systems. To address this issue, much work has been put into developing particle-based coarse-grained models to investigate large systems. CGMD simulations can help bridge the gap between atomistic simulations and experiments in the understanding of polymers across the range from micron scale [177, 178]. In CGMD, relating to smart polymer modeling, the system can be simplified as each molecule of the polymer is coarse-grained into a string of beads, which are all connected. It is represented as a sphere of determined mass repelling each other via the Weeks-Chandler-Anderson potential [179]. In addition to this, simulation results found with AAMD and experimental results are used to gain relevant force field parameters.

(3) Dissipative Particle Dynamics (DPD)

The DPD approach, aligns with the time scale of the response of self-assembled polymers. This is a mesoscopic simulation method, with mesoscopic fitting between macroscopic and atomic [180]. This method has been utilized as a prominent tool to research complex systems of soft matter, therefore it can be used to study the stimuli-responsiveness of polymers. In DPD simulations, polymer monomers will be simplified to DPD beads by coarse-graining. Compared to the AAMD method, the atomic clusters are replaced by dissipative beads, with the details just being included as internal forces [181]. In DPD simulations, physical quantities are often expressed in reduced units for computational simplicity. Similar to the AAMD approach, bead motion is determined by solving Newton's equations of motion [182].

(4) Phase Field Modeling (PFM)

The arrangement and characteristics of different phases on a microscopic level have a major influence on the behavior of materials on the macroscopic level [183]. The imperfections, or defects, in the lattice, determine the properties of most materials. Defects such as dislocations, precipitates or solute atoms in the lattice, but also defects in the lattice boundaries, such as grains. The microstructure-properties relationship is commonly explored using FEM. However, FEM struggles with dynamic boundary changes during processing. PFM provides a robust alternative for simulating microstructural evolution [184, 185].

PFM is particularly relevant for phase transformations and complex changes in microstructure over time under the influence of factors, such as stress, temperature and composition. For instance, this is important for SMAs since a transition is made from austenite to martensite. The key principle behind PFM is making use of continuous fields for the interfaces. All the discontinuities found across the interfaces, in addition to some boundary conditions, are depicted by a clean smooth version of a phase field. Every PFM is based on this formulation of the free energy as a functional [186]:

$$F = \int f(\phi_1, \phi_2, \dots, \phi_n, c_1, c_2, \dots, c_n, \nabla\phi_1, \nabla\phi_2, \dots, \nabla\phi_n, \nabla c_1, \nabla c_2, \dots, \nabla c_n, p, T, \dots) \quad (2.1)$$

with ϕ being a set of non-conserved fields and c a set of conserved fields. The energy function f normally includes a potential with local minima, gradient terms such as ∇c which relate to

the energetic costs and state variables such as pressure and temperature, or other external stimuli which is the case for most smart materials.

2.3.2 Constitutive models for smart materials

Implementing constitutive models is a crucial step in using numerical methods. Solving complex problems in materials science and engineering requires modern numerical methods, but their effectiveness hinges on the quality of the constitutive models [187, 188]. These models describe the mathematical relationships between the material's behavior of different factors such as stress, strain, etc. The mathematical relationships are found to be the constitutive equations, which are essential for understanding and predicting how materials will behave under various loading conditions [189]. Constitutive equations can range from linear relationships to more complex nonlinear equations, such as to account for large deformations at high temperatures. Constitutive equations are frequently derived from experimental data and can be application-specific. Therefore, the exact form of these equations depends on the material and the phenomena that are dealt with [190, 191]. This section is dedicated to conclude the common constitutive equations for SMAs, SMPs, hydrogels and MRFs. In addition, the review presents the constitutive models of various smart materials, emphasizing their properties and state changes, without delving into dynamic analysis.

2.3.2.1 Constitutive models for SMAs

Due to external stimuli caused by the change of the microscopic phase transformations of the phases austenite and martensite, SMAs have the macroscopic mechanical properties of the SME and SE. The stress-strain constitutive model encompasses both complex mechanical properties and phase transformations [192].

(1) Adjusted Brinson Model

The behavior of the SMA material relies on a set of variables such as the stress, temperature and the crystal structure, the latter depends on the loading and thermal histories. The constitutive model is based on loading (tensile force) at a low temperature, unloading and then heating [193]. To account for this, in SMAs an internal variable is introduced ξ . This letter depicts the condition of the materials as a martensite material fraction, with $\xi = 0$ indicating the material is completely in the austenite phase. The created martensite has two results, twinned or detwinned [194]. Twinned indicates multiple martensite variants coexisting, while detwinned suggests a connection with one dominant variant, as expressed in Equation (2.2),

$$\xi = \xi_S + \xi_T \quad (2.2)$$

where the subscript S stands for stress-induced and T for temperature induced. The model is an adjusted model for the situation of a simple one-dimension SMA model proposed by Brinson [195] and is given in Equation (2.3),

$$\sigma - \sigma_0 = E(\xi_0)\varepsilon_0 + \Omega(\xi)\varepsilon_S + \theta(T - T_0) \quad (2.3)$$

with σ depicting the stress currently resisted in the material, $E(\xi)$ is the elastic modulus depending on the current crystal structure, ε is the strain experienced by the material and θ is

the thermal response shown by the material. All the variables with the “0” subscript indicate the initial state.

(2) Macroscopic models

The macroscopic models depict the behavior of SMAs based on phenomenological considerations, simple micromacro thermodynamics or experimental data. The mentioned models in this section are pioneering models which are used as foundations for specific applications of models made for SMAs. These models have attributed to major developments in the modeling of SMAs [196].

a) Boyd and Lagoudas - Phenomenological Model

This model is based on an energy potential which is taken from physical considerations [197]. In this case, the state equation of this model is derived from the following Gibbs free energy potential [198], with ψ_A and ψ_M being the free energies of austenite and martensite. ψ_{mix} indicates the mixing term reflecting on the different interactions between the two phases. This is the first model that takes into consideration the reorientation of martensite by including an inelastic strain tensor,

$$\psi(\boldsymbol{\sigma}, T, \xi, \boldsymbol{\varepsilon}^{tr}) = (1 - \xi)\psi_A(\boldsymbol{\sigma}, T) + \xi\psi_M(\boldsymbol{\sigma}, T) + \psi_{mix}(\xi, \boldsymbol{\varepsilon}^{tr}) \quad (2.4)$$

the following stress-strain relation of Equation (2.5) is used in this model,

$$\boldsymbol{\sigma} = [\xi\mathbf{S}_M + (1 - \xi)\mathbf{S}_A]^{-1} : [\boldsymbol{\varepsilon} - \boldsymbol{\varepsilon}^{tr} - \boldsymbol{\alpha}(T - T_0)] \quad (2.5)$$

b) Auricchio and Petrini - Phenomenological Model

This model is based on the Helmholtz free energy function and is written as a function of the total strain $\boldsymbol{\varepsilon}$, \boldsymbol{e}^{el} and \boldsymbol{e}^{tr} being the elastic and transformation strain of the SMA. In addition to this G is the shear modulus and κ is the bulk modulus [199]. The model can be found below as Equation (2.6),

$$\Phi(\boldsymbol{\varepsilon}, \boldsymbol{\varepsilon}^{tr}, T) = \frac{1}{2} \kappa (\text{Tr}(\boldsymbol{\varepsilon}))^2 + G \|\boldsymbol{e}^{el}\|^2 + \tau_m(T) \|\boldsymbol{e}^{tr}\| + \frac{h}{2} \|\boldsymbol{e}^{tr}\|^2 + I_{0, \boldsymbol{\varepsilon}_{\max}^{tr}}(\boldsymbol{\varepsilon}^{tr}) \quad (2.6)$$

The associated stress-strain function found can be found below as Equation (2.7),

$$\boldsymbol{\sigma} = 2G \text{dev}(\boldsymbol{\varepsilon} - \boldsymbol{\varepsilon}^{tr}) + \kappa [\text{Tr}(\boldsymbol{\varepsilon}) - 3\alpha(T - T_0)] \quad (2.7)$$

c) ZM phenomenological model

This model is based on an energy potential which is taken from physical considerations. In this case, the state Equations of this model are derived by Zaki and Moumni [200] from the Helmholtz free energy potential which is shown in Equation (2.8),

$$\Phi(T, \boldsymbol{\varepsilon}_A, \boldsymbol{\varepsilon}_M, \boldsymbol{\varepsilon}^{ori}, \xi) = (1 - \xi)\Phi_A + \xi\Phi_M + I_{AM} \quad (2.8)$$

Leading to Equation (2.9) which is a strain-stress relationship, with K_a as the elastic stiffness tensor of austenite and K_m is the elastic stiffness tensor of martensite. This model is based on the assumption that the reversible inelastic deformation of SMAs is due to the orientation of the different Martensite forms,

$$\boldsymbol{\sigma} = [(1 - \xi)\mathbf{K}_A^{-1} + \xi\mathbf{K}_M^{-1}]^{-1} : (\boldsymbol{\varepsilon} - \xi\bar{\boldsymbol{\varepsilon}}^{tr}) \quad (2.9)$$

The above-mentioned models have in recent years been expanded, and more details have been added, which is based on the applications needed [201, 202]. Therefore, the initial models are added here since most of them have been adaptations of the original models.

2.3.2.2 Constitutive models for SMPs

The constitutive models are based on the investigation of the mechanical behavior and the mechanisms associated with SMP structures, to depict the SME in as much detail as possible. Compared to other SMMs, offer the widest range of stimuli for activation. Even though different types of stimuli triggered SMPs work differently, the internal mechanism is similar to thermal-induced SMPs. Consequently, most research is dedicated to thermal-induced SMPs [203]. Many approaches exist to examine the principles and mechanisms of the shape memory phenomenon, such as the stress-strain relationship under several factors such as temperature. In general, there are two categories: rheological models, emphasizing viscoelasticity theory, and micromechanical models, centering more on phase transitions. Subsequent discussion will scrutinize these models [204, 205].

(1) Rheological models SMPs

Rheological models have been modelled as springs and dashpot elements. Due to the model parameters varying in temperature, the models can quantify the SME of SMPs. These models can efficiently analyze mechanical qualities affected by temperature, time, strain rate, and other factors.

a) Basic Viscoelastic Model

A simplified three-element model is proposed by Li et al. [206] to effectively simulate the characteristics of stress, strain and temperature in combination with a Kelvin element and a spring element all in series. These elements represent viscoelasticity, supplemented by accounting for heat expansion caused by temperature fluctuations. Consequently, the model delineates thermo-viscoelastic behaviour, derived from one-dimension constitutive equations, resulting in Equation (2.10),

$$\sigma + \frac{\mu(T)}{(E_1(T) + E_2(T))} \frac{d\sigma}{dt} = \frac{\mu(T)}{\left(1 + \frac{E_1(T)}{E_2(T)}\right)} \left(\frac{d\varepsilon}{dt} - \alpha \frac{dT}{dt}\right) + \frac{1}{\frac{1}{E_1(T)} + \frac{1}{E_2(T)}} (\varepsilon - \alpha(T - T_0)) \quad (2.10)$$

where σ , ε and T indicate the stress, strain and temperature. The α depicts the expansion coefficient and E is the elastic modulus. The model presented in Equation (2.10) can efficiently predict the response of the SMPs by making use of simplified parameters, which is very beneficial for some applications in engineering.

b) Thermoviscoelastic Models of SMPs coupled with temperature and rate effects

The previous model has provided a simple method to depict the mechanical properties of SMPs, but only focuses on infinitesimal strains. Diani [207] has developed a model to account for large strain deformation. This model is based on thermodynamics, thus the deformation is based on internal energy and entropy. The total Cauchy stress has been formulated as follows in Equation (2.11),

$$\boldsymbol{\sigma}^\eta = \frac{E^r}{6} \frac{T}{T_h} \mathbf{F}^e \mathbf{F}^{eT} - p \mathbf{I}$$

$$\boldsymbol{\sigma}^U = \mathbf{L}^e [\ln(\mathbf{V}^e)] \quad (2.11)$$

with $\boldsymbol{\sigma}^\eta$ indicates the stress from the entropy branch, with T_h being a higher temperature than regular T . \mathbf{F}^e is the deformation gradient, p is the Lagrange multiplier and \mathbf{I} is the invariant of the right Cauchy-Green tensor of the elastic deformation. With $\boldsymbol{\sigma}^U$ indicating the stress from the internal energy branch, where \mathbf{L}^e is the elastic constant tensor and \mathbf{V}^e is the left stretch tensor found from the deformation gradient \mathbf{F}^e . In general, this model can precisely make an estimation of the remaining strain when the stress is released. It provides a useful groundwork for the thermomechanical response of SMPs while experiencing large deformation.

c) Fractional Viscoelastic Constitutive Model

A majority of SMPs are described by relaxation behavior, leading to a large number of material parameters to be determined experimentally. An attempt is made to describe the complex viscoelastic behavior with a lower number of parameters, which can be seen in Equation (2.12). The fractional viscoelastic model is applied to accurately look into the thermomechanical responses of SMPs. The thermal expansion is considered independent of the mechanical behaviors and was defined separately from the model. For the complete derivation and parameters included refer to the work of [208],

$$\sigma_M(t) = \sigma_{eq}(t) + \sum_{i=1}^m \sigma_i(t) = E_{eq} \varepsilon_M(t) +$$

$$\sum_{i=1}^2 \left[E_i \int_{t_0}^t E_\beta \left(-\left(\frac{t-\xi}{\tau_i} \right)^\beta \right) \frac{d\varepsilon_M(\xi)}{d\xi} d\xi + E_\beta \left(-\left(\frac{t-t_0}{\tau_i} \right)^\beta \right) \sigma_i(t_0) \right] \quad (2.12)$$

where σ_M is the total mechanical stress, E is the stiffness of the spring, E_β is the Mittag-Leffler function [209]. n belongs to the set of integers, τ is the relaxation time and t is the time.

(2) Phenomenological models SMPs

Most phenomenological models for SMPs are built on the “meso-mechanical approach”, which simplifies the structure to continuous phases. Certain external stimuli lead to the different phases transforming into one other, which again reflects the properties of SMP. In comparison to the rheological models, the phenomenological models can relate the phase transitions to the SME, which provides a clear comprehension of the deformation mechanisms.

a) Classic Phenomenological Constitutive Model

The first phenomenological 3D model for thermally activated SMPs is proposed by [210], which suggested that the SMP structure consists of two phases, the frozen phase and the active phase. The deformation in the frozen phase is dominated by internal energy change, and polymer conformation motion occurs in the active phase. The frozen phase is the most important phase of a polymer in its glassy state, whereas the active phase is primarily concerned with the rubbery state. The classic phenomenological constitutive model decomposes the strain energy into thermal, elastic strain, and frozen entropic (stored) strain components and uses the frozen

volume fraction as an internal variable to describe the microstructure evolution. All the parameters lead to the constitutive equation for SMPs in a thermomechanical cycle in one-dimension form which is expressed as follows in Equation (2.13),

$$\sigma = \frac{\varepsilon - \varepsilon_S - \varepsilon_T}{\frac{\phi_f}{E_i} + \frac{1 - \phi_f}{E_e}} = E \left(\varepsilon - \varepsilon_S - \int_{T_h}^T \alpha dT \right) \quad (2.13)$$

with ϕ_f being the frozen fraction, ε_S frozen entropic strain, ε_T the thermal strain, E_i is the modulus associated with the glossy state at a low temperature and E_e is the modulus associated with the entropic deformation at the rubbery state. For the complete derivation and parameters included refer to the work of [210].

b) Phenomenological Models of SMP with Rate Effect

Following the classic phenomenological constitutive model, a new model was proposed by [211]. The new model was a phase-evolution-based thermomechanical model aiming to describe the behaviors of amorphous SMPs. Equations were derived to describe the mechanical behaviors taking place within a complete thermal mechanical cycle [188]. By making use of the concept of frozen strain, which is dependent on time and temperature, Equation (2.14) can be derived:

$$\begin{aligned} \sigma_{\text{total}} &= \frac{\varepsilon_{\text{total}} - \varepsilon_{f\text{-real}} - \varepsilon_T}{\frac{\gamma}{E_g}} + \frac{1 - \gamma}{E_r} \\ \frac{d\varepsilon_f}{dT} &= \frac{d\gamma}{dT} [1 - f(T)] \frac{\varepsilon_{\text{total}} - \varepsilon_f - \varepsilon_T}{E_r \left(\frac{\gamma}{E_g} + \frac{1 - \gamma}{E_r} \right)} \\ \varepsilon_{f\text{-real}} &= \varepsilon_f - \int_0^t \varepsilon_f e^{\frac{-(t-a)}{\tau}} da \end{aligned} \quad (2.14)$$

with σ_{total} being the total stress, $\varepsilon_{\text{total}}$ is the total strain, $\varepsilon_{f\text{-real}}$ is the real frozen strain depending on the time, γ is the volume fraction of the glassy phase, E_g is the elastic modulus in the glassy phase, E_r is the elastic modulus in the rubbery phase, ε_f is the total frozen strain in the materials. The new proposed model is fit to be used for predicting strain and stress respondents of SMPs under a free strain condition but is also capable of reproducing the behavior of SMPs under other external constraints.

2.3.2.3 Constitutive models for hydrogel

A generalized theory has been created to specify different kinds of hydrogel, even if the hydrogels differ by their stimulus. This section gives the constitutive equations for different kinds of hydrogel, such as neutral gel, pH-sensitive gel, temperature-sensitive gel and photothermal-sensitive gel. The general model is the same, but the model has been adjusted for each of the gels concerning their properties. The constitutive equations make use of the Neo-Hookean hyperelastic material model [212, 213], whose strain-energy function is given in Equation (2.15) where T is the absolute temperature, k_B is the Boltzmann constant, N is the

crosslink density, λ is the principles stretch in each direction. This equation is chosen since hydrogels are a hyperelastic material type.

$$W = \frac{1}{2} N k_B T (\lambda_1 + \lambda_2 + \lambda_3 - 3) \quad (2.15)$$

(1) Neutral Gel

The most frequently studied type of gel, is the neutral gel. The neutral gel has one single stimulus and that is external exposure to water. Since there are no other stimuli, the constitutive model is fundamental. By combining the Flory–Rehner free-energy function due to stretching a network of polymers with the three principal normal stresses [214], the general form can then be expressed as follows in Equation (2.16),

$$\frac{s_{iK}}{v} = N v (F_{iK} - H_{iK}) + \left[J \log \left(1 - \frac{1}{J} \right) + 1 + \frac{\chi}{J} - \frac{\mu}{kT} J \right] H_{iK} \quad (2.16)$$

Equation (2.16) connects the stress component to the deformation gradient in the case of the gel being held at a not-varying chemical potential by a reservoir of solvent molecules. With s_{iK} being one of the three nominal stresses, v is the specific volume, F_{iK} is the deformation gradient, μ is the chemical potential, J is the volumetric strain, and χ is the dimensionless measure of the enthalpy of mixing [215].

(2) Salt Concentration Sensitive Gel

When exposed to an ionic solution, polyelectrolyte networks absorb it, causing gel swelling, resulting in a salt concentration-sensitive gel [216]. Similar to the neutral gel, salt concentration sensitive gel is subjected to the same concentrations only with the stimulation of a salt concentration. Equation (2.17) describes the mechanical deformation of the salt concentration gel, including the free swelling and contained swelling cases. It combines the free energy functions of salt and ions with that of the stretching of the hydrogel. With σ_{ij} being the true stress, J is the det(F), C^0 is the fixed charge in the gel, c_0 is the concentration salt, C^+ and C^- are the positive and negative ion concentrations [217].

$$\frac{\sigma_{ij}}{v} = \frac{Nv}{J} (F_{iK} F_{jK} - \delta_{ij}) + \left(\log \frac{J-1}{J} + \frac{1}{J} + \frac{\chi}{J^2} + 2v c_0 \right) \delta_{ij} + \left[c^+ \left(\log \frac{c^+}{c_0} - 1 \right) + c^- \left(\log \frac{c^-}{c_0} - 1 \right) + J \left(\frac{\partial c^+}{\partial J} \log \frac{c^+}{c_0} + \frac{\partial c^-}{\partial J} \log \frac{c^-}{c_0} \right) \right] \quad (2.17)$$

It is worth noting that during the last decade, studies have disagreed if the concentration C^a is dependent on J . In the derivation resulting in Equation (2.17), it is assumed that it is dependent to realize an equation which can be implemented in FEM. For the detailed derivation with all the assumptions please refer to the study of [217].

(3) pH-Sensitive Gel

The pH-sensitive hydrogel consists of a network of stretching soft materials which have acidic groups and are in equilibrium with a solution of which the solvent is water and mechanical forces [218]. The constitutive equation is based on the summation of the free energies of the

stretching polymers, the solvent, the ions and the acidic groups: $W = W_{str} + W_{mix} + W_{ion} + W_{dis}$. Equation (2.18) emerges from this summation, where c^{H^+} , \bar{c}^- , and \bar{c}^+ denote the concentrations of protons, negative ions, and positive ions in the external solution, respectively. For a detailed derivation, refer to the work of [219].

$$\frac{\sigma_{ij}}{kT} = \frac{Nv}{J} (F_{iK}F_{jK} - \sigma_{ij}) + \left(\log \frac{J-1}{J} + \frac{1}{J} + \frac{\chi}{J^2} \right) \delta_{ij} - v\delta_{ij}[c^{H^+} + c^+ + c^- - \bar{c}^{H^+} - \bar{c}^+ - \bar{c}^-] \quad (2.18)$$

(4) Temperature-sensitive Gel

Temperature-sensitive hydrogels, also known chemically as PNIPAM hydrogels, are hydrogels that can withstand large changes in volume owing to temperature changes [220]. Due to their distinctive characteristic of exhibiting a sharp macromolecular transition from hydrophilic to hydrophobic, temperature-sensitive hydrogels constitute a significant branch within the realm of hydrogels. In addition to this, these types of hydrogels are transparent, elastic and flexible. The constitutive equation is similar to the one of neutral gel, the only addition is the interaction parameter χ with χ_0 , χ_1 and ϕ (Equation (2.19)) being dependent on experimental data obtained for PNIPAM [221].

$$\chi = \chi_0 + \chi_1\phi \quad (2.19)$$

By combining Equation (2.16) of the neutral gel with Equation (2.19) and the uniaxial load case the following two lines can be obtained which form Equation (2.20). With s being the stress, V is the volume of the gel and V_0 is the volume of the referential state.

$$\begin{aligned} Av(\lambda_1^2 - 1) + \left(\frac{V}{V_0}\right) \log \left[1 - \left(\frac{V}{V_0}\right)^{-1} \right] + 1 + (\chi_0 - \chi_1) \left(\frac{V}{V_0}\right)^{-1} + 2\chi_1 \left(\frac{V}{V_0}\right)^{-2} &= 0, \\ \frac{1}{\lambda_3} \left[Nv(\lambda_3^2 - 1) + \left(\frac{V}{V_0}\right) \log \left[1 - \left(\frac{V}{V_0}\right)^{-1} \right] \right] + \\ \frac{1}{\lambda_3} \left[1 + (\chi_0 - \chi_1) \left(\frac{V}{V_0}\right)^{-1} + 2\chi_1 \left(\frac{V}{V_0}\right)^{-2} \right] &= \frac{sv}{k_B T} \end{aligned} \quad (2.20)$$

2.3.2.4 Constitutive models for MRFs

In MRFs, rheology is crucial due to their two-phase nature. Carbon Iron Powder (CIP) is widely used for the initial phase of MRFs, due to its high saturation magnetization and wide availability [222]. The rheology affects the way the fluids are applied in practical settings. Experimental studies predominantly focus on shear stress and stress rate as key descriptors of the rheological properties of MRFs [223]. Various equations can be found for the shear stresses, all including different magnetic properties. This section will summarize the most prominent constitutive equations for MRFs based on [150, 151].

The first is a traditional finite element model, which includes nonlinearity and saturation of the magnetization of particles integrated. In this model, MRFs have been simulated as chains of

infinite length. The chains consist of aspherical magnetizable particles whose alignment depends on the applied direction of the magnetic field. The equation is given as Equation (2.21) with γ being the shear strain, F being the chain tension, and W being the radius of the particles. For the entire derivation of this equation refer to [151].

$$\tau = \frac{\gamma}{1 + \gamma^2} \frac{F}{\pi W^2} \quad (2.21)$$

A micro-macro model has been developed, based on a single-chain model. This model makes use of the mean magnetization approximation and can be found in Equation (2.22). In addition to this, a normal distribution is followed for the inclining angles of the evolving particle chains. With τ_0 being the shear stress of the MRF without magnetic field applied, A is a constant, μ_0 is the Permeability of vacuum, ϕ is the particle volume fraction, R is the core radius, χ is the magnetic susceptibility of magnetic particle, H illustrates the intensity of the magnetic field, t_h demonstrates the thickness of the non-ferro-magnetic coat, and δ is the distance between two particles. For the second part of the equation: θ is the incline angle of the chain, μ is the mean, and σ is the standard deviation. For the entire derivation of Equation (2.22) refer to [224].

$$\tau = \tau_0 + \frac{A\mu_0\phi R^3\chi^2 H^2}{(2R + 2t_h + \delta)^3} \cdot \int_{-\frac{\pi}{2}}^{\frac{\pi}{2}} \frac{(5\cos^2\theta - 1)\cos^4\theta \sin\theta}{\sqrt{2\pi}\sigma} e^{-\frac{(\theta-\mu)^2}{2\sigma^2}} d\theta \quad (2.22)$$

To adjust Equation (2.22) for a more exact dipolar model, but without using the approximation that the size of the particles is much smaller than the distance between the particles, yields Equation (2.23). In this equation, n is the number of particles and r_j is the particle radius. Again the distribution of the inclining angles of the particle chains follows a normal distribution [225].

$$\tau = \tau_0 + \sum_{j=1}^{n-1} \frac{\mu_0\phi H^2\chi^2 R^3(2R + \delta)}{r_j^4} \cdot \int_{-\frac{\pi}{2}}^{\frac{\pi}{2}} \left[(1 - 5\cos^2\theta) - \frac{\chi R^3(1 + 4\cos^2\theta)}{3r_j^3} \right] \times \frac{\sin\theta}{\sqrt{2\pi}\sigma} e^{-\frac{(\theta-\mu)^2}{2\sigma^2}} d\theta \quad (2.23)$$

Equation (2.24) can be used to predict the yield shear stress of MRFs if fitting rate parameters are included. In Equation (2.24) λ is the rate parameter, ς is the volume fraction of magnetic particles in the MRFs, r is the radius of the magnetic particle, and B is the magnetic flux density [226].

$$\tau = \frac{\varsigma\pi^2 r\chi^2 B^2}{72\mu_0\delta} \lambda \left\{ \frac{1}{3} + \frac{3\lambda \times e^{-\lambda\pi/2} - \lambda^2}{12(\lambda^2 + 9)} - \frac{\lambda \times e^{-\lambda\pi/2} + \lambda^2}{4(\lambda^2 + 1)} \right\} \quad (2.24)$$

An initial chain model was also established by assuming a normal distribution for the inclining chain angles, which results in Equation (2.25). In this model, ξ has been an additional term as a function of θ [227].

$$\tau = \frac{\zeta AR^3 \chi^2 B^2}{\mu_0 (1 + \chi_1)^2 (2R + \delta + 2t)} \xi \quad (2.25)$$

A compact two-column model is given in Equation (2.26), where ψ is an additional term as a function of θ . In this model, the exponential distribution was applied to describe the distribution of the inclining chain angles, for the complete derivation see [228].

$$\tau = \frac{\phi r^3 \chi^2 B^2}{3\mu_0 (1 + \chi)^2 (2r + 2t + \delta)^3} \psi \quad (2.26)$$

A profound theoretical analysis of the microstructure of MRFs found the following Equation (2.27), where a is the particle radius, k is a parameter to describe the effect of inhomogeneity of CIP particles, and σ is the deviation angle of a particle. This model is based on the structure evolving in a stable hexagonal close-packed structure from a microscopic perspective. Equation (2.27) is also the only model which assumes multiple chains of particles [229].

$$\tau = \frac{4H^2 a^3 \zeta \chi^2 \mu_0}{3k(2a + 2t + \delta)^3} f(\sigma) \quad (2.27)$$

ERFs are similar to MRFs, Kumar [230] provides an interesting continuum-based method for the modeling of electro-magneto-rheological fluids (EMRFs) which are exposed to an electromagnetic field. In this approach the principles of physics and thermodynamics are combined, resulting in a generalized constitutive model. The continuum-based model attempts to generalize the deformations of a fluid continuum to EMR. The generalization is something that is quite in contrast with existing works performed on ERFs and MRFs.

Furthermore, Table 2.2 gives an overview of all the types of constitutive equations being discussed in this chapter regarding the four groups of Smart materials: SMAs, SMPs, Hydrogels and MRFs. It is important to note that the equations that are included in this chapter are chosen due to their fundamental role in the creation of specific models for different applications or since they are most commonly used as models. Nevertheless, there are many more models which could be used, all depending on the application at hand or the information or data needed to gather.

Table 2.2 Summary constitutive models of different smart materials

Type	Equation	Model
SMA	Eq. (2.3)	Adjusted Brinson Model [195]
	Eq. (2.5)	Boyd and Lagoudas - phenomenological model [197]
	Eq. (2.7)	Auricchio and Petrini - phenomenological model [199]
	Eq. (2.9)	ZM phenomenological model [200]
SMP	Eq. (2.10)	Basic viscoelastic model [206]
	Eq. (2.11)	Thermoviscoelastic models [207]
	Eq. (2.12)	Fractional viscoelastic constitutive model [208]

	Eq. (2.13)	Classic phenomenological constitutive model [210]
	Eq. (2.14)	Phenomenological models of SMP considering rate effect [211]
Hydrogel	Eq. (2.16)	Neutral Gel model [214]
	Eq. (2.17)	Salt concentration gel model [216]
	Eq. (2.18)	pH-sensitive gel model [218]
	Eq. (2.20)	Temperature sensitive Gel model [221]
MRF	Eq. (2.21)	Finite-element microscopic model [151]
	Eq. (2.22)	Micro-Macro model [224]
	Eq. (2.23)	Magnetic-dipoles-based micro-macro model [225]
	Eq. (2.24)	Yield shear stress model [226]
	Eq. (2.25)	Initial tilt chain model [227]
	Eq. (2.26)	Compact two-column model [228]
	Eq. (2.27)	Micro model based on hexagonal close packed structure [229]

2.4 Potentials of the model-based design for mechanically intelligent structures

The optimization of model-based design has emerged as a critical approach for unlocking the full potential of smart structures. By utilizing numerical models, researchers and engineers can simulate and predict the behavior of smart materials under different conditions, enabling them to optimize their design parameters. The process of model-based design involves employing simulation tools and numerical methods to explore a vast design space, ultimately identifying the most efficient and effective solutions. Constitutive models are needed to accurately depict the nonlinear behavior of a smart material. Each type of smart material has its respective type of constitutive equation based on a specific free energy function. Each constitutive equation includes the parameters found by experimental data, resulting in less accuracy to some extent. Each constitutive equation depends on the application and the required phenomena should be studied. The mechanically intelligent structure is an adaptive structure actuated by multiple stimuli. A desire for a functional mechanically intelligent structure requires a complex model for design optimization. To improve smart materials-based design, proper selection of suitable simulation tools and constitutive equations are required to eventually reach the model-based design framework. The flowchart of model-based design framework is shown in Figure 2.3. A set of functions (F_i) as input, such as scale, stiffness or strength together with a variety of smart materials (M_i) lead with model-based design to a set of designs (D_i) of which a final design is chosen due to performance comparison and then leading to a working prototype.

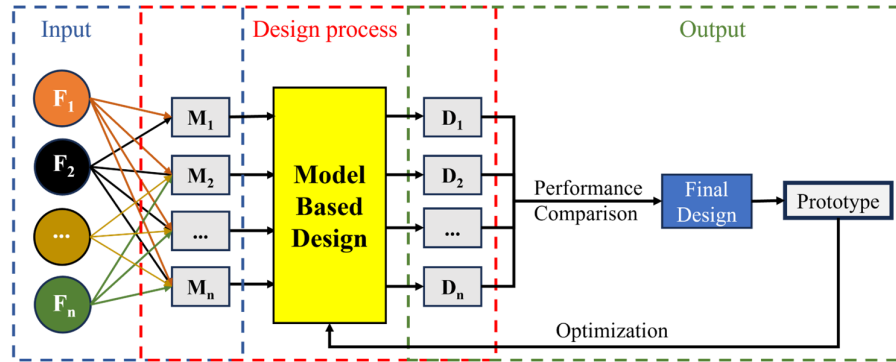


Figure 2.3. Framework of the model-based design strategy

2.5 Conclusion

In this chapter, a comprehensive review of the current state-of-the-art of smart materials is presented, including their classification, properties, and modeling.

Smart materials are classified based on how they react to external factors like temperature, light, pressure, electric fields, or magnetic fields. They exhibit various behaviors, including reacting to pressure or electricity, and altering or retaining their color, shape, volume, or mechanical properties in response to changes in temperature, light, electricity, or magnetism. Smart materials show various properties stimulated by different stimuli. Hydrogels show the volume change actuated by temperature, pH, humidity, or chemical reactions. Shape memory materials can achieve the shape memory effect or stiffness variation by temperature change. Piezoelectric materials generate the electricity by external stress. Light, electric, and magnetic responsive materials can change the shape by inner mechanical strain.

Modeling approaches offer solutions for understanding the properties of smart materials. Commonly used techniques include the finite element method (FEM), molecular dynamics (MD), and phase field modeling (PFM). FEM emphasizes macroscale analysis, relying on constitutive models to study stress-strain relationships. MD operates at the atomic to nanoscale level, enabling the investigation of fundamental properties of smart materials at the atomic scale. PFM focuses on the mesoscale, simulating microstructural evolution such as phase transitions and domain formation. Among them, FEM is widely utilized for designing structures involving smart materials. A crucial aspect of FEM analysis for smart materials is selecting an appropriate constitutive model. This chapter highlights the most commonly used models, including thermally dependent viscoelastic or super/hyper-elastic models for shape memory materials, free energy models for hydrogels, and rheological models for electro/magneto-rheological fluids.

To apply smart materials into morphing structures, Chapter 3 presents a model-based design framework, employing the numerical approaches outlined in this chapter. Using this systematic framework, Chapter 4 develops the conceptual design of a hydrogel-based bending morphing structure with stiffness variation. Expanding on this conceptual design, Chapter 5 explores the use of multiple smart materials, including hydrogel and shape memory polymer (SMP), to

develop a metastructure capable of both self-actuation and stiffness variation. Finally, Chapter 6 integrates the shape memory materials-based metastructure with a novel thermal control system, enabling synchronized operations to coordinate the shape memory and variable stiffness effects for mechanical intelligence in the morphing structure.

3 Model-based design framework for mechanically intelligent morphing structure*

As analyzed in Chapter 2, smart materials that possess distinct capabilities offer possibility for the design of adaptable morphing structures for mechanical intelligence. Model-based design presents a promising approach of the development of smart material-based morphing structures. However, there is no comprehensive design framework connecting the materials properties to adaptable structure to support the smart materials based morphing structure embedded the mechanical intelligence. To apply smart materials into morphing structures to build mechanical intelligence, this chapter constructs a comprehensive model-based design framework for the design process and strategy. Section 3.2 introduces the concept of "building block", which is a modular intelligent unit integrating smart material, geometric configuration, and external stimuli, supporting the model-based design process for morphing structure. Section 3.3 introduces the numerical approaches can be used into model-based design framework. Section 3.4 presents case studies that show how a model-based design framework is used to design building blocks. The main conclusions are presented in Section 3.5.

* This chapter is based on Q. Chen, D. Schott, and J. Jovanova, "Model-based design strategy for mechanically intelligent building blocks," Submitted to Mechanical Engineering-Scientific Journal

3.1 Introduction

Soft robotics embedded with mechanical intelligence promises a notable advantage in enhancing flexibility and adaptability, finding extensive utilization in diverse industrial applications [231, 232], from medical to agriculture and offshore. Soft actuators are essential components enabling soft robots to achieve various deformation behaviors, with morphing structures playing a central role in the design and functionality of these actuators. Soft actuators can be categorized into various traditional types, encompassing electrical, pneumatic, particle jamming, and chemical reaction-based actuators [233-236]. However, traditional actuation methods often require additional power systems, which limits their applicability. The emergence of smart materials, utilizing their special properties, has enabled the development of adaptable and dynamic soft actuators. These materials can alter their structure or composition in response to external stimuli such as electrical signals, magnetic fields, light, heat, or chemical interactions [24, 69].

The evolution of soft actuators frequently necessitates cumbersome and ineffectual experimental investigations. Alternatively, computational simulations offer a more streamlined and potentially superior adjunct to this procedure. Modeling soft actuators poses significant challenges due to their pronounced nonlinear behavior and complex geometries. The finite element method (FEM), a widely utilized technique in nonlinear mechanics modeling, provides an efficient means to address these challenges without relying on explicit analytical frameworks [237]. FEM excels in accommodating substantial deformations and material nonlinearities during deformation processes. Consequently, FEM-based models offer a viable means to predict the performance of soft actuators and evaluate the viability of different designs under varying input conditions, thereby streamlining both cost and development timelines [238]. Besides, as for the actuator actuated by particle jamming, coupling method of finite element method and discrete element method (FEM-DEM) is also an effective method to investigate the interaction behaviors between the granular materials and flexible boundary [239]. In the coupling method, FEM serves as a precise tool for characterizing the deformations occurring within the chamber under external loads. Furthermore, the discrete element method (DEM) proves invaluable in modeling particle interactions within granular materials, particularly when dealing with a limited quantity of particles. However, current research primarily emphasizes the development of modeling approaches for either expressing the materials' properties or predicting the hyperplastic characteristics of flexible structures, there is no comprehensive model-based design framework for smart material actuating morphing structures.

In this chapter, we developed a model-based design strategy using smart material structures to create mechanically intelligent building blocks for soft robotics. The key contributions are as follows: First, we demonstrated the effectiveness of the model-based design framework for designing smart actuators. Second, we introduced the concept of building blocks to establish mechanically intelligent morphing structures for soft robotics. Third, we constructed numerical models, including FEM and coupled FEM-DEM models, to capture the nonlinear behavior of smart materials and the interactions between particles and soft bodies, verifying the feasibility of the proposed design strategy. This framework was successfully applied in various cases for

potential applications, such as underwater pipe manipulation, windmill blade installation, and seabed pipe maintenance.

3.2 Design process based on building blocks

Model-based design framework offers a highly efficient and optimized approach in engineering, emphasizing the creation of an optimal design plan based on specific requirements. Unlike traditional methods that rely on physical prototypes, model-based design utilizes numerical models and simulation techniques for iterative improvements, resulting in resource savings and optimized structural designs. The basic design process is shown in Figure 3.1. **By considering the environmental conditions and external stimuli, such as temperature change, humidity change, or chemical conditions, the suitable smart materials that can respond to exact stimulus will be selected. In the design process, the building blocks function as responsive elements, adapting to the designed structures, materials, and external stimuli. During the implementation of the model-based design framework, these building blocks need to adapt to changing conditions, ensuring they continue to function under new requirements.** Using the modular concept of these building blocks, various configurations can then be assembled to achieve specific deformation behaviors. After optimization, different smart materials can be integrated to enhance the actuator's performance.

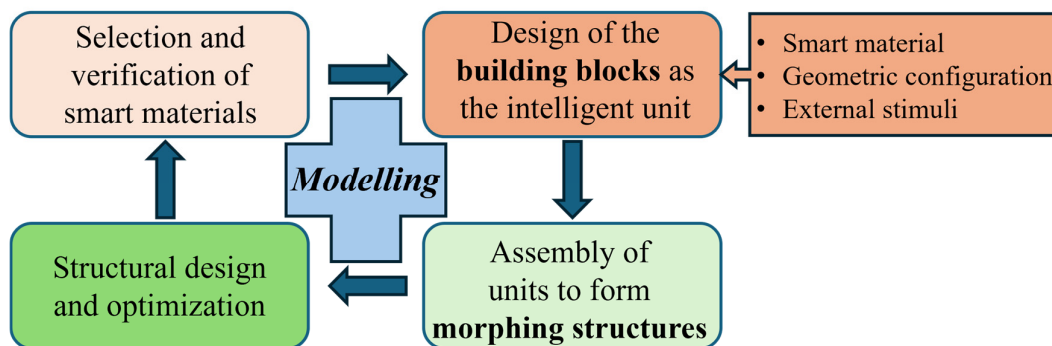


Figure 3.1. The design process of the model-based design strategy

3.3 Methodology

The model-based design approach is fundamental for developing the building blocks. The modelling flowchart, illustrated in Figure 3.2, begins with defining design requirements based on application scenarios, such as scale, environmental conditions, and boundary constraints. From these requirements, spatial and temporal domains are established. Spatial conditions include smart materials and structural geometries, while time-dependent factors involve environmental stimuli, initial conditions, and external loads. These inputs are incorporated into the model-based design framework. In the model-based design step, various numerical methods, such as FEM, DEM, multibody dynamics (MBD), and coupling techniques, are then employed for simulations across multiple scales. The simulation results inform the analysis of different design configurations, which are further refined through optimization. The final design is

realized through fabrication and experimental validation. In general, numerical modeling, particularly for capturing the nonlinear properties of materials, is a critical aspect of this process, with commonly used methods also discussed in this section.

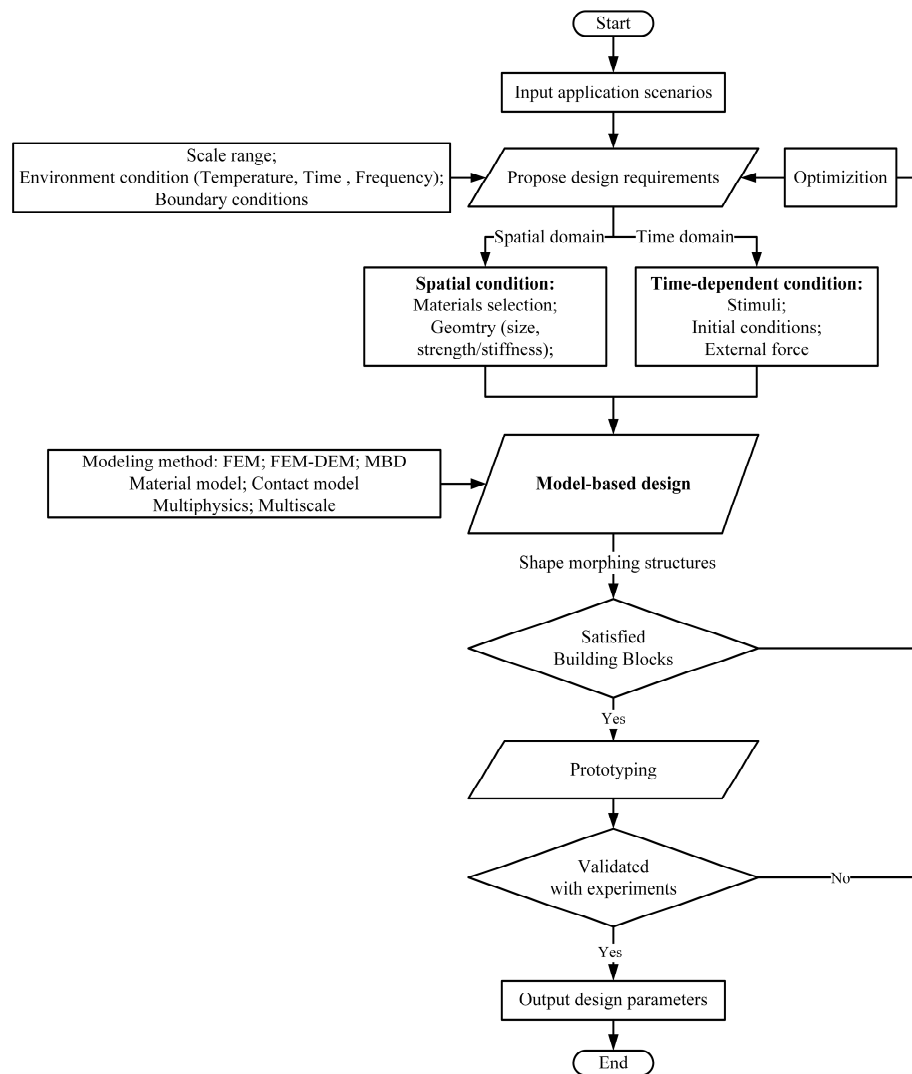


Figure 3.2 The design process of the model-based design

3.3.1 FEM model

FEM is commonly used in the structure and non-linear mechanics behavior analysis. In our study, we used FEM as the basis for smart materials, including temperature-sensitive hydrogel and shape memory polymers. Also, the hyperelastic properties of nonlinear materials are analyzed by FEM in the membrane configuration.

First, in our study, the thermos-responsive hydrogel is modeled by FEM. The temperature-sensitive hydrogel, poly hydrogel has garnered significant academic interest owing to its distinctive characteristics, including facile synthesis and robust stability. Considering hydrogel

as a hyperelastic substance and applying the nonlinear field theory that integrates diffusion and deformation [215], the hydrogel can be expressed by free energy function,

$$W(I_1, I_3, \mu, T) = \frac{1}{2} N k_B T (I_1 - 3 - 2 \log I_3) - \frac{k_B T}{\nu} \left[(I_3 - 1) \log \frac{I_3}{I_3 - 1} + \frac{\chi(T, I_3)}{I_3} \right] - \frac{\mu}{\nu} (I_3 - 1) \quad (3.1)$$

where $I_1 = F_{iK} F_{iK}$ and $I_3 = \det \mathbf{F}$ are the first and the third invariants of the deformation gradient tensor. Furthermore, μ represents the chemical potential, T denotes the temperature, N signifies the number of chains per polymer volume, ν is the volume of a solvent molecule, and k_B stands for the Boltzmann constant. Then, it is conventional to establish a reference state wherein the polymer network achieves equilibrium with a solvent possessing a specific chemical potential denoted as μ_0 . This reference state involves free swelling, where the swelling coefficient (λ) remains uniform in all spatial directions, denoted as $\lambda_x = \lambda_y = \lambda_z = \lambda_0$. Given the free swelling nature of the reference state, the swelling ratio (J) is determined as the cube of the swelling coefficient, $J = \lambda_0^3$. Adhering to these stipulations, the equilibrium state can be delineated as follows,

$$\frac{\mu_0}{kT} = \frac{N\nu}{\lambda_0^3} (\lambda_0^2 - 1) + \log \left(1 - \frac{1}{\lambda_0^3} \right) + \frac{1}{\lambda_0^3} + \frac{\chi}{\lambda_0^6} \quad (3.2)$$

Moreover, the Flory–Huggins interaction parameter, χ , quantifies the enthalpy associated with the blending mechanism and is articulated with respect to T and I_3 for a temperature-sensitive hydrogel,

$$\chi(T, I_3) = A_0 + B_0 T + \frac{A_1 + B_1 T}{I_3} \quad (3.3)$$

The experiments can take the coefficients A_i and B_i as $A_0 = -12.947$, $B_0 = 0.0449 \text{ K}^{-1}$, $A_1 = 17.92$, $B_1 = -0.0569 \text{ K}^{-1}$ [103]. In addition, the expression of stresses immediately follows, and the first Piola–Kirchhoff stress is computed as,

$$\mathbf{P} = \frac{\partial W_0(I_1, I_3)}{\partial \mathbf{F}} = \frac{\partial W_0(I_1, I_3)}{\partial I_1} \frac{\partial I_1}{\partial \mathbf{F}} + \frac{\partial W_0(I_1, I_3)}{\partial I_3} \frac{\partial I_3}{\partial \mathbf{F}} \quad (3.4)$$

In the simulations, we standardize material stresses and Young's modulus by $k_B T / \nu$, where the estimated value is $4 \times 10^7 \text{ Pa}$. Different synthesis conditions yield various initial swelling ratios, and without loss of generality, λ_0 is fixed to 1.5 is uniformly set to 1.5 for all three directions, representing an equilibrium chemical potential of $\mu_0 = -0.01$ for the hydrogel material [240].

In addition, hyperelastic model is also adopted for shape memory polymer (SMP). SMP demonstrates significant viscoelasticity throughout its shape memory, spanning temperatures both above and below the glass transition temperature. This visco-elastic response exhibits a pronounced time–temperature dependency [241, 242]. In our study, we employed the superimposed generalized Maxwell model and Williams-Landel-Ferry (WLF) equation within

FE solver to elucidate the mechanical behavior of SMP. The utilized constitutive equations for the multi-branch viscos-elasticity are as follows [243],

$$\sigma(t) = \varepsilon_0 E_n + \varepsilon_0 \sum_{i=1}^{n-1} E_i e^{-\frac{t}{\tau_i}} \quad (3.5)$$

where $\sigma(t)$ represents stress at time t , ε_0 is the strain at the initial time, E_n denotes the instantaneous modulus, E_i and τ_i represent the elastic modulus and relaxation time of the Maxwell element i , respectively. The relation of relaxation modulus E in the generalized Maxwell equation with time t is expressed as follows,

$$E(t) = E_n + \sum_{i=1}^{n-1} E_i e^{-\frac{t}{\tau_i}} \quad (3.6)$$

and satisfies the limit condition, $\lim_{t \rightarrow \infty} E(t) = E_n$.

Conducting relaxation experiments at various temperatures and applying the time-temperature equivalence principle is essential. This allows the conversion of the relaxation response curve of SMP across different temperatures into a comprehensive relaxation response curve at a specific temperature. According to the WLF equation [243], the connection between the relaxation time at the present temperature T and the relaxation time at the reference temperature of T_r can be written as,

$$\lg \alpha_T = \lg \frac{\tau}{\tau_r} = \frac{-C_1^s (T - T_r)}{C_2^s + (T - T_r)} \quad (3.7)$$

where α_T represents shift factor, C_1^s and C_2^s are material constant.

Besides, silicone is frequently employed as the standard material in soft actuators to facilitate substantial deformations. The Neo-Hookean constitutive model is utilized in the finite element solver to articulate the stress-strain correlation and manifest hyperelasticity traits,

$$W_{\text{NH}} = \mu_{\text{NH}} (\bar{I}_1 - 3) \quad (3.8)$$

where μ_{NH} represents a material constant, \bar{I}_1 denotes the first invariants of the deformation gradient tensor.

3.3.2 FEM-DEM model

The FEM typically analyzes deformations of components under external loads, while the DEM focuses on particle-level materials. To model a soft actuator driven by granular materials, it is essential to couple FEM and DEM for a comprehensive analysis.

The movements of both discrete element and finite element nodes adhere to Newton's Second Law. Consequently, the external force F_i acting on both discrete element and finite element node i is expressed as follows,

$$F_i = m_i \left(\frac{d^2 \mathbf{u}_i}{dt^2} \right) \quad (3.9)$$

where m_i denotes the mass of element i , and \mathbf{u}_i represents the displacement of element i . Furthermore, the centroidal moment of the discrete element i is expressed as follows [244],

$$M_i = I_i \left(\frac{d^2 \theta_i}{dt^2} \right) \quad (3.10)$$

where I_i is the inertia moment of element i and θ_i is the rotation angle of element i . Both of the equation (8) and equation (9) are solved using explicit finite difference method.

Furthermore, the interaction force can be divided into normal force and the tangential force, the normal force F_n , and the tangential force F_s can be expressed as,

$$F_n = F_{n,e} + F_{n,v} \quad (3.11)$$

$$F_s = \begin{cases} F_{s,e} + F_{s,v} & |F_s| < \mu |F_n| \\ \mu F_n & |F_s| \geq \mu |F_n| \end{cases} \quad (3.12)$$

where, $F_{n,e}$ and $F_{n,v}$ are the normal spring force and the normal damping force. Moreover, $F_{s,e}$ and $F_{s,v}$ denote the tangential spring force and tangential damping force. Additionally, the μ is friction coefficient.

During the coupling process, FE elements, along with their grid information, are mirrored into the DEM solver as a wall condition [245]. This involves calculating interaction forces and loads between particles and the wall within each DEM time step. Subsequently, node forces are computed based on particle loads and interpolated onto each FEM element. These node forces are then transformed into distributed loads to facilitate interpolation onto each FE element, enabling the calculation of mesh element deformations and node displacements.

3.3.3 FEM-MBD model

The multibody dynamics (MBD) method is employed to comprehensively capture the motion information, enabling the simulation of scenarios involving significant deformations and the loading process. A coupling between the MBD and FEM models is established to facilitate the transfer of information between rigid and deformable components. This coupling strategy leverages the intrinsic properties of the MBD module to effectively constrain the actuator's motion. Additionally, the embedded characteristics of the MBD module allow for the formation of a rigid linkage between components, irrespective of the motion framework. In the coupling strategy, during each time step of the FEA-MBD algorithm, stress and strain are computed using the FE solver, while displacements are determined by the MBD model. Importantly, throughout this process, nodes involved in rigid connections receive stress information from the FE solver to aid in displacement calculations. Additionally, the presence of various rigid connections restricts structural motion to a certain degree, allowing the MBD model to accurately represent the motion characteristics of the multibody system.

3.4 Case study

In this section, various building blocks have been proposed to demonstrate the feasibility of the model-based design strategy. After designing the building block, the selected stimuli will serve as the external condition to activate the smart materials, thus the building blocks can be actuated.

3.4.1 Smart materials and smart mechanism building blocks

The first is the proposition of a particle-based actuator, formulated through model-based design, aims to fulfill the demands for significant deformation and substantial bending stiffness. The analysis of this proposed actuator is conducted utilizing the FEM-DEM approach. The design concept is shown in Figure 3.3, different sized particles are filled into different chambers, separated by a middle layer. The chambers are enveloped by an elastic membrane. During the actuation phase, the membrane undergoes contraction, facilitated by a specified shrinking coefficient, resulting in the deformation of the whole element. This deformation causes the actuator to exhibit a bending motion towards the left, propelled by the discrepancy in volume between the two chambers. Furthermore, subsequent to the contraction process, the actuator's stiffness experiences augmentation due to the phenomenon known as particle jamming. The phenomenon of particle jamming denotes a transition in the packing state of particles. Initially, particles are loosely encapsulated, representing a state of natural packing that permits particle mobility within the membrane. However, as the packing state transitions to a tighter configuration, the spatial arrangement of particles undergoes alteration. Consequently, the inter-particle contact forces and interactions between particles and the membrane intensify, impeding particle mobility. This transition results in the aggregation of particles into a solid-like state, leading to the formation of a jammed configuration.

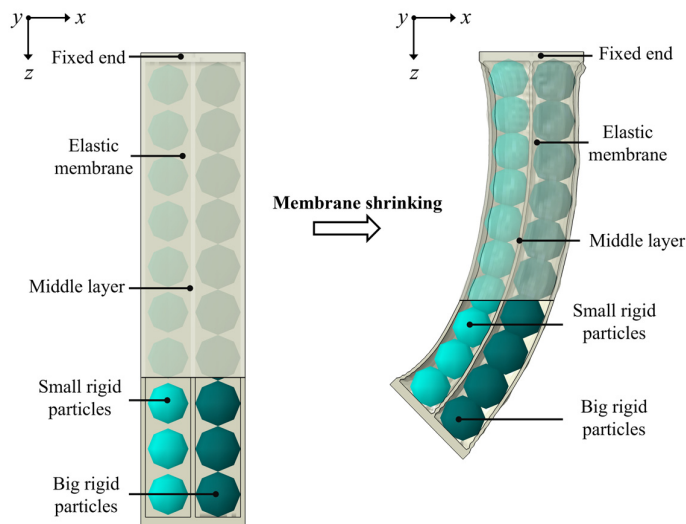


Figure 3.3. The actuation process of the particle-based building block

Secondly, this section explores the properties of hydrogels and materials using the hyperelastic model with FEM. The structure in Figure 3.4 uses a thermally responsive hydrogel linked to a standard soft particle made of silicone or rubber. Initially the same size, the hydrogel swells in water with temperature changes, resulting in a smart element with particles of two different sizes for versatile configurations.

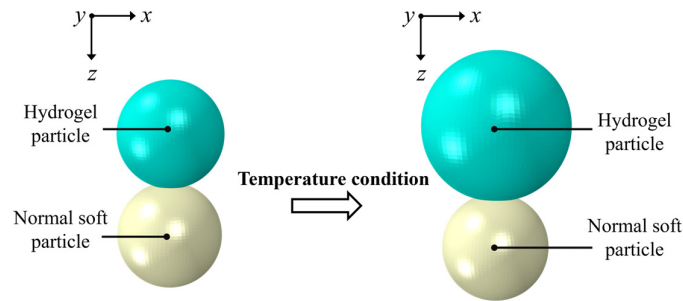


Figure 3.4. Smart element based on hydrogel particle

Smart building blocks are developed using modeled smart elements, as shown in Figure 3.5. Figure 3.5(a) depicts a structure that expands and contracts. It consists of alternating smart elements, where hydrogel particles swell with temperature changes, causing the structure to elongate. The hydrogel particles drive the motion, while normal soft particles provide balance. Temperature change enables the structure's expansion and contraction. Figure 3.5(b) shows a grasping smart building block with a dual-layered framework and four branches. Initially straight, the branches bend inward during hydrogel swelling, constrained by elastic particles, creating a grasping motion.

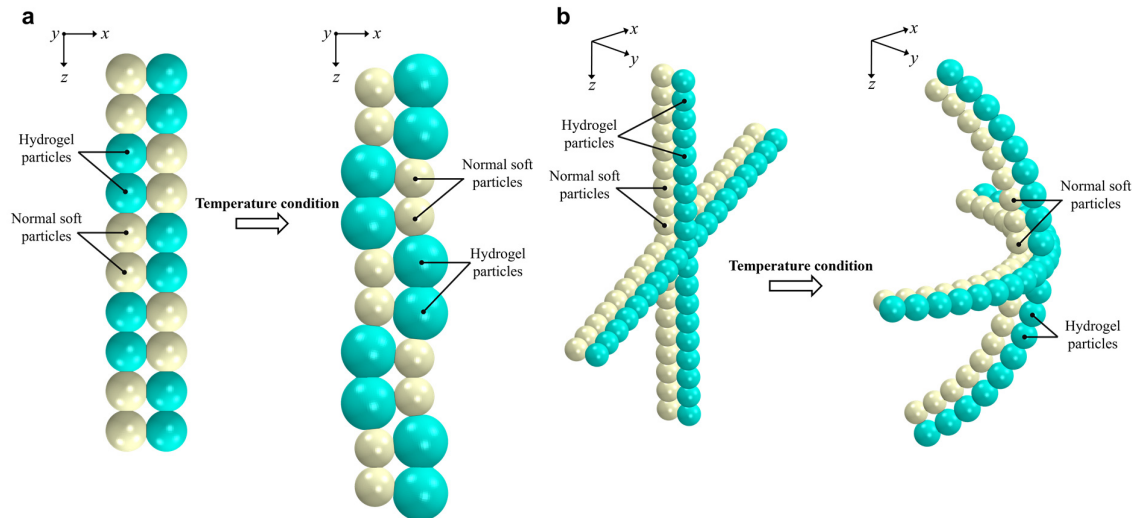


Figure 3.5. Different smart building blocks based on the smart elements (a) *Configuration of elongation structure* (b) *Configuration of grasping structure*

3.4.2 Multiple smart materials based building blocks

In underwater pipe manipulation and seabed maintenance, high temperatures and intense flow present constant challenges for grippers to stabilize or install pipes. In such cases, a gripper capable of operating underwater, actively deforming, and maintaining both high stiffness and adaptability to temperature changes and flow conditions is essential.

The illustration presented in Figure 3.6 depicts the integration of a building block incorporating SMP as its base along with hydrogel protrusions. The SMP base primarily functions as the actuation mechanism facilitating substantial deformation. Conversely, the hydrogel protrusions serve as the supportive framework aimed at enhancing the adaptability of the smart actuator. In the initial state, the SMP base exhibits a curved form, while the hydrogel protrusions maintain a state of minimal swelling. Upon the application of an external force or stimuli, the SMP base undergoes a temporary morphological change. Subsequently, when the temperature surpasses the critical threshold of the SMP, the material reverts to its original shape. Following the shape recovery process, lowering the temperature again serves to both fix the SMP shape and induce further swelling of the hydrogel protrusions. Through this cycle process, the SMP base achieves bending behavior, facilitated by the swelling and contraction of the hydrogel protrusions to modulate the structure's thickness and enhance its adaptability.

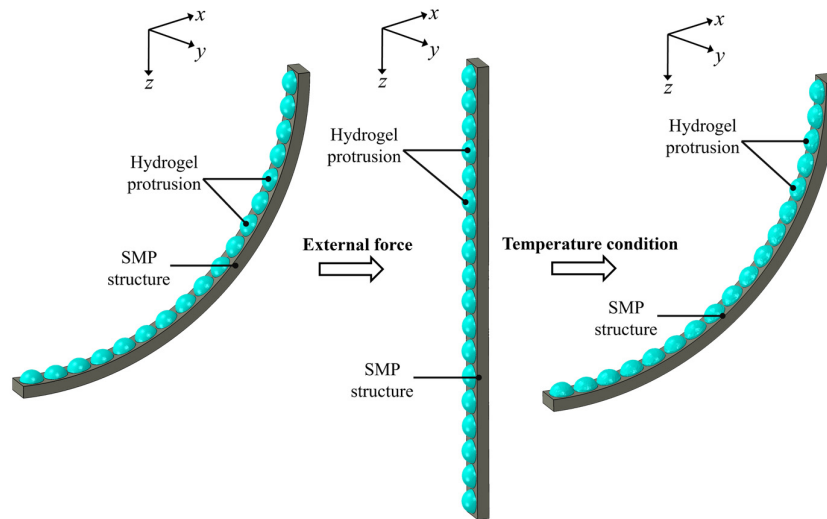


Figure 3.6. The building block based on SMP and hydrogel

As shown in Figure 3.7, the proposed building block exhibits potential for development in specific applications. This potential finds utility within underwater environments for tasks of pipeline maintenance. The operational sequence involves initial deformation of the composite structure through external force, maintaining it in a temporary configuration. Following immersion in water, the entire structure gradually approaches the local section of the pipeline. Subsequently, the pressure valve initiates opening to release high-pressure hot gas. As a result of the elevated temperature of the hot air, adjacent water experiences thermal conduction, leading to its heating. With the increased temperature, the SMP base undergoes bending,

reverting to its original configuration, thus enveloping the pipeline in need of maintenance to ensure safety. Upon the gradual decrease in nearby water temperature, the hydrogel protrusion undergoes swelling, subsequently making contact with both the pipe valve and its outer wall. The inherent softness of the hydrogel structure serves to shield the pipe from potential damage due to collisions. Furthermore, the hydrogel functions to fill the space between the pipe and actuator, thereby promoting pipe stability.

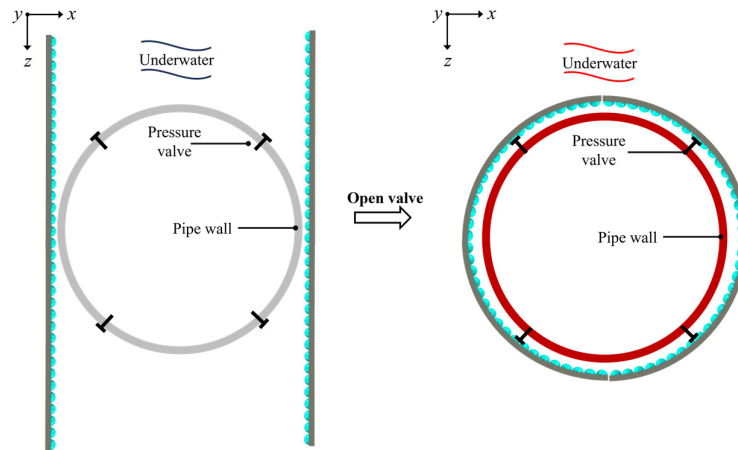


Figure 3.7. Potential application of the multiple smart materials based building blocks

In conclusion, the comprehensive design framework is shown in Figure 3.8. The process begins with the selection of smart materials capable of changing shape, volume, and stiffness in response to environmental stimuli. Replacing conventional soft materials with these smart materials enables energy harvesting from natural sources and reduces dependence on external power, facilitating self-actuation in complex or unpredictable environments. In addition, smart materials like shape memory materials also enable stiffness changes, enhancing adaptability and stability in real-world applications. By combining multiple smart materials, the self-actuation unit, which refers to “building blocks”, can be developed to achieve specific deformations, such as surface folding, shell volume changes, or joint bending. Then, the morphing structures are assembled into more complex structures, which can be modularly configured to perform different behaviors. Finally, the mechanical intelligence relating to the soft robotics can be developed by the structural design based on the morphing structure for various tasks, such as locomotion or manipulation.

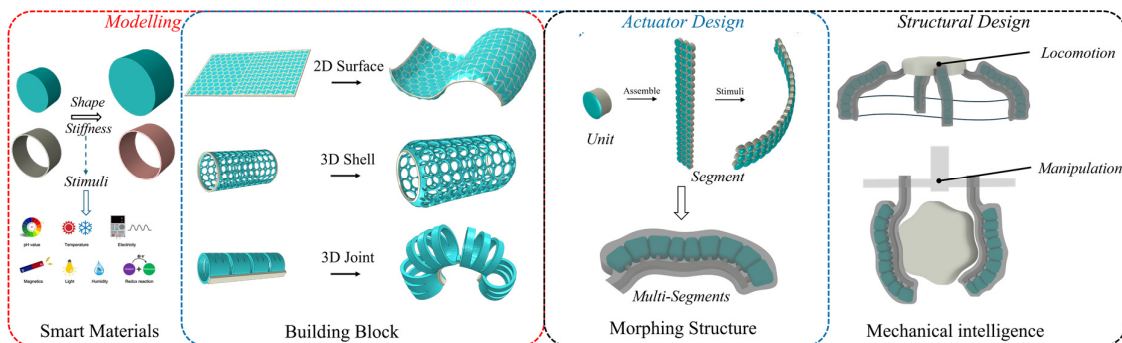


Figure 3.8. The model-based design process of the smart building blocks

3.5 Conclusion

In this chapter, a model-based design framework utilized smart materials is developed, and the design process is proposed to construct the mechanically intelligent structure.

The concept of building blocks, which refers as the modular units, is induced to support the model-based design framework developing smart materials based structure. The building blocks are constructed by integrating the structural geometry, smart material, and external stimuli. Numerical methods, such as the finite element method (FEM) and the coupled method of finite element and discrete element method (FEM-DEM), and multibody dynamics (MBD) offer significant approaches to build model-based design framework.

By employing variable building blocks, it is possible to tailor the functions of these components to specific applications. Particle-based building blocks, for example, demonstrate substantial deformation capabilities and can increase stiffness. Temperature-sensitive hydrogels exhibit active deformation properties, making the building blocks suitable for applications such as elongation and grasping. A hybrid design combining SMP and smart hydrogel can further enhance these actuators by offering both active deformation and stiffness control, enabling functions such as grasping, installation, and maintenance while improving the adaptability of the modular building blocks.

In the future, this framework will integrate numerical models with experimental validation, ultimately enabling the systematic design and manufacturing of building blocks for mechanical intelligence embedded soft robotic systems. Thus, in the next chapter, the conceptual design of stiffness variable bending building blocks will be developed by this model-design framework and will be validated by experiments.

4 Conceptual design of variable stiffness soft bending building blocks*

The model-based design framework proposed in Chapter 3 provides a systematic approach to developing mechanically intelligent morphing structures. A crucial part of this process is developing the geometry configuration, which is important in the morphing functionality. In this context, employing concept of particle-based units presents a promising solution. The particles group exhibits fluid-like behavior, which benefits it as a filler in a closed cavity to facilitate structural morphing. In addition, the particles group can induce a particle jamming effect, which enables tunable stiffness of the structure. Based on the model-based design framework, this chapter proposes a novel conceptual design of particle-based bending building blocks showing the potentials to construct the mechanically intelligent morphing structures. Section 4.2 proposes the design of building blocks and analyzes the actuating method, including the rigid particles-based unit and smart hydrogel particles-based unit. Section 4.3 describes the numerical approaches for the modeling of building block. Section 4.4 analyzes the performances of the building blocks. The main conclusions and potential applications are presented in Section 4.5.

* This chapter is based on Q. Chen, D. Schott, and J. Jovanova, “Conceptual design of a novel particle-based soft grasping gripper,” *Journal of Mechanisms and Robotics*, vol. 16, no. 5, 2024. <https://doi.org/10.1115/1.4062647>, and Q. Chen, D. Schott, and J. Jovanova, “Model-Based Design of Variable Stiffness Soft Gripper Actuated by Smart Hydrogels,” *Soft Robotics*, 2024. <https://doi.org/10.1089/soro.2023.0185>

4.1 Introduction

The particle jamming effect, as versatile jamming, is widely used in soft robotic grippers [246]. The primary mechanism of particle jamming is the particle packing state's transition. Initially, the particles are first capsuled loosely and show the natural packing state, which allows particles to flow within the membrane. However, when the particle packing state transits to tight packing, the arrangement of particles has been changed. Thus, the contact force between particles and interaction forces between particles and the membrane will be enhanced so that the particles are not allowed to move. Thus the particles group shows a solid-like state and the jamming forms [247]. Based on the particle jamming effect, various soft membrane-wrapped containers are designed to improve performance when grasping irregular and heavy objects [248-250]. Nevertheless, incorporating extra pump stations or power equipment augments the intricacy and mass of the robotic system, posing challenges for achieving the compactness and high power-density demanded by large scale applications.

To realize active actuation, the utilization of smart materials that react autonomously to external stimuli offers potential for applications into soft gripper [36]. Functioning as an active smart material, hydrogel exhibits shape alteration in reaction to specific external triggers, including pH, temperature, light, electric and magnetic fields [251]. The thermally responsive hydrogel, has gained significant interest, owing to the facilitated adjustability and strong compatibility [252]. Thermally responsive hydrogel actuators utilize hydrogel volume alterations triggered by ambient temperature fluctuations, exhibiting targeted large deformations within specific temperature ranges [253]. Furthermore, given the adaptable critical temperature, this attribute proves valuable in applications such as, self-folding bilayers, soft origami, and multi-layer-based soft gripper [254-256]. However, limited to the compliance of the soft materials, soft robotic grippers have always been used on objects across a range of scales only from hundreds of μm to a few centimeters and perform poorly with large scale or heavy objects. Inspiringly, the promising properties of using the jamming effect in stiffness variation bring the possibility of solving this problem [257].

This chapter first proposes a novel deformable actuator based on the building block utilizing particle jamming effect. The contributions are summarized in several points. First, the design is a dual-chambers structure that uses rigid and deformable particles combined with the flexible membrane as carriers. The dual –chambers actuator can achieve large bending deformation by membrane shrinking or particles expanding, and different bending behaviors can be achieved by controlling the design parameters including particle diameter ratio, actuator length, and material property. Compared with traditional pneumatic and single-chamber particle jamming actuators, the proposed concept design can improve the bending angle and bending stiffness significantly. Furthermore, a bidirectional discrete element method and finite element method (DEM-FEM) coupling numerical model is presented to analyze the load and the deformation of the elastic chamber interacted by particles, which brings a novel approach to characterize the motion and stiffness of the particle jamming-based actuators.

Then, this chapter introduces a novel soft gripper driven by active smart hydrogels building block, enabling large deformations and variable stiffness. The contributions include several

aspects. First, the swelling and shrinking behaviors of the temperature-sensitive hydrogel spheres are utilized as the basic actuating principle to drive the gripper. Then, the gripper actuator is uniquely designed as a flexible structure made of silicone membrane with separate units filled with hydrogel spheres. Subsequently, an examination of the bending stiffness, which pertains to loading capacity, is conducted. A method for enhancing stiffness is then suggested to enhance the bending stiffness of the actuator. Compared to current actuation methods, our design eliminates the need for additional equipment, and its triggering conditions are relatively easy to implement. Consequently, the proposed gripper benefits in scenarios requiring large-scale, in non-immediate responses, such as the installation and stabilization of sizable objects in underwater or in surface vehicles, particularly in offshore engineering.

4.2 Conceptual design of the smart building blocks

4.2.1 Theoretical background

The proposed actuator is inspired by the bender configuration of active compliant structures [258-261]. The bending curvature of a large deflection bender modular is shown in Figure 4.1. The δ_x and δ_z are the horizontal and vertical displacements at the free end, respectively, and ϕ_{max} refers to the maximum slope of the bender. It is assumed that the length of the middle layer between the two parts of the bender always remains the same.

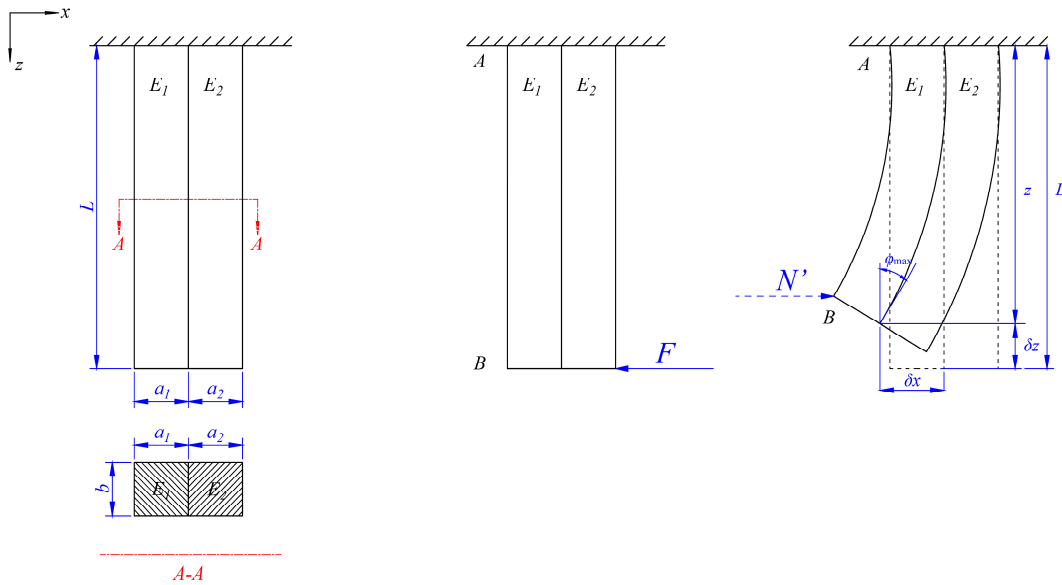


Figure 4.1. The cantilever beam of length L

If the right part of the bender with the elastic modulus E_1 has a maximum expansion of Δl , the maximum curvature $1/\rho$ of the bender can be described as,

$$\frac{1}{\rho} = \frac{\Delta l}{\frac{a_1 + a_2}{2} + \frac{2(E_1 I_1 + E_2 I_2)}{a_1 + a_2} \left(\frac{1}{E_1 a_1} + \frac{1}{E_2 a_2} \right)} \quad (4.1)$$

Thus, the equivalent external force F can be described as,

$$F = \frac{1}{\rho} \left(\frac{2}{(a_1 + a_2)a_1} (E_1 I_1 + E_2 I_2) + \frac{E_1 a_1}{2} \right) \quad (4.2)$$

In addition, $\varphi_{max} = 180L/\pi\rho$, and consider the bender as a whole and the equivalent elastic modulus \bar{E} and the equivalent moment of inertia \bar{I} , the x and z coordinates of the horizontal and vertical deflection at any point along the neutral axis of the bender are found as follows,

$$z = \left| \sqrt{\frac{2\bar{E}\bar{I}}{F}} (\sqrt{\sin\varphi_{max}} - \sqrt{\sin\varphi_{max} - \sin\varphi}) \right| \quad (4.3)$$

$$x = \left| \sqrt{\frac{\bar{E}\bar{I}}{2F}} \int_0^\varphi \frac{\sin\varphi d\varphi}{\sqrt{\sin\varphi_{max} - \sin\varphi}} \right| \quad (4.4)$$

$$\delta_x = x(\varphi_{max}), \delta_z = L - z(\varphi_{max}) \quad (4.5)$$

It can be seen that φ_{max} , δ_x , and δ_z are affected by the beam's equivalent elastic module \bar{E} , the equivalent moment of inertia \bar{I} , and the bender length L .

Additionally, the bending stiffness of the actuator is represented as S_a , which can be described as,

$$S_a = \frac{N' z'}{\varphi_{max} - \varphi'} \quad (4.6)$$

where N' is the external interaction when the actuator touching with objects, z' is the new vertical position point, and φ' is the bending angle affected by N' .

4.2.2 Building blocks design

4.2.2.1 Rigid particle-based building block design

To describe the bending behavior of the proposed gripper, the structure of the actuator is discussed. First, it is assumed that all the materials used in the actuator are incompressible and the effect of gravity is not considered. In order to draw the concept of smart elements with engineered particles, two strategies of driving modes are used in the conceptual design stage, which is called expansion mode and shrinkage mode, respectively. For the expansion mode, as shown in Figure 4.2, the covered membrane is made of conventional elastic material. Here, the particles in the right chamber will expand actively with a certain expansion coefficient to deform the whole structure. For the shrinkage mode, as shown in Figure 4.3, a reverse process by controlling the behaviors of the membrane is considered. Different-sized rigid particles are filled into different chambers in one element, while the covered membrane is set to shrink with a certain shrinking coefficient to deform the whole element.

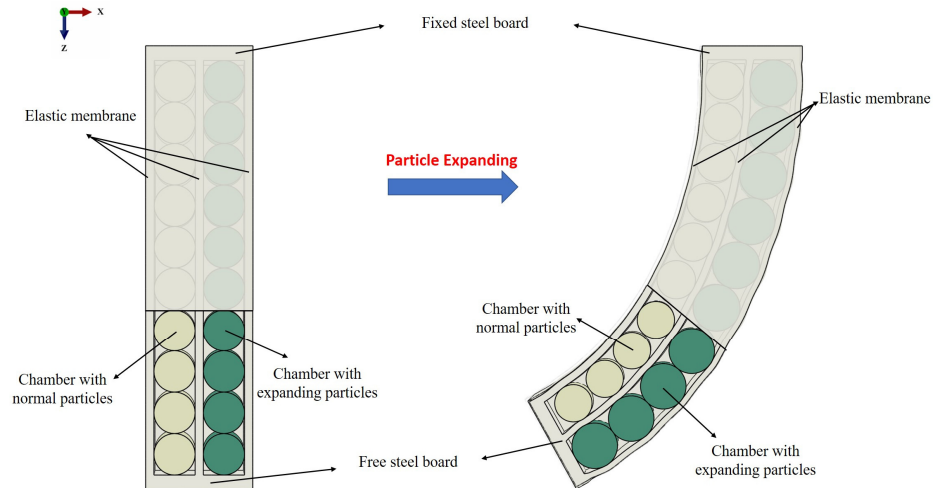


Figure 4.2. Actuator working process of the expansion mode

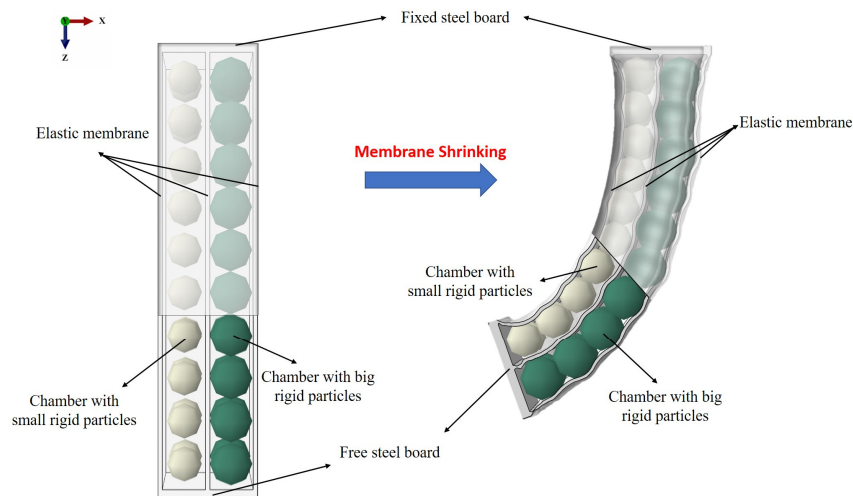


Figure 4.3. Actuator working process of the shrinkage mode

Furthermore, to validate the feasibility of the proposed design, two experimental cases are conducted as proof of concept of both the expansion and shrinkage modes. The experiments with the actuator's expansion and shrinkage modes are illustrated in Figure 4.4 and Figure 4.5, respectively. In Figure 4.4 (left) the same-sized rigid particles fill both chambers, which are covered by an Ecoflex-00-50 (Smooth-On Company) silicone membrane. Then, the bigger green particles are used instead of the initial ones to represent the expanding process. Now, the actuator structure bends towards the left after adding the particles in, providing demonstrating proof of the principle of the expansion mode. Additionally, Figure 4.5 demonstrates the shrinkage mode. First, the small rigid white particles and big rigid green particles are filled into the left chamber and right chamber, respectively. The total volume of the small white particles is smaller than the volume of the chamber, thus the particles in the left chamber show a loose packing state in the beginning. Both chambers are covered by the silicone membrane. Then, as shown in Figure 4.5 (right), the smaller chambers which have the same volume of small particles group are used instead to present the membrane-shrinking process. The result

demonstrates that the actuator bends toward the left, indicating that shrinkage mode can also achieve the actuator's bending. Moreover, the bending performance in these experimental cases will be used to compare and validate the simulation results.

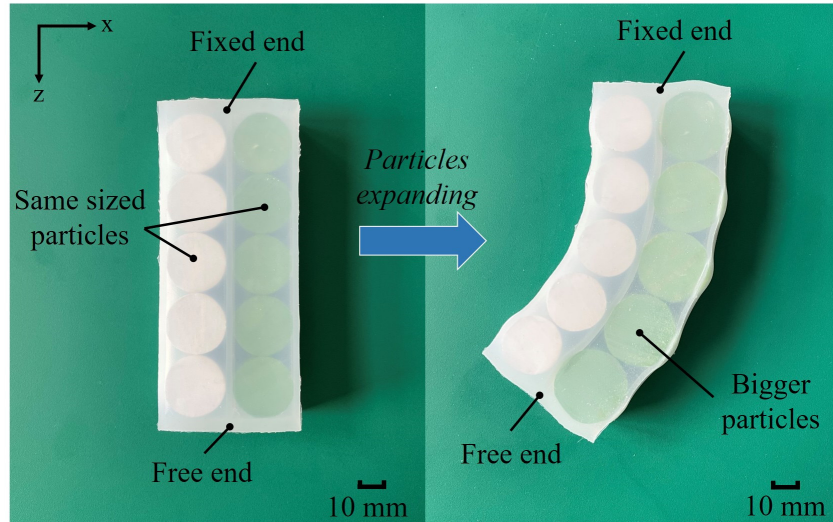


Figure 4.4. The demonstration of the actuator of expansion mode

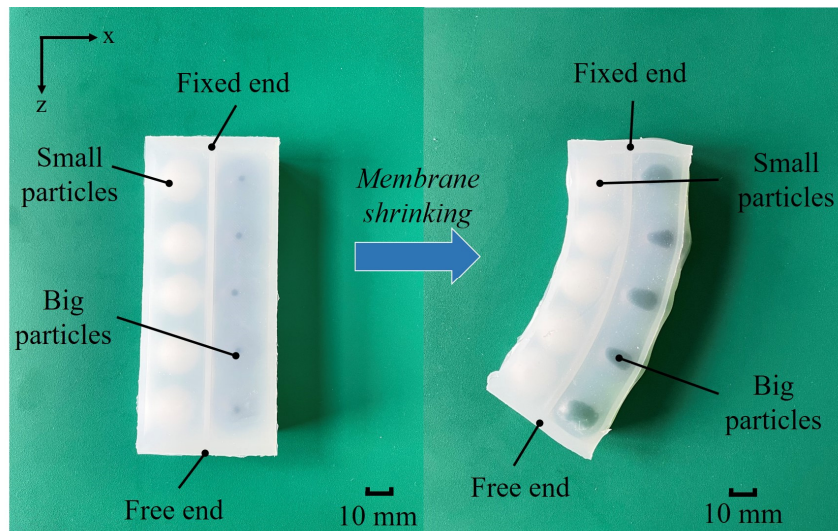


Figure 4.5. The demonstration of the actuator of shrinkage mode

Additionally, as shown in Figure 4.6, the geometric parameters of the actuator are defined as follows: the general structure has two chambers. The membrane at the length of L is fixed on the top and accessible at the end. The thicknesses at the top and the bottom are t_1 , while the thicknesses of the outer membrane on both sides are t_0 . It contains two layers with different widths a_1 and a_2 . The two layers are connected by a thin film at a thickness of t_2 in between. Each chamber will be filled with particles with diameters of d_1 and d_2 , respectively.

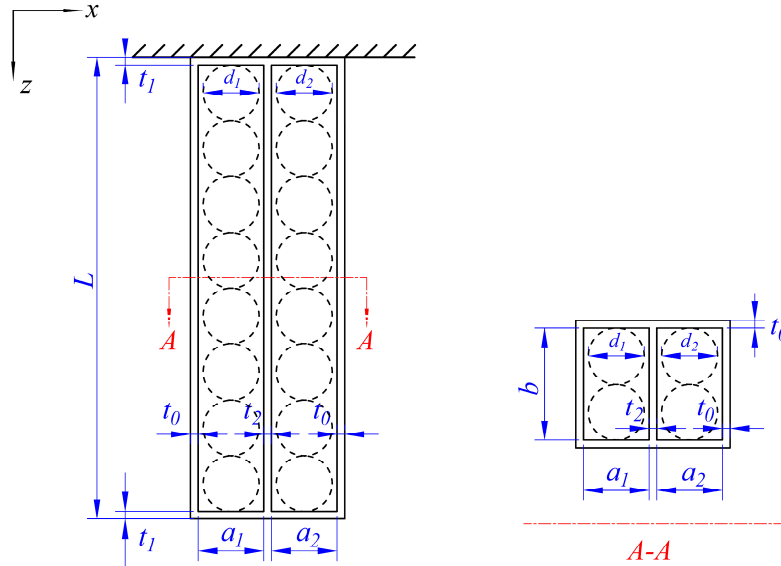


Figure 4.6. A front view and the cross-section view of the actuator structure

Additionally, considering different independent influential parameters, variable simulation cases were conducted as the sensitivity analysis to investigate the behaviors of the proposed actuator. The first set of simulations investigates how particle size differences influence the actuator's behaviors. The second set of simulations explores how the major structural parameters influence the actuator's behaviors. The last set of simulations investigates how the membrane's material property influences the soft actuator's behaviors. It should be noted that in the last set of simulations, the linear model is used instead of the hyperelastic model in the simulations for analyzing the effects of materials with an extensive range of stiffness on the bending performance. Thus, all materials are assumed to be with a fixed elastic modulus. Besides, different driving modes of the actuator are also compared. The specific actuator parameters are shown in Table 4.1, and the material's properties are shown in Table 4.2.

Table 4.1 Actuator parameters

Driving modes	Particle diameter ratio β_{1s}	Actuator Length L (mm)	Other sizes (mm)
Shrinkage mode	1 - 2	28 - 448	$a_1 = a_2 = 20$
Expansion mode			$t_0 = t_2 = 2$
			$t_1 = 4$
			$b = 40$

Table 4.2 Materials properties

	Particles	Membrane	End board
Density (kg/m^3)	$\rho_p = 1180$	$\rho_m = 950$	$\rho_b = 7800$
Elastic modulus (MPa)	$E_p = 2910$	$E_m = 50 \sim 60000$	$E_b = 210000$
Poisson's Ratio	$\nu_p = 0.38$	$\nu_m = 0.48$	$\nu_b = 0.32$

4.2.2.2 Hydrogel particle-based design

Typically, the particle jamming effect achieves by the pneumatic system. Our design uses smart deformable particles instead to accomplish the jamming effect. As shown in Figure 4.7, different soft particles fill the chamber, which can achieve the action of expanding or deforming by external stimuli. After the dynamic behaviors, the arrangement of particles and the total volume of the particle group will change. Thus, particles jam with each other due to the increasing interaction between particles.

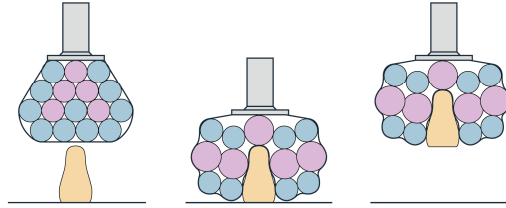


Figure 4.7. Illustration of the active particle jamming actuator

The gripper actuator, as illustrated in Figure 4.8, consists of a silicone structural body with discrete units as chambers. Each chamber contains a uniform temperature-sensitive hydrogel sphere. The designed actuator select the poly (N-isopropylacrylamide) (PNIPAM) as the utilized hydrogel. When the temperature falls below the critical point, PNIPAM experiences one-way swelling behavior due to the absorption of water molecules, and when the temperature exceeds critical temperature (306 K), PNIPAM shrinks as it releases water molecules [262]. The spherical design ensures symmetrical volume for water accommodation, while multiple chambers prevent unrestricted sphere movement. A strain-limit layer on the left side restricts left-layer extension, and the top layer serves as a fixed point to secure the gripper without structural deformation. The slope of the actuator is characterized as bending angle φ .

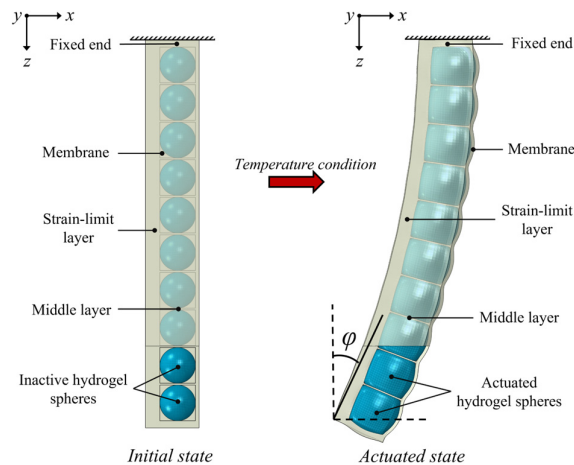


Figure 4.8. The working principle of the hydrogel based design

Figure 4.8 also illustrates the working principle. It involves two states: initial and actuated. In the initial state, inactive hydrogel spheres fill the chambers without any force. As temperature changes, the hydrogel spheres expand and interact with silicone chambers, causing the

membrane to extend due to interaction forces. The strain-limit layer limits left-side elongation, causing bending. When the hydrogel spheres swell significantly, maximum bending occurs, transitioning to the actuated state.

In addition, the detailed structure design is shown in Figure 4.9. Each unit fills hydrogel sphere with the diameter of d . The total length of the structure is L . The thicknesses at the top and the bottom are t_1 , while the thicknesses of the outside membrane on both sides are t_0 . Different units are separated by the middle layer with the thickness of t_2 . The strain-limit layer is on the left of the thickness of t_3 .

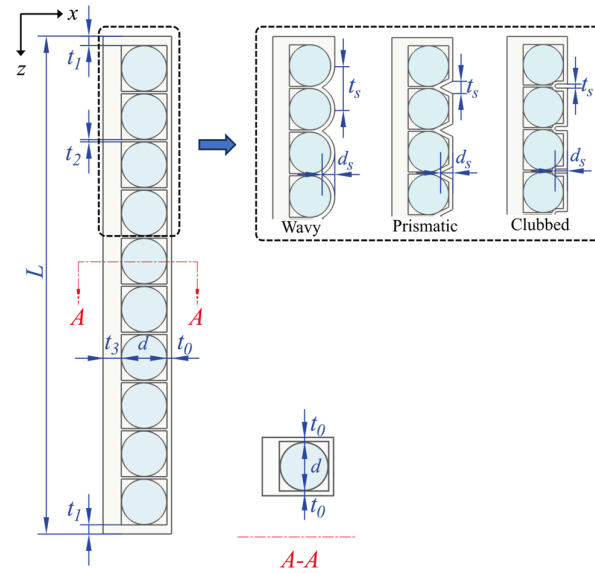


Figure 4.9. The geometric parameters of the structure

Furthermore, various structures are model designed to investigate the effects of geometric factors on the bending performance. The designs, derived from the initial straight design, feature gaps on the right side. The depth d_s of each shape is same and set to 6.2 mm, while the difference between different designs is the width t_s , which is 20 mm, 6 mm, and 2 mm for the clubbed, wavy, and prismatic configurations, respectively.

4.3 Methodology

FEM and the DEM-FEM coupling method are used for modeling. FEM describes the nonlinear behaviors of the smart hydrogels. Additionally, for the small amount of rigid particles, DEM can describe the interactions at the particle level in granular materials with low computing resource consumption compared to traditional FEM. Besides, the FEM-DEM has already been proven as a more efficient and realistic method to solve the interaction between rigid particles and elastic boundaries [263].

4.3.1 FEM-DEM model and implementation

4.3.1.1 Numerical model

Both the discrete elements and the finite element node motions are governed by Newton's Second Law. First, the external force F_i^{fem} for finite element node i is given by,

$$F_i^{fem} = m_i^{fem} \left(\frac{d^2 u_i^{fem}}{dt^2} \right) \quad (4.7)$$

where m_i^{fem} is the mass of element i and u_i^{fem} is the displacement of element i . And the total force F_i^{dem} for discrete element node i , which composites of all collision force F_i^c , gravitational force F_i^g , and external force F_i^e , is given by,

$$F_i^{dem} = F_i^c + F_i^g + F_i^e = m_i^{dem} \left(\frac{d^2 u_i^{dem}}{dt^2} \right) \quad (4.8)$$

where m_i^{dem} is the mass of individual particle i and u_i^{dem} is the displacement of discrete element i . In addition, the centroidal moment of element i of the discrete element i is given by [244],

$$M_i = I_i \left(\frac{d^2 \theta_i}{dt^2} \right) \quad (4.9)$$

where I_i is the inertia moment of element i and θ_i is the rotation angle of element i . The equation (4.7)-(4.9) are solved using an explicit finite difference method based on the commercial platform ABAQUS.

Contact detection is necessary to calculate the interaction forces among the elements. The C-grid method is applied for the contact detection of the elements [264]. Besides, the node-to-surface method consists of a global search. Local search is used as the contact detection between the spherical discrete elements and the hexahedron finite meshes [265]. In this method, the discrete elements are regarded as the slave nodes, and the contact surfaces of the finite elements are regarded as the master surfaces. Global research determines the potential contact pairs, and the local search calculates the penetration value between the contact pairs. The interaction forces among the elements strongly depend on the contact model between contact pairs. The contacts of particle-to-particle and particle-to-surface are shown in Figure 4.10. The overlap between discrete elements and discrete and finite elements, which represents the small deformation of the discrete element, is δ_{ij} . Moreover, the linear velocities and angular velocities of elements i and j are v_i , v_j , ω_i , and ω_j , respectively. It needs to be noted that there is no angular velocity in the finite elements.

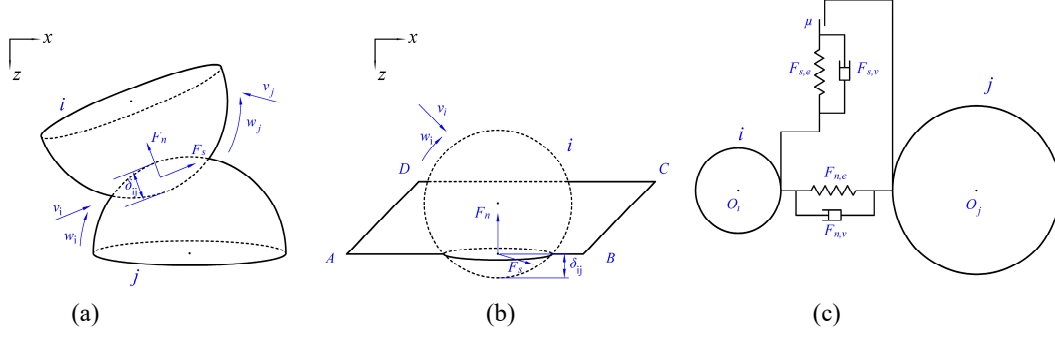


Figure 4.10. Schematic of contact interaction and contact force of particles and wall surface (a) The overlap between two particles (b) The overlap between particle and the wall surface (c) The contact with spring, damper in both tangential and normal direction as well as sliding contact

The normal force F_n , and the tangential force F_s can be written as ,

$$F_n = F_{n,e} + F_{n,v} \quad (4.10)$$

$$F_s = \begin{cases} F_{s,e} + F_{s,v} & |F_s| < f|F_n| \\ fF_n & |F_s| \geq f|F_n| \end{cases} \quad (4.11)$$

where, $F_{n,e}$, and $F_{n,v}$ represent the normal spring force and the normal damping force, respectively; $F_{s,e}$, and $F_{s,v}$ represent the tangential spring force and tangential damping force, respectively. The friction coefficient is shown as f . The $F_{n,e}$, $F_{n,v}$, $F_{s,e}$, and $F_{s,v}$ can be calculated by Hertz-Mindlin theory [266]. Specially, there is an assumption that finite elements are regarded as spheres with infinite radii [267]. The $F_{n,e}$, and $F_{s,e}$ are shown as,

$$F_{n,e} = \frac{4}{3} E^* \sqrt{R^*} \delta_{ij}^{\frac{3}{2}} \quad (4.12)$$

$$F_{s,e} = \frac{16}{3} G^* \sqrt{R^*} \delta_{ij}^{\frac{3}{2}} |u^*| \quad (4.13)$$

where R^* is the equivalent radius of the contact elements, which can be obtained by $R^* = (r_1 r_2) / (r_1 + r_2)$; the E^* and G^* are the relative elastic modulus and shear modulus, which can be illustrated as ,

$$\frac{1}{E^*} = \frac{1 - \nu_i^2}{E_i} + \frac{1 - \nu_j^2}{E_j} \quad (4.14)$$

$$\frac{1}{G^*} = \frac{2 - \nu_i^2}{G_i} + \frac{2 - \nu_j^2}{G_j} \quad (4.15)$$

where E_i , E_j , G_i , G_j , ν_i and ν_j are the elastic modulus, shear modulus, and Poisson's ratios of elements i and j , respectively; and u^* is the relative displacement in the tangential direction which can be calculated by,

$$u^* = \int_0^t v_{s,ij} dt \quad (4.16)$$

The $F_{n,v}$, and $F_{s,v}$ are shown as,

$$F_{n,v} = -\frac{\Phi_n m_i m_j}{m_i + m_j} \cdot v_{n,ij} \quad (4.17)$$

$$F_{s,v} = -\frac{\Phi_s m_i m_j}{m_i + m_j} \cdot v_{s,ij} \quad (4.18)$$

where Φ_n and Φ_s represent the damping factors of normal and tangential directions; $v_{n,ij}$, and $v_{s,ij}$ represent the relative velocities of the normal and tangential directions.

4.3.1.2 Coupling strategy

The coupling strategy is shown in Figure 4.11. First, the mesh file containing the actual triangulated surface elements and the number of the original finite element FE elements are used as input into the DEM solver as a wall condition [263]. Then, the DEM solver calculates particles' interaction forces, displacements, and velocities in a specific DEM time step. The next step is calculating the node forces based on the particle load and then transferring them into each FEM element. Furthermore, the node forces must be transferred to a distributed load to interpolate them onto each FE element. Consequently, the deformations of mesh elements and displacements of nodes can be calculated. The deformed mesh will update the old grid information to the DEM solver, which is a complete coupling FEM time step which is a multitude (default value, 10) of the minor DEM time step.

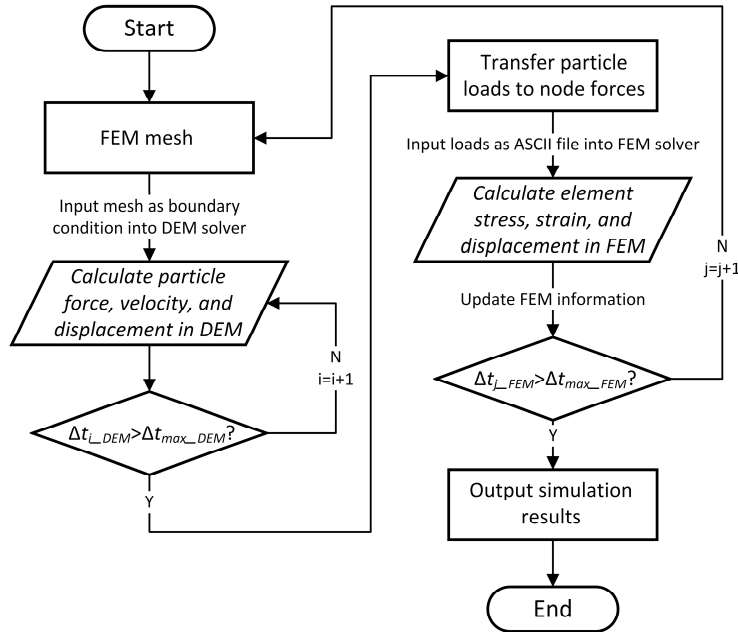


Figure 4.11. Schematic of coupling strategy

4.3.1.3 Simulation setup

In the shrinkage mode, the membrane is set to finite element units and the particles are established by DEM. However, in expansion mode, both the membrane and particles are set to finite element units. The structured mesh is used to establish the finite element units, and after mesh convergence analysis, the hexahedral mesh is selected and the mesh numbers are set to

92,267 and 3,657 for membrane and particles in expansion mode. Besides, the Noe-Hookean model is used as the constitutive model to characterize the mechanical property of the membrane made of Ecoflex-00-50. The fitted parameters of μ , denoting the coefficient depending on the material property, is given by $\mu = 0.0481$ [268]. In order to achieve the shrinking process, the membrane material was set thermos-sensitive with a constant shrinking rate coefficient $\gamma = -0.01$, which is triggered by temperature increase. Furthermore, as for the expansion mode, the membrane is set as normal elastic material without any thermal response. Instead, the filling particles are thermos-sensitive, with an expansion coefficient of $\alpha = 0.01$. The membrane shrinking strain ε_s , and particle expansion strain ε_e can be described as:

$$\varepsilon_s = \gamma(T_1 - T_0) \cdot t \quad (4.19)$$

$$\varepsilon_e = \alpha(T_1 - T_0) \cdot t \quad (4.20)$$

where T_0 is the initial temperature with a constant value of 300K, T_1 is the operating temperature which is set to 330K. t represents the total simulation time, 10s. And for both simulations, the time step is set to constant with $\Delta t = 10^{-6}$ s.

As an example, the shrinking process of a total simulation time is shown in Figure 4.12, the overall structure bends toward the layer of small particles with the shrinking of the membrane. In the initial stage, the elastic membrane covering the particles assumes a cubic structure. During the working phase, the membrane shrinks and interacts with particles continuously over time, and the difference in particle sizes in the two chambers causes the different shrinking extents, which eventually results in bending.

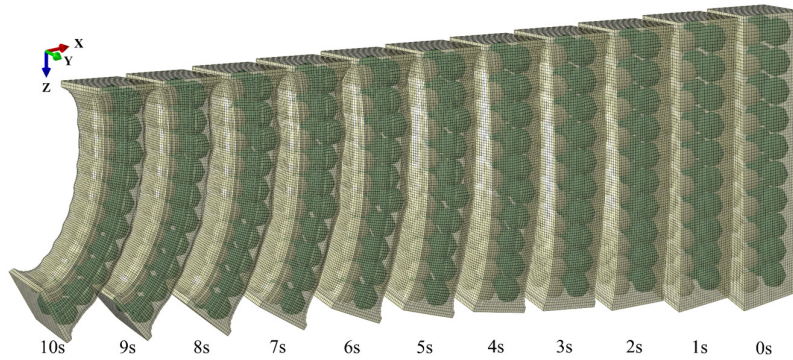


Figure 4.12. The bending process as a function of time with membrane shrinking mode

As shown in Figure 4.13, the bending performance of the proposed actuator is indicated by bending angle and deflections. The δ_x and δ_z are the horizontal and vertical displacements at the free end, respectively. The φ_{max} refers to the maximum slope of the actuator element.

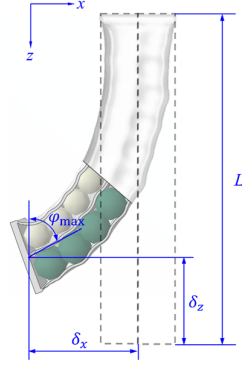


Figure 4.13. The illustration of the bending angle and deflection of the actuator

4.3.2 FEM model and implementation

4.3.2.1 Temperature-sensitive hydrogel model

The PNIPAM can be characterized using the Helmholtz free energy model [262],

$$W = W_s + W_m \quad (4.21)$$

where W_s arises from the elongation of the polymer network, while W_m represents the energy associated with the mixing of the polymers and the solvent. The free energy arising from the elongation of a polymer network is considered as [269],

$$W_s = \frac{NkT}{2} [F_{ik}F_{ik} - 2 \log(\det \mathbf{F}) - 3] \quad (4.22)$$

The energy of mixing of the extended polymer with the solvent is considered as [270],

$$W_m = kT[C \log \phi \nu C + \phi \chi C] \quad (4.23)$$

where N represents the count of polymer chains per unit dry volume, kT denotes temperature expressed in energetic units, \mathbf{F} stands for the deformation gradient concerning the dry network, ϕ corresponds to the volume proportion of the polymer in the hydrogel matrix. χ is a dimensionless parameter quantifying the potency of intermolecular interactions between constituent entities, which is in the empirical adjustment of experimental data, adopting the subsequent formulation [271],

$$\chi(T, \phi) = \chi_0 + \chi_1 \phi \quad (4.24)$$

where χ_0 and χ_1 are the temperature related parameters and expressed as,

$$\chi_0 = A_0 + B_0 T, \quad \chi_1 = A_1 + B_1 T \quad (4.25)$$

The values A_0 , B_0 , A_1 , and B_1 of PNIPAM hydrogel are given by experiments as -12.947 , 0.04496 , 17.92 , and -0.0569 , respectively [272]. In addition, ϕ can be described as,

$$\phi = \frac{1}{1 + \nu C} \quad (4.26)$$

where C represents the nominal concentration of solvent water molecule and v denotes the volume attributed to an individual water molecule.

Furthermore, the chemical potential denoted as μ , constitutes another important material property parameter utilized for characterizing the hyperelastic behavior of hydrogels within numerical models, necessitating its constancy within a state of equilibrium. Hence, the free energy function can be alternatively formulated using a Legendre transform [221],

$$\widehat{W}(\mathbf{F}, T, \mu) = W - \mu C \quad (4.27)$$

The constraint relation between \mathbf{F} and C is expressed as [273],

$$\det(\mathbf{F}) = 1 + vC \quad (4.28)$$

Then the volume ratio J is induced to donate the third deformation gradient tensor. Thus the free energy function can be obtained by using the equations (4.21)-(4.23) and equation (4.28),

$$\widehat{W}(\mathbf{F}, T, \mu) = \frac{1}{2} NkT(J^{\frac{2}{3}}\bar{I}_1 - 3 - 2 \log(J)) + \frac{kT}{v} \left[(J - 1) \log \frac{J - 1}{J} + \frac{\chi(T, J)}{J} \right] - \frac{\mu}{v} (J - 1) \quad (4.29)$$

where $\bar{I}_1 = F_{iK}F_{iK}$, which represents the first invariants of the deformation gradient tensor.

PNIPAM hydrogel is investigated through the FEM approach capable to capture the responsive behavior, along with the implementation of user-defined codes [240].

In the case where $J = 1$, the free energy density exhibits a singularity. The issue of singularity can be addressed by selecting a reference state with a value of $J > 1$ [215]. In this study, the chosen reference state corresponds to a free state configuration of the network, devoid of any mechanical loading. It attains equilibrium alongside a solvent possessing a chemical potential denoted as μ_0 , all transpiring at a designated reference temperature denoted as T_0 . Consequently, it is also necessary to introduce an initial swelling ratio λ_0 .

For the free swelling, the swelling ratio in different directions has the relation as,

$$\lambda_1 = \lambda_2 = \lambda_3 = \lambda_0 \quad (4.30)$$

Thus, the equilibrium state can be articulated as follows,

$$\frac{\mu_0}{kT_0} = \frac{Nv}{\lambda_0^3} (\lambda_0^2 - 1) + \log \left(1 - \frac{1}{\lambda_0^3} \right) + \frac{1}{\lambda_0^3} + \left(\frac{\chi_0 - \chi_1}{\lambda_0^6} + \frac{2\chi_1}{\lambda_0^9} \right) \quad (4.31)$$

Relative to the dry network, the condition of free swelling can be delineated through the deformation gradient,

$$\mathbf{F}_0 = \begin{bmatrix} \lambda_0 & 0 & 0 \\ 0 & \lambda_0 & 0 \\ 0 & 0 & \lambda_0 \end{bmatrix} \quad (4.32)$$

Let \mathbf{F}' denote the deformation gradient and J' represent the volume ratio relative to the free swelling state,

$$\mathbf{F} = \mathbf{F}_0 \mathbf{F}' \quad (4.33)$$

$$J = \lambda_0^3 J' \quad (4.34)$$

Using the free swelling state as the reference state, the nominal free energy density is expressed as,

$$\begin{aligned} \widehat{W}(\mathbf{F}', T, \mu) = & \frac{1}{\lambda_0^3} \left\{ \frac{1}{2} NkT \left[\lambda_0^3 J'^{\frac{2}{3}} \bar{I}_1 - 3 - 2 \log(\lambda_0^3 J') \right] \right. \\ & + \frac{kT}{\nu} \left[(\lambda_0^3 J' - 1) \log \left(\frac{\lambda_0^3 J' - 1}{\lambda_0^3 J'} \right) + (\lambda_0^3 J' - 1) \cdot \left(\frac{\chi_0}{\lambda_0^3 J'} + \frac{\chi_1}{\lambda_0^6 J'^2} \right) \right] \\ & \left. - \frac{\mu}{\nu} (\lambda_0^3 J' - 1) \right\} \quad (4.35) \end{aligned}$$

the equation (3.35) constitutes the fundamental basis function FEM simulations.

In addition, the covered silicone membrane exhibits characteristics of hyperelasticity, thereby manifesting a stress-strain correlation of nonlinear behavior. To describe this particular stress-strain relationship, the finite element solver incorporates the Neo-Hookean constitutive model, thus facilitating the delineation of the material attributes [274]. The strain energy density function for an incompressible material is as,

$$W_{\text{NH}} = \mu_{\text{NH}} (\bar{I}_1 - 3) \quad (4.36)$$

where μ_{NH} is a material constant, \bar{I}_1 is the first invariants of the deformation gradient tensor.

4.3.2.2 Simulation setup

In this study, the ABAQUS commercial finite element software is employed, and a user-defined UHYPER subroutine is developed for modeling the PNIPAM hydrogel. Before integration into the all-polymer structure, the hydrogel was assumed to be existed in a homogeneous free swelling state after synthesis. The equilibrium state is characterized by λ_0 fixed to 1.926 in the simulation, which corresponds to an equilibrium state of $\mu = 0$ for the material of the hydrogel. Besides, $N\nu$ represents the crosslink density of a representative hydrogel. In addition, the swelling process is simplified into state change rather than the dynamic process, where only temperature serves as the triggering condition for hydrogel swelling. Regarding the silicone membrane, the μ_{NH} should be defined to characterize the materials. In the simulations, diverse nonlinear materials of different μ_{NH} have been employed, as illustrated in Table 4.1 [268].

The hydrogel and silicone membrane exhibit characteristics of soft materials, displaying minimal disparity in relative hardness. Consequently, the hard contact model is adopted for the contacting interface, aiming to minimize the penetration of the slave surface into the master surface at the constraint locations, while concurrently restricting the transfer of tensile stress across the interface. Besides, the friction formulation utilizes an isotropic coefficient of 0.01 to describe tangential characteristics. The mesh is specified individually for each part. The hydrogel balls employ a standard 3D C3D8H (8-node linear brick, hybrid with constant pressure) mesh. However, the 3D C3D4H (4-node linear tetrahedron, hybrid with constant pressure) mesh was chosen for membrane structures to improve mesh quality and convergence by addressing

the existence of thinner and irregular edges. Furthermore, grid independence verification establishes the global mesh sizes for hydrogel balls and membrane structures at approximately 1 and 1.5, respectively. Moreover, in formulating the design concept, emphasis was placed exclusively on the bending performance actuated by hydrogel balls, with the gravitational impact being disregarded. The temperature is used as triggering conditions, alterations in temperature serve as the triggering condition, ranging from 308 K down to 290 K [103].

Table 4.1 Parameters of different materials

Material type	μ_{NH} (Mpa)
Ecoflex 00–30	0.032
Ecoflex 00–50	0.048
Dragon Skin™ 10 MEDIUM	0.079
SOLOPLAST 150318	0.123
Mold Star 20T	0.171
Dragon Skin 20	0.207
Dragon Skin 30	0.242
RTV615	0.339

4.4 Results and discussion

4.4.1 Sensitive analysis of rigid particle-based building block

4.4.1.1 Comparison of the bending performances and driving modes

To validate the bending performances of the designed actuator, the detailed results of experiments and simulations are compared. As for the experimental cases, the reference point at the actuator's free end is selected to describe the displacements. Besides, the coordinate paper is used to quantify the motion range of the actuator. The displacements in the x direction and z direction are represented as U_x and U_z , respectively. The results are shown in Figure 4.14, the error bars are the displacement differences of the experimental cases which are tested for 3 times. In addition, the coordinate origin represents the initial state, and the bending process is shown as the configuration shown in Figure 4.14. The simulation results show good consistency with the experimental case results in the moving displacement at the free end, further proving the feasibility of the design.

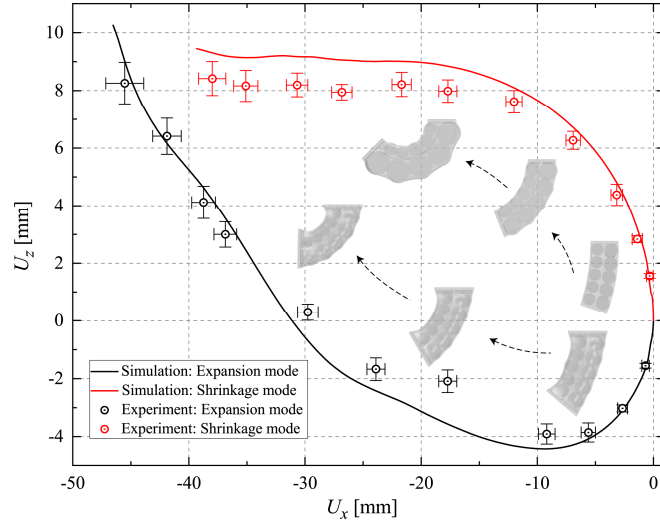


Figure 4.14. The displacements in x direction and z direction of simulation results and experimental results of the proposed novel actuator

Furthermore, the bending angle and the stiffness of the shrinkage mode are compared with pneumatic and single-chamber particle jamming actuators to evaluate the design concept [275]. The parameter J' represents the volume ratio between the cavity (with smaller particles) before and after shrinkage. For other actuators, J' is the volume ratio between the bending state and the initial state. Essentially, J' is the volume difference before and after deformation. As shown in Figure 4.15, the bending angle of all actuators increases as the volume ratio increases. Compared with the pneumatic actuator, the bending angle of our proposed particle-based actuator increases more sharply and exhibits a maximum six-fold increase. Compared with the particle jamming actuator, the trend of the bending angle change is similar, however, our design can obtain an extra 8 degrees bending angle at the maximum volume ratio. As shown in Figure 4.16, the bending stiffness of our design and the particle jamming actuator increases sharply as the volume ratio increases, but the bending stiffness of the pneumatic actuator changes very less. Compared with the pneumatic actuator, the bending stiffness of our design exhibits a maximum nine-fold increase. Compared with the particle jamming actuator, the trend of the bending stiffness change is also similar, but our design exhibits greater stiffness across the range of volume ratio from 1.2 to 1.8.

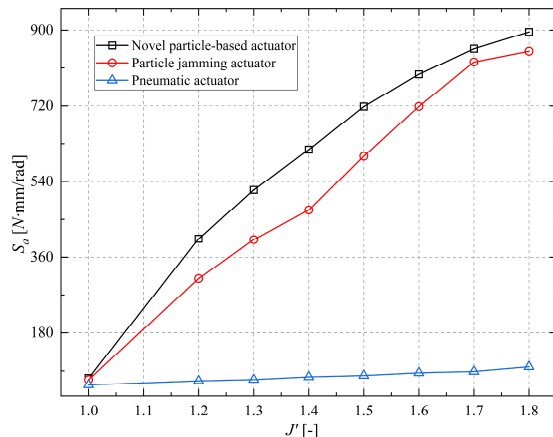
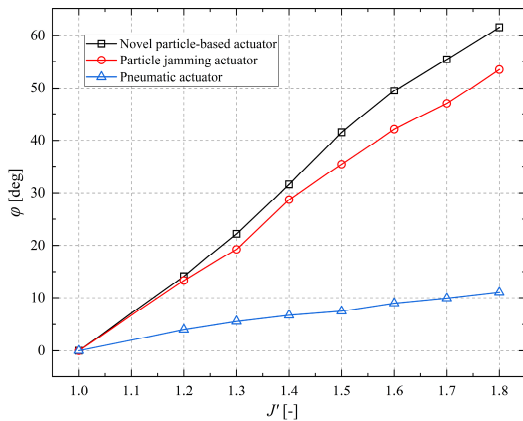


Figure 4.15. The bending angle comparison of the proposed design and [275]

Figure 4.16. The bending stiffness comparison of the proposed design and [275]

The bending performances of different driving modes are also compared. The bending performances of different β_{ls} actuated by different driving modes are compared in Figure 4.17. Generally, the shrinkage mode and the expansion mode show good agreement in the bending curvature. Individually, the angle difference between the two driving modes rises gradually as β_{ls} increase, but the maximum difference value is only up to 30 degrees.

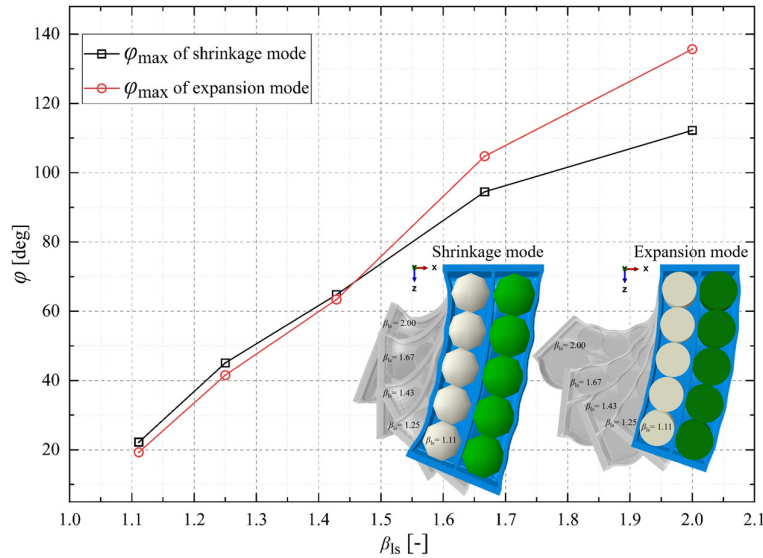


Figure 4.17. Comparison of bending angles of different driving modes with different β_{ls}

To further explore whether expansion and shrinkage modes can achieve similar bending performance, as shown in Figure 4.18, the effects of the actuator length on the bending performance of different driving modes are analyzed. Firstly, both driving modes' bending angle curves increase gradually, dropping within a specific range of L and then going up again until L comes to 448 mm. Specifically, both driving modes show a similar bending trend at the beginning of L from 48 mm to 208 mm. When the length increases over 208 mm, the bending angle of the expansion mode starts to drop, but the bending angle of the shrinkage mode keeps rising. In addition, when L comes to 288 mm, the bending angle of shrinkage mode also starts to drop, and the bending angle curve of expansion and shrinkage mode shows a similar trend again after L reaches 325 mm. Therefore, although the bending angles of shrinkage and expansion mode differ when L is over 248 mm, both the expansion mode and shrinkage mode of the actuator can achieve the desired design.

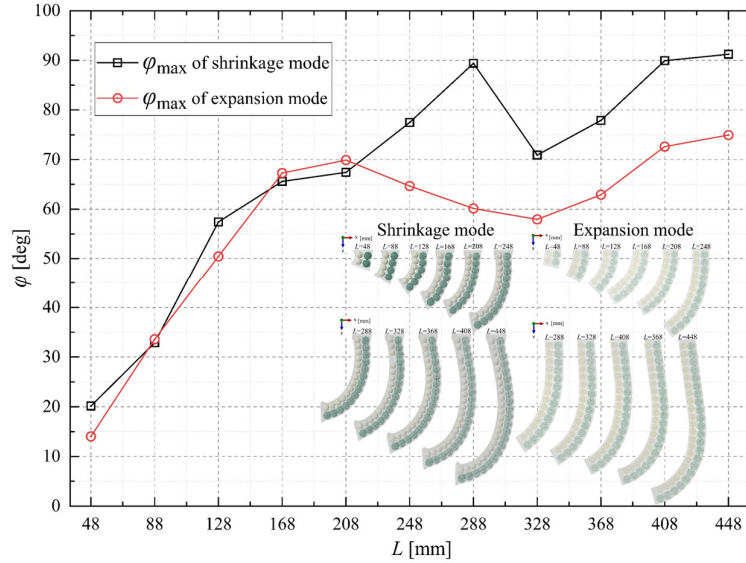


Figure 4.18. Comparison of different driving modes of different actuator length L

4.4.1.2 Effect of the particle diameter ratio

In this section, the effects of the diameter ratios of particles in the two chambers on the bending angle and deflection are analyzed. As shown in Figure 4.19, In general, the final bending state of the membrane shows a significant difference of β_{ls} from 1 to 1.33, while the final bending presents an imperceptible difference of β_{ls} from 1.33 to 2. Specifically, as shown in Figure 4.20, the difference in bending angle φ is up to 50 degrees of β_{ls} from 1.1 to 1.33 but only 10 degrees of β_{ls} from 1.33 to 2. As for the deflection change, the maximum deflection δ_{x_max} and δ_{z_max} climb gradually of β_{ls} from 1.1 to 1.33 and remain between 55 mm and 65 mm of β_{ls} from 1.1 to 1.33.

Generally, the membrane shrinkage induces the volume difference between two chambers, resulting in the bending. Specifically, when β_{ls} is at a relatively low level, both large or small particles group will reach the tight packing state before the chamber gets into the shrinking limit. At this time, the volume difference is mainly between the large particle group and the tiny particles group. Thus, the bending angle and deflections are variable as the β_{ls} change. Additionally, when the value of β_{ls} gets larger, the volume of the particles group in the left can not form the tight packing state before the chamber reaches the shrinking limit, which means the particles in the left chamber will not take the main effects anymore. Thus, the bending state is stable when β_{ls} is up to a high level from 1.33 to 2.

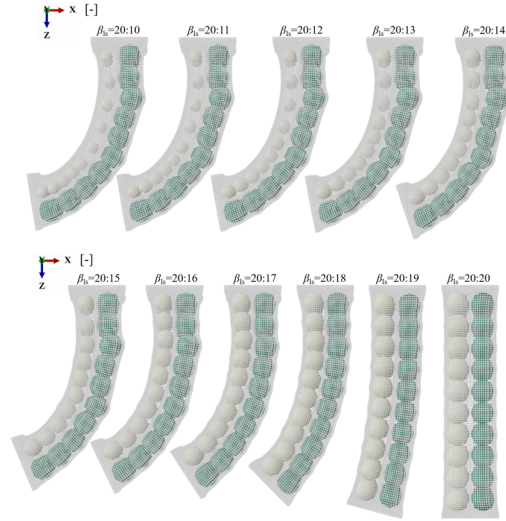


Figure 4.19. The actuator bending performance of different β_{1s}

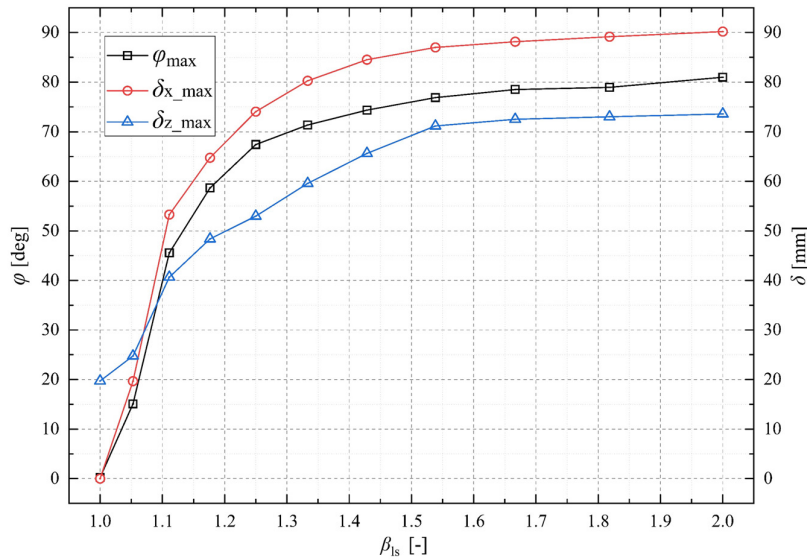


Figure 4.20. The actuator bending angle and deflection curves of different β_{1s}

4.4.1.3 Effect of the actuator length

In this section, the effect of the actuator length on the bending angle and deflection is analyzed. The variation of the whole actuator length depends on the chamber length and particle number, thus the particle number also changes in exploring the effect of actuator length. The results of the final bending state of different actuator lengths from 28 mm to 448 mm are shown in Figure 4.21. First, the final bending angle increases gradually of L from 28 mm to 288 mm, while the final bending angle first drops when L comes to 328 mm and then goes up until L comes to 448 mm. Then, when L is over 288mm, the overall structure exhibits a curvature near the fixed end rather than only at the free end. This phenomenon can be explained by transitioning from a bending state to a curling state. First, when the actuator length L is at a low level, the internal force produced by the interactions between particles and membrane only takes effect on the

structure in the horizontal direction, thus the bending state forms. However, when the actuator length L comes to a high level, the internal force produced by the interactions between particles begins to take effect in the vertical direction, which causes the curling state.

Additionally, to observe the deformation trend specifically, the bending angle φ and the deflection δ at the free end are illustrated in Figure 4.22. A similar changing trend of bending angle φ shows up, the δ_{x_max} and δ_{z_max} drop of L from 288 mm to 328 mm. When the actuator length is from 328 mm to 448 mm, δ_{x_max} keeps decreasing while δ_{z_max} climbs again. This indicates that, first when curvature changes from a bending state to a curling state, the effect of particles interacting on the membrane gradually weakens, thereby reducing the horizontal deflections of the actuator. Then, as for δ_{z_max} , it decreases transiently in the transition state, and then owing to the effects of the shrinking membrane and interactions of particles to particles and particles to the membrane, δ_{z_max} shows a rising trend of the curling state of actuator length from 288 mm to 328 mm.

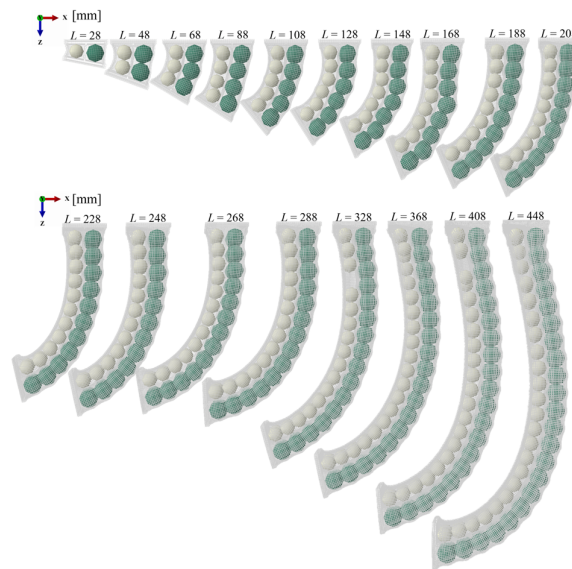


Figure 4.21. The final bending state of the actuator of different L

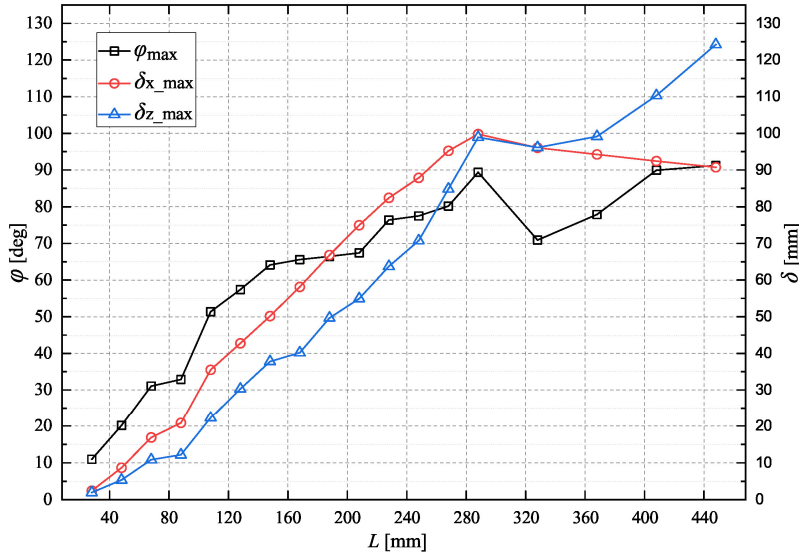


Figure 4.22. The bending angle and the deflection curve of the actuator of different L

4.4.1.4 Effect of the membrane material property

In this section, the effects of the membrane material property on the bending angles and deflections are analyzed. The bending performance is shown in Figure 4.23. Generally, the bending angle increases gradually with the E_m increasing until around 650 MPa and then drops off when E_m reaches 60000 MPa. In addition, the arrangement of the particles in each chamber is more ordered as the membrane is stiffer. The phenomenon of the bending angle increasing can be explained as the changes in the relationship between stress and strain. When the membrane material is of a low-level elastic modulus, the membrane is easy to deform with lower stress, and the structure is too soft to support a bending curvature, thus, little bending happens. Also, when the membrane material becomes much stiffer, the particles become softer compared to the membrane, thus, there are fewer interaction effects caused by particles on the membrane to achieve a bending behavior. Therefore, the bending angle no longer increases but drops down.

Furthermore, the bending angle and the deflection at the free end of different membrane materials are illustrated in Figure 4.24. The bending angle increases gradually as the E_m increases from 50 MPa to 600 MPa and then drops down as the E_m changes from 600 MPa to 60000 MPa. The deflection change has a similar trend to the bending angle variation. In addition, it can be seen that $\delta_{z_{\max}}$ remains around 30 mm rather than keeps going down when the elastic modulus of the membrane changes from 8000 MPa to 6000 MPa, which also indicates that the interactions between membrane and particles no longer contribute to bending when the membrane is stiff enough, thus the overall structure becomes a hard shell with a fixed shrinking coefficient.

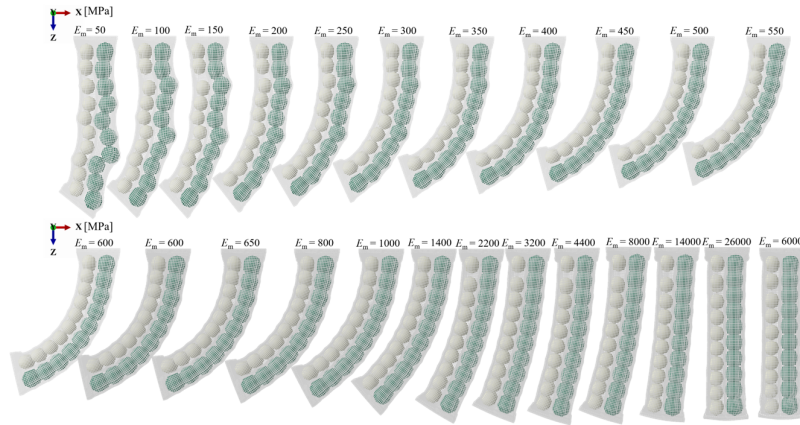


Figure 4.23. The final bending state of the actuator for different E_m

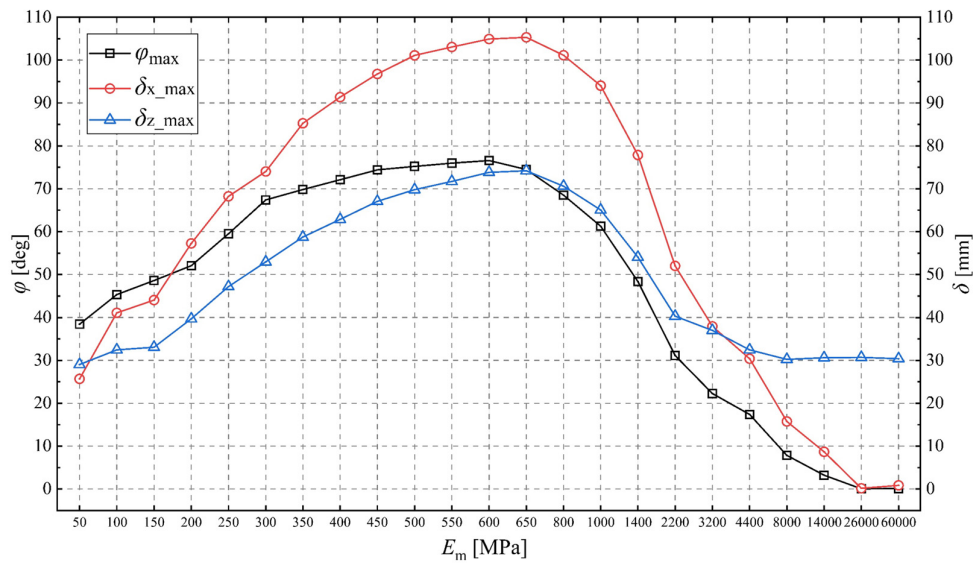


Figure 4.24. The bending angle (include symbol) and the deflection (include symbol) of the actuator as a function of E_m

4.4.2 Sensitive analysis of smart hydrogel particle-based building block

To substantiate the numerical model of the swelling process, a comparative analysis is conducted between the simulation results of the swelling ratio (λ) concerning the PNIPAM hydrogel and the corresponding experimental data [276, 277]. The single PNIPAM hydrogel sphere with different Nv is modeled to conduct the simulation and the temperature across the range from 307 K to 290 K. As shown in Figure 4.25, the numerical results and experimental data are in good alignment, with a maximum deviation of 0.5 in λ .

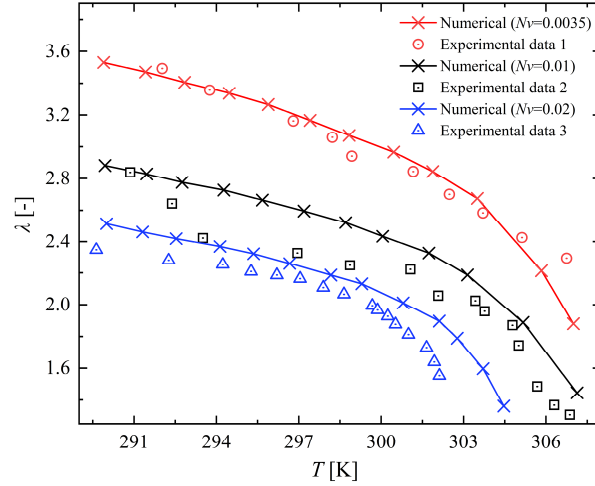


Figure 4.25. Comparison of the hydrogel swelling ratio [276, 277]

Furthermore, to validate the bending performance of the proposed actuator gripper, a comparative analysis of the bending performances between the numerical model and experiments has been conducted. In the conducted experiments, chamber and hydrogel balls are produced through mold casting, with 3D-printed molds using Polylactic acid (PLA) filament. The chamber membrane is constructed from Ecoflex-30 silicone, and the balls are made of PNIPAM based hydrogels. Furthermore, in the experiments, the full bending and recovery process took 9 hours, including around 8 hours of the bending and 30 minutes of the recovery cycle. The bending angle is measured by the displacements of the free end of the gripper. In order to align with experimental conditions, a simulation is performed with $N\nu$ set at 0.0035. Furthermore, bending displacement occurred in both the x and z directions, with the gravitational effects in the y direction ignored. The grid lines is used to measure the displacement in the x direction (δ_x) and the displacement in the z direction (δ_z), and the bending angle φ is calculated as,

$$\tan \varphi = \frac{\delta_x}{\delta_z} \quad (4.37)$$

Figure 4.26 illustrates the comparison with error bars indicating measurement discrepancies in three experimental trials, and the maximum error attains a magnitude of 8%. Generally, both the experiment and numerical case shows that the φ increases as the increasing of the λ . Furthermore, simulation results closely match experimental bending angle trends, validating the proposed design. However, it's worth noting that experimental values are slightly lower than simulated results, with a maximum variance of 7.2° . This discrepancy can be attributed to two primary factors. Firstly, in the fabrication process, mold casting is employed for both the silicone cavity and cover. The closure of the cavity requires additional silicone for adhesion, expanding the membrane thickness locally and causing a reduced bending angle. Secondly, simulation boundary conditions are ideal, whereas practical experimentation introduces external factors, such as non-uniform internal temperature distribution within the structure and the release of water during the bending (hydrogel expansion) process, both adversely impacting bending performance.

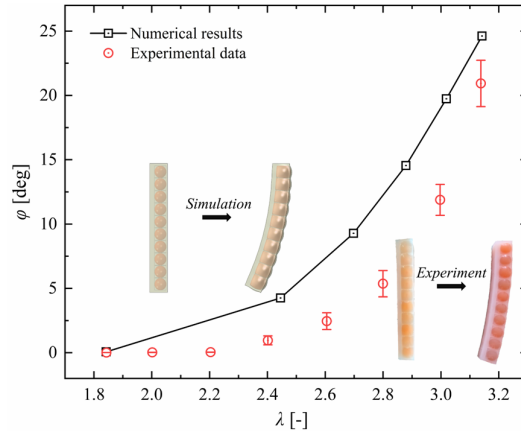


Figure 4.26. Comparison of the simulated and experimental results of the bending angle (φ) of the actuator for different swelling ratios (λ)

4.4.2.1 Sensitivity Analysis of different factors

Various key factors, such as the number of hydrogel spheres, structure configurations, and membrane materials, are chosen to study their impact on bending performance. Specifically, each hydrogel sphere occupies one individual unit in one layer, thus the hydrogel sphere layers can represent the number of hydrogel spheres. Hydrogel sphere layers represent the sphere count, ranging from 10 to 50 layers. Different structural configurations (straight, wavy, prismatic, and clubbed) are explored, and materials details are shown in Table 4.2. Besides, $N\nu$ sets as 0.01 in the simulations. Furthermore, a uniform temperature of 291 K is selected across all simulation scenarios.

The result of the bending angle of different hydrogel sphere layers is shown in Figure 4.27 (a). Generally, more hydrogel layers result in a higher bending angle, indicating a consistent interaction force between the membrane and swelling hydrogel. Specifically, the φ is 24.61° for the configuration with 10 hydrogel layers, while the φ is 127.12° for the arrangement involving 50 hydrogel layers. The correlation coefficient concerning the relationship between the bending angle and the hydrogel layers measures 2.56° .

Figure 4.27(b) illustrates how bending angles change with varying structural configurations due to swelling ratio. Generally, as the swelling ratio increases, the bending angles of different structures also increase, and this increase occurs gradually. This overall pattern suggests a consistent trend between bending angles and swelling ratio across various structural configurations.

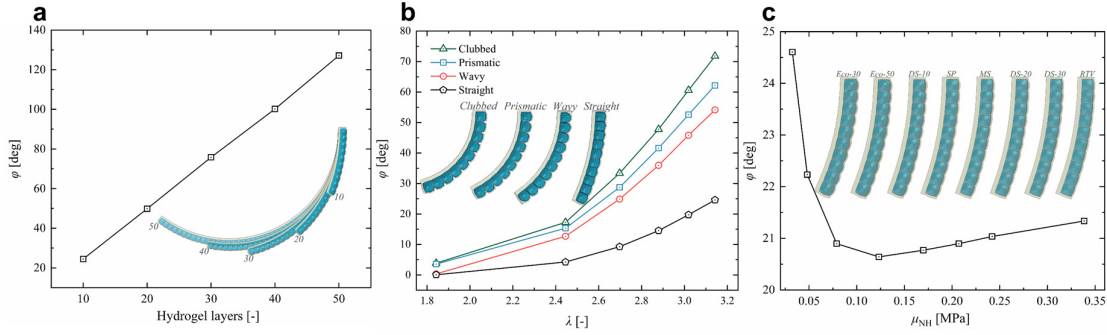


Figure 4.27. Bending performance of different influential parameters (a) The bending angle (φ) for different hydrogel sphere layers with the straight configuration (b) The bending angle (φ) of different membrane structures as a function of the swelling ratio (λ) (c) The bending angle (φ) as a result of different Neo-Hookean coefficients (μ_{NH})

Specifically, the clubbed configuration attains a maximum φ of 71.8°, the prismatic configuration achieves a maximum φ of 62.17°, and the wavy configuration demonstrates a maximum φ 54.14°, all under the condition of λ being 3.15. These values substantially surpass the maximum φ achievable in the straight configuration. Figure 4.27(c) illustrates how the Neo-Hookean coefficient μ_{NH} affects the bending angle. Generally, as μ_{NH} increases, the bending angle drops suddenly and then rises slowly. Generally, an increase in μ_{NH} initially causes a sharp decrease in the bending angle from 0.032 to 0.123, as the membrane becomes stiffer, limiting the elongation by the swelling hydrogel. This reduced elongation weakens the external structure's shape, resulting in a lower bending angle. However, as μ_{NH} goes from 0.123 to 0.339, the bending angle gradually increases due to amplified μ_{NH} , which shifts the balance of strain-limit layer constriction, causing a higher bending angle. Additionally, when transitioning from Ecoflex-30 (Eco-30) to RTV 615 (RTV), the left side experiences reduced curvature. Specifically, the φ decreases from 24.61° to 20.64° of μ_{NH} across the range from 0.032 to 0.123, while the φ only increases from 20.64° to 21.33° of μ_{NH} across the range from 0.123 to 0.339.

4.4.2.2 Bending stiffness evaluation and variation

The bending stiffness in this study refers to the capacity of the entire structure to resist the external force while maintaining its form without undergoing deformation. The bending stiffness can be expressed as follows [236],

$$S_a = \frac{NL \sin \beta}{\theta} \quad (4.38)$$

where S_a represents the bending stiffness. As shown in Figure 4.28, N represents the external force, L is the distance from the fixed top layer to the free layer. Thus, $NL \sin \beta$ represents the external moment about the fixed end. Here, θ denotes the rotational angle causing by the external moment.

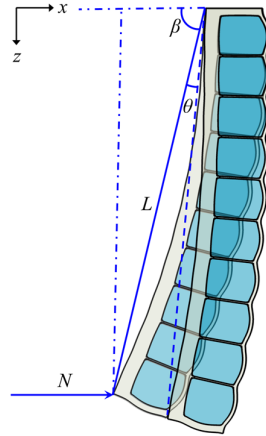


Figure 4.28. Illustration of the calculation of the bending stiffness

The variation in bending stiffness across different structural configurations and membrane materials being altered by the bending angle, are illustrated in Figure 4.29. Figure 4.29 (a) displays the S_a of various structural configurations. Overall, the results reveal that increasing the bending angle leads to higher bending stiffness, with the straight configuration showing the most pronounced change. Additionally, structural design influences bending stiffness, with the straight configuration having the highest, followed by the wavy, prismatic, and finally, the clubbed configuration with the lowest bending stiffness. Specifically, the straight configuration has about twice the bending stiffness compared to the others. In contrast, the wavy, prismatic, and clubbed configurations show a consistent increase in bending stiffness, suggesting that introducing gaps into the structural design improves bending performance, though with a trade-off in stiffness.

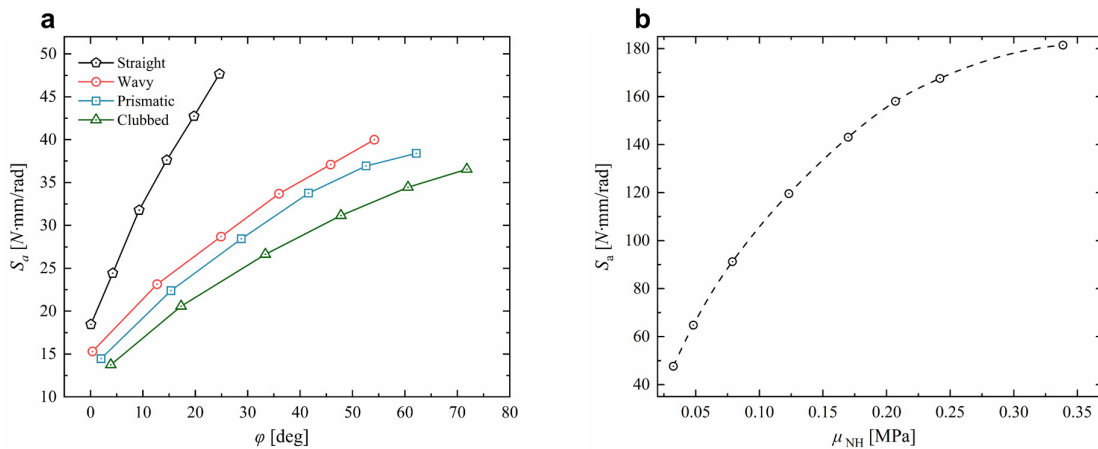


Figure 4.29. The variation in bending stiffness (a) *The bending stiffness (S_a) of different structural configurations.* (b) *The bending stiffness (S_a) of different membrane materials*

The membrane materials chosen from Table 4.2 determine bending stiffness, as shown in Figure 4.29(b). Bending stiffness generally increases with higher μ_{NH} values, exhibiting a nonlinear relationship. We describe this nonlinear correlation using a polynomial fitting approach, resulting in equation (4.40),

$$S(\mu_{NH}) = 2332\mu_{NH}^3 - 2818\mu_{NH}^2 + 1181\mu_{NH} \quad (4.40)$$

The coefficient of determination (R^2) [278], denoted as 0.99973, indicates a substantial level of consistency between the regression forecast and the actual value. This polynomial model can evaluate bending stiffness across various membrane materials.

Specifically, S_a increases sharply of the μ_{NH} across the range from 0.032 to 0.171, while the rising trend of S_a gradually stabilize of the μ_{NH} across the range from 0.171 to 0.339, indicating that the bending stiffness is sensitive to changes of more flexible materials. Furthermore, when contrasting the variation in bending angles resulting from alterations in μ_{NH} as depicted in Figure 4.27(c), the divergence in bending stiffness across various μ_{NH} values is notably more pronounced.

4.4.2.3 Stiffness enhanced method

While the hydrogel-based smart actuator gripper achieves significant flexibility and a wide range of motion, it faces a limitation in bending stiffness. Increasing load-bearing capacity for diverse grasping tasks involves introducing a low melting point alloy (LMPA) mechanism to enhance bending stiffness [279, 280]. LMPA exhibits a liquid state above its transition temperature and solidifies below this threshold. In this study, gallium-based LMPA with a transition temperature of 303 K was integrated into the soft actuator as variable stiffness strips to achieve tunable stiffness variation.

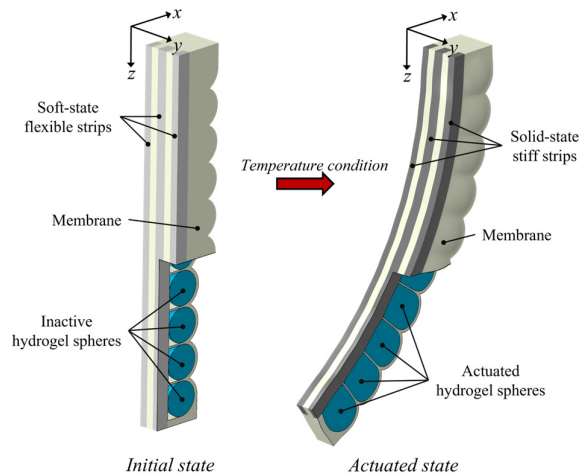


Figure 4.30. Illustration of the stiffness enhanced method

As shown in Figure 4.30, three variable stiffness strips are inserted in the strain-limit layer of the size of 8 mm in x direction, 6 mm in y direction, and 213 mm in z direction. In the modeling process, the principle of LMPA was applied and several assumptions were employed to represent the LMPA behavior in the simulation. The liquid state of LMPA was represented by a low elastic modulus of 0.08 MPa to denote deformability. Furthermore, the variable stiffness strips undergo plastic deformation during the actuator's bending. As the actuator bends to its extreme position, adopting a temperature-based condition increases the strips' elastic modulus to 9800 MPa, demonstrating the solid state, which results in the entire actuator maintaining a fixed shape with significantly enhanced bending stiffness. In addition, the simulation results lay

foundation for LMPA development with parameters that can be employed in an actuator configuration for tailoring stiffness. This will increase the load bearing capacity.

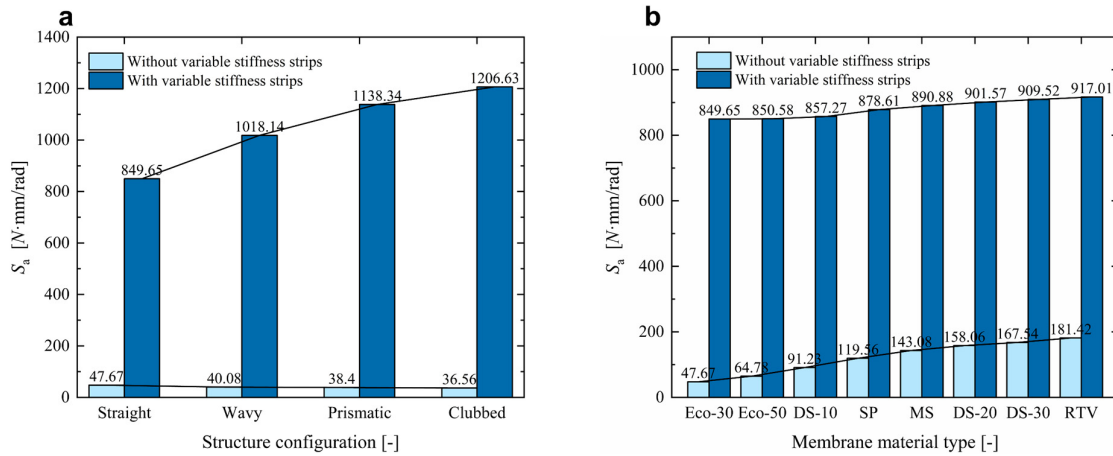


Figure 4.31. The results of the enhanced bending stiffness (a) *The bending stiffness (S_a) of different structural configurations with and without stiffness strips* (b) *The bending stiffness (S_a) of different membrane materials with and without stiffness strips*

Figure 4.31 depicts increased bending stiffness with variable stiffness strips in various structures and membrane materials. In Figure 4.31(a), compared to the original design, the use of these strips boosts bending stiffness by up to thirty times, demonstrating their effectiveness. Notably, the bending stiffness with variable stiffness strips rises from a straight to a clubbed configuration, contrary to the original design. Illustrated in Figure 4.31(b), when comparing with the original designs without variable stiffness strips, the incorporation of variable stiffness strips yields a maximum twenty-fold improvements in bending stiffness across various membrane materials.

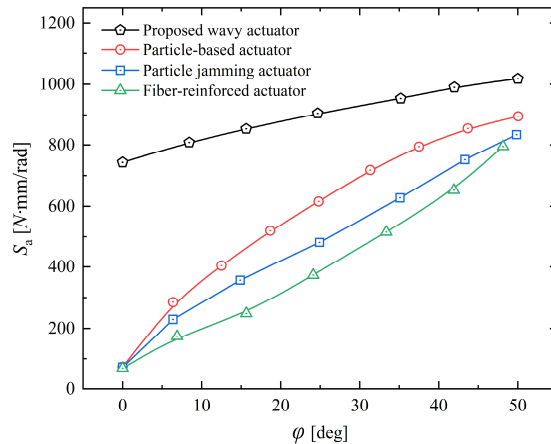


Figure 4.32. The bending stiffness (S_a) comparison of different actuators [275, 281, 282]

To further evaluate the effects of the stiffness enhanced method, a comprehensive comparison to other variable stiffness actuators is introduced, including proposed wavy actuator, particle-based actuator [281], particle jamming actuator [275], and fiber-reinforced actuator [282]. Figure 4.32 displays the bending stiffness of different actuators at various bending angles. The

proposed actuator significantly outperforms others, with 1.15 times greater stiffness than the particle-based actuator, 1.22 times greater than the particle jamming actuator, and 1.28 times greater than the fiber-reinforced actuator when fully actuated.

4.5 Conclusion

In this chapter, the conceptual design of particle-based bending building blocks are proposed and evaluated, enabling large deformation and stiffness variation.

To achieve large deformation and stiffness variation, this chapter first proposed a novel conceptual design of a particle-based soft building block through model-based design framework. First, the rigid-particle based actuator is proposed based on the particle jamming effect, which is characterized by a dual-deformable chamber structure filled with tailored particles. Then, a novel building block was proposed to explore the potential of smart hydrogel as actuating method on the soft grippers. The proposed soft gripper is characterized by flexible structure and temperature-sensitive smart hydrogel particles.

In the design of rigid particle building block, the simulation results are in good agreement with the experimental cases, which have validated the feasibility of the simulation method. Furthermore, the specific results have shown that both the shrinkage mode and expansion mode of the actuator can achieve the bending behaviors of different particle diameter ratios from 1 to 2 and different actuator lengths from 48 mm to 448 mm. In addition, the larger bending angle and more significant deflection can be achieved by increasing the particle diameter ratio from 1 to 2, the actuator length from 28 mm to 288 mm, and the elastic modulus of the membrane from 50 MPa to 600 MPa. However, when the actuator length increases from 288 mm to 448 mm and the elastic modulus of the membrane from 600 MPa to 60000 MPa, the performance of the soft actuator will deteriorate.

In the design of smart hydrogel-based building block, the simulation results also have shown good consistency with experimental data in displacements and bending angles. As for the influential parameters, to increase the bending performance of the soft gripper, either the particle layers must be increased, the structure material must be more flexible or the structure design of the strain layer must be considered to have specific shaped gaps. In addition, bending stiffness grows as the angle increases, but structures with gaps reduce stiffness, while rigidly covered membranes enhance it. Implementing variable stiffness strips significantly boosts bending stiffness, achieving a thirty-fold increase at most, demonstrating a relative improvement compared to other enhanced actuators.

The proposed conceptual designs can facilitate the development and modeling of multiple smart materials-based building block incorporating smart materials to achieve multifunctional capabilities. Thus, in the next chapter, these building blocks will be developed by integrating multiple smart materials, which will enable stiffness variation and self-actuation, providing the foundation for mechanical intelligence.

5 Model-based design of a mechanically intelligent morphing building block by multiple materials*

In the previous chapters, within the model-based design framework, the use of a particle-based unit cell demonstrates promising potential for integrating smart material into building blocks for morphing structure design that enables stiffness variation. In order to embed the morphing structure into soft robotics with mechanical intelligence, achieving both stiffness variation and self-actuation are required. To meet these requirements, integrating multiple smart materials into a single building block is a feasible solution. Building on the conceptual designs introduced in Chapter 4, this chapter develops building blocks using multiple smart materials for mechanically intelligent morphing structures. Section 5.2 proposes the simplified modeling methods to describe different nonlinear behaviors of multiple smart materials in one structure. In Section 5.3, the shape morphing building block, based on a hydrogel-SMP framework, is introduced along with the self-actuation process. Assembling these building block, Section 5.4 proposes different morphing structures enabling diverse morphing configurations and stiffness variation. Finally, Section 5.5 presents the main conclusions.

* This chapter is based on Q. Chen, D. Schott, and J. Jovanova, “Model-based design of a mechanically intelligent shape-morphing structure,” *Scientific Reports*, vol. 14, no. 1, pp. 26148, 2024. <https://doi.org/10.1038/s41598-024-74379-4>

5.1 Introduction

Among the smart materials utilized in soft robotics, smart hydrogels are widely used owing to the improved mechanical flexibility and suitability for a range of material substrates [283]. Owing to their polymer structure, being cross-linked either physically or chemically, hydrogels show as elastic solids characterized by deformability and softness [284]. Smart hydrogel have the ability to swell or shrink in response to external stimuli, primarily including factors such as temperature, pH, light, or chemical triggers [285]. Within the special attributes, smart hydrogels can be easily integrated into soft robotics systems to serve as actuators. Zheng et al. demonstrated a soft gripper comprising a bilayer structure, capable of functioning even in the air conditions, achieved by layering two distinct types of temperature-responsive hydrogels [256]. Duan et al. developed a soft actuator that produces significant deformations and demonstrates bidirectional bending by stacking anionic and cationic pH-responsive hydrogels [286]. Takashima et al. developed an expansion-contraction artificial muscle utilizing photo-responsive hydrogel [287]. Palleau et al. created a reversible hydrogel actuator that can grasp small objects in ethanol (EtOH) and release them in water [288]. However, despite their flexibility, the low modulus and mechanical strength of the hydrogels limit their application in complex environments and stiffness variation.

Furthermore, shape memory polymers (SMPs) are another smart materials widely employed as actuators, which are crucial components in soft robotics devices for enhancing stiffness [289, 290]. Their functionality is based on the principle of phase transition, which changes the relative mechanical properties and achieve self-healing or shape memory effect [291]. SMPs respond to various stimuli, with temperature being the most common. Specifically, when exposed to temperatures above their transition point, SMPs change from a glassy phase to a rubbery phase. In the rubbery phase, SMPs exhibit a low elastic modulus, supporting them highly deformable. When SMPs cool and return to the glassy phase, they retain the deformed shape, recovering a high elastic modulus and thus achieving stiffness variation [128]. Gandhi et al. introduced a multilayer configuration utilizing SMP, featuring adaptable stiffness by changing the state of the polymer [292]. Wang et al. proposed a bioinspired soft robotic finger based on the SMP, featuring adaptable bending capabilities by controlled adjustments in stiffness [293]. Despite exhibiting unique function and shape control, most SMPs only have one-way shape memory effect and lack the ability to deform in response to stimuli triggers. Thus, SMP-based designs need external loading to achieve desired deformations.

This chapter presents the design of a mechanically intelligent shape-morphing structure incorporating smart materials to achieve tailored deformation and stiffness variation. The contributions of this work include several points. First, the novel intelligent structure unit, based on the combination of pH-sensitive hydrogel and SMP, is designed to achieve volume and stiffness variation. Then, the building block of different shape-morphing structures based on the smart units are proposed for applications in soft robotics. Furthermore, To effectively capture large deformations while also reducing computational costs, we used a novel approach. Here the constitutive model, combined with a simplified viscoelastic model, is used in the FEM solver to describe the nonlinear behaviors of both pH-sensitive hydrogel and SMP within the same structure. The design strategy is illustrated in Figure 4.1. Initially, the intelligent structural

unit is created using multiple smart materials. Subsequently, the numerical approach is applied to investigate the different deformation behaviors of building blocks, which are composed of intelligent units. Based on these building blocks, morphing structures are then developed through structural design to achieve specific functionalities. Moreover, these morphing structures have potential applications in soft robotics, such as in grasping tasks during undersea cave exploration, where they could be used for ore collection.

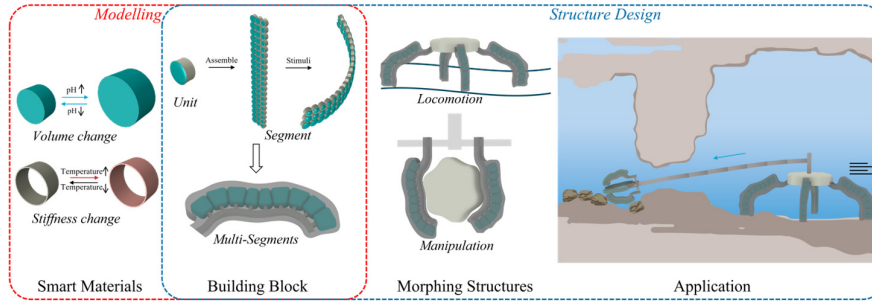


Figure 5.1. The design framework by building blocks

5.2 Methodology

The modeling of smart materials holds significance in design processes. This study employs Finite Element Method (FEM) to describe the nonlinear characteristics of the pH-sensitive hydrogel and thermal response Shape Memory Polymer (SMP). pH-sensitive hydrogel and SMP are utilized as the smart materials integrated into the actuator. The pH-sensitive hydrogel is selected as the smart actuating material that can be used underwater due to their low cost, and high adaptability and sensitivity. In addition, the elevated pH levels in seawater, as opposed to air, create optimal conditions for activating pH-sensitive hydrogels. This property makes pH-sensitive hydrogels ideal materials for use in ocean engineering applications. Similarly, SMP is chosen based on the simplicity of achieving triggering conditions. The swelling and shrinking of the hydrogel induced to actuate the structure, while the shape memory effect of SMP applied as the stiffness enhanced method.

5.2.1 The pH-sensitive hydrogel modeling

Hydrogel exhibits hyperelastic properties and can be described by free energy theory to understand diffusion and deformation mechanisms [294]. The free energy density of pH-sensitive hydrogels encompasses various contributing factors and expressed as,

$$W(\mathbf{F}, C_{H^+}, C_+, C_-) = W_{net}(\mathbf{F}) + W_{sol}(\mathbf{F}) + W_{ion}(\mathbf{F}, C_{H^+}, C_+, C_-) + W_{dis}(\mathbf{F}, C_{H^+}, C_+, C_-) \quad (5.1)$$

where W is the free energy density, \mathbf{F} denotes the deformation gradient tensor, and C_{H^+} , C_+ , C_- are nominal concentrations of hydrogen ions, mobile cations, anions, respectively. $W_{net}(\mathbf{F})$ is the elastic energy from polymer network stretching, that can be expressed by Neo-Hookean model as,

$$W_{net}(\mathbf{F}) = \frac{NkT}{2} [F_{ik}F_{ik} - 3 - 2 \log(\det\mathbf{F})] \quad (5.2)$$

where N is the polymer chains number divided by the volume of the dry network, F_{ik} is the deformation gradient of the network, and the swelling volume is, $\det\mathbf{F} = 1 + v_s C_s$, where C_s and v_s are the concentration of solvent and single molecule volume, respectively. Moreover, k is the Boltzmann constant and T is the absolute temperature. $W_{sol}(\mathbf{F})$ is from polymer-solvent mixing and described by Flory–Huggins model [295, 296],

$$W_{sol}(\mathbf{F}) = \frac{kT}{v_s} \left[(\det\mathbf{F} - 1) \log \left(1 - \frac{1}{\det\mathbf{F}} \right) - \frac{\chi}{\det\mathbf{F}} \right], \quad (5.3)$$

where χ is the Flory–Huggins interaction coefficient, expressing the enthalpy of the mixing polymer. $W_{ion}(\mathbf{F}, C_{H^+}, C_+, C_-)$ represents energy from ion-solvent, and mobile ions, with their low concentration, primarily affect free energy through mixing entropy,

$$W_{ion}(\mathbf{F}, C_{H^+}, C_+, C_-) = kT \left[C_{H^+} \left(\log \frac{C_{H^+}}{C_{H^+}^{ref} \det\mathbf{F}} - 1 \right) + C_+ \left(\log \frac{C_+}{C_+^{ref} \det\mathbf{F}} - 1 \right) + C_- \left(\log \frac{C_-}{C_-^{ref} \det\mathbf{F}} - 1 \right) \right] \quad (5.4)$$

and $W_{dis}(\mathbf{F}, C_{H^+}, C_+, C_-)$ arises from acidic group dissociation in polymer chains,

$$W_{dis}(\mathbf{F}, C_{H^+}, C_+, C_-) = kT \left[C_{A^-} \log \left(\frac{C_{A^-}}{C_{A^-} + C_{AH}} \right) + C_{AH} \log \left(\frac{C_{AH}}{C_{A^-} + C_{AH}} \right) \right] + \gamma C_{A^-}, \quad (5.5)$$

where γ denotes the enthalpy increase, while C_{A^-} and C_{AH} represent fixed charge and associated acidic group concentration. The relationship between these concentrations requires, $C_{A^-} = C_{H^+} + C_+ - C_-$, and $C_{AH} = f/v_s - (C_{H^+} + C_+ - C_-)$, in which f is the number of acidic groups on a polymer chain. The thermodynamic state of the system is entirely determined by the free energy, as described by Equation (5.1). Once the explicit expression of the system's free energy is obtained, the elastic stress of the hydrogel can be derived as,

$$\sigma_{ij} = \frac{F_{jK}}{\det\mathbf{F}} \frac{\partial (W_{net} + W_{sol} + W_{dis})}{\partial F_{iK}} - \frac{\mu_s}{v_s} \delta_{ij}, \quad (5.6)$$

where μ_s represents the chemical potential. Using the osmotic pressure to express μ_s , the stress tensor can be expressed as,

$$\sigma_{ij} = \frac{NkT}{\det\mathbf{F}} (F_{ik}F_{jk} - \delta_{ij}) - (\Pi_{sol} + \Pi_{ion})\delta_{ij} \quad (5.7)$$

The osmotic pressures from polymer-solvent and ion-solvent mixtures, denoted Π_{sol} , and Π_{ion} , respectively, are defined as,

$$\Pi_{sol} = -\frac{kT}{v_s} \left[\log \left(1 - \frac{1}{\det\mathbf{F}} \right) + \frac{1}{\det\mathbf{F}} + \frac{\chi}{(\det\mathbf{F})^2} \right], \quad (5.8)$$

$$\Pi_{ion} = kT(C_{H^+} + c_+ + c_- - \bar{c}_{H^+} - \bar{c}_+ - \bar{c}_-), \quad (5.9)$$

where $c_i (i = +, -, H^+)$ and $\bar{c}_i (i = +, -, H^+)$ describe the true concentrations of cations, anions and hydrogen ions inside and outside, respectively. In addition, the true concentrations and nominal concentrations are related as, $C_i = c_i \det \mathbf{F}$. The \bar{c}_{H^+} also relates to the pH of outside solution and is expressed as,

$$\bar{c}_{H^+} = N_A 10^{-\text{pH}} \quad (5.10)$$

where N_A is the Avogadro number, $N_A = 6.023 \times 10^{23}$. In addition, the specific conditions are required for ionic equilibrium as [219],

$$\frac{c_+}{\bar{c}_+} = \frac{\bar{c}_-}{c_-} = \frac{c_{H^+}}{\bar{c}_{H^+}} \quad (5.11)$$

By applying the Donnan equations and considering the principle of electroneutrality within the hydrogel, the following equation for acid dissociation is derived,

$$\frac{c_{H^+}(c_{H^+} + c_+ + c_-)}{\left(\frac{f}{v_s}\right) (\det \mathbf{F})^{-1} - (c_{H^+} + c_+ + c_-)} = N_A K_a \quad (5.12)$$

where K_a is constant of acidic dissociation. Equation (5.12) is expressed based on c_{H^+} that can be solved FEM solver. In the numerical simulation process, the Abaqus finite element solver is employed for the pH-sensitive hydrogel. A user-defined subroutine is utilized to describe the hyperelastic material based on the free energy function. It is assumed in this model that the volume per monomer is equivalent to the volume per solvent molecule. Additionally, the composition of the external solution is defined solely by \bar{c}_+ and \bar{c}_{H^+} . The electroneutrality in the outside solution needs to satisfy $\bar{c}_- = \bar{c}_+ + \bar{c}_{H^+}$, where \bar{c}_{H^+} is considered as a variable calculated from the input pH value.

5.2.2 SMP modeling

The shape memory effect relating to the stiffness variation shows significant viscoelasticity, spanning temperatures both above and below the glass transition temperature [241, 242]. In our study, we employed the superimposed generalized Maxwell model and Williams-Landel-Ferry (WLF) equation within Abaqus finite element solver to elucidate the mechanical behavior of SMP. The utilized constitutive equations for the multi-branch viscos-elasticity are as follows [243],

$$\sigma(t) = \varepsilon_0 E_n + \varepsilon_0 \sum_{i=1}^{n-1} E_i e^{\frac{-t}{\tau_i}} \quad (5.13)$$

where $\sigma(t)$ represents stress at time t , ε_0 is the strain at the initial time, E_n denotes the instantaneous modulus, E_i and τ_i represent the elastic modulus and relaxation time of the Maxwell element i , respectively.

The relation of relaxation modulus E in the generalized Maxwell equation with time t is expressed as follows,

$$E(t) = E_n + \sum_{i=1}^{n-1} E_i e^{-\frac{t}{\tau_i}} \quad (5.14)$$

and satisfies the limit condition, $\lim_{t \rightarrow \infty} E(t) = E_n$. Conducting relaxation experiments at various temperatures and applying the time–temperature equivalence principle is essential. This allows the conversion of the relaxation response curve of SMP across different temperatures into a comprehensive relaxation response curve at a specific temperature. According to the WLF equation [243], the connection between the relaxation time at the present temperature T and the relaxation time at the reference temperature of T_r can be written as,

$$\lg \alpha_T = \lg \frac{\tau}{\tau_r} = \frac{-C_1(T - T_r)}{C_2 + (T - T_r)} \quad (5.15)$$

where α_T represents shift factor, C_1 and C_2 are material constant. And it is assumed that here the glass transition temperature (T_g) is same as T_r .

5.2.3 Simulation setup

For the specific materials, poly(acrylic acid) (PAA) hydrogel, a widely recognized pH-sensitive hydrogel, is used as a reference in this study, with the polymer specified by several parameters. In particular, the representative value of volume of per water molecule is $v_s = 10^{-28} m^3$, and the number of monomers per chain is $1/Nv_s$. The chemical potential, normalized by kT , is $4 \times 10^{-21} J$. For the PAA hydrogel, which exhibits a preference for large swelling ratios, the parameters Nv_s , f , and χ are set to 0.001, 0.03, and 0.1, respectively. Additionally, the concentrations of anions \bar{c}_- is 0.005 M and dissociation constant K_a is $10^{-4.3}$, both of which are typical for carboxylic acids [219]. The pH is set as the input parameter, which changes from 2 to 8. Furthermore, polylactic acid (PLA), recognized for its biodegradability, non-toxicity, and renewability, is selected as SMP for modeling [297]. The parameters related to the viscoelastic and thermal properties are set as, $T_g = 334 K$, $C_1 = 6.14$ and $C_2 = 293 K$ [298]. The material's elastic modulus was 1000 MPa at 298 K, decreasing by 60% at the transition temperature [299]. Consequently, the temperature range from 295 K to 360 K was selected for the simulation.

For the remaining configurations, a standard 3D C3D8H mesh (8-node linear brick, hybrid with constant pressure) was selected to enhance mesh quality and convergence by addressing thin and irregular edges. Grid independence verification confirms global mesh sizes at around 0.5. Emphasis was exclusively placed on morphing structures in designing, with gravitational impact disregarded.

5.3 Mechanical intelligent structure design and validation

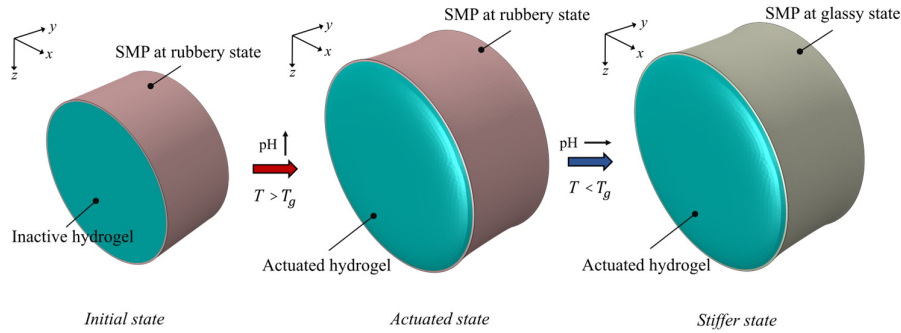


Figure 5.2. The working principle of the intelligent structure

The working principle of the proposed soft intelligent structure is illustrated in Figure 5.2. It consists of a pH-sensitive hydrogel cylinder covered by the SMP ring. In the simulation, the tied constraint interface is used between the hydrogel and SMP cover. Initially, at low pH and high temperatures above the transition point, the hydrogel is shrunken and the SMP is in a rubbery state. When the pH rises, the hydrogel expands, leading to the deformation of the SMP cover as a result of the hydrogel's increased volume. Once the hydrogel has fully expanded, reducing the temperature below the transition point enhances the stiffness of the SMP cover, locking the deformed shape. By subsequently raising the temperature and lowering the pH, the hydrogel contracts back to its original volume, allowing the SMP frame to return to its initial size. Therefore, the SMP frame is classified as a one-way shape memory material, which undergoes deformation through the activation of the hydrogel. By using this soft intelligent structure as the unit cell, various shape-morphing structures can be developed. Besides, the self-actuation strategy independent of specialized equipment will be implemented in practical applications. The developed intelligent structure will be utilized in maritime and offshore engineering, where environmental conditions will actuate the hydrogels and SMP. For instance, high pH seawater can cause the hydrogel to swell, while hot gases released from ships or undersea construction can trigger the phase transition of SMPs. Consequently, this self-actuation process conserves resources and leads to mechanically intelligent systems.

Furthermore, To validate the materials model, the simulated behavior of different pH sensitive hydrogels and typical SMPs are compared to experimental data. The comparison of pH sensitive hydrogels are shown in Figure 5.3(a). Different experimental data with different crosslink density was presented by Eichenbaum et al. [300]. In addition, Nv_s is set from 0.06 to 0.15 to match with the experimental setup. Correspondingly, the matchable materials parameters are given as, $\bar{c}_- = 0.03\text{M}$, $K_a = 10^{-4.7}$, and $f = 0.35$. The simulation results have the similar trend with the experimental data. The swelling ratio (λ) of the hydrogel rises proportionally with pH, while the increase in Nv_s leads to the reduction in λ . The comparison between the simulation results and experimental data for SMPs is shown in Figure 5.3(b). The experimental data with T_g of 343 K was obtained by Liu et al. [210], while the experimental data with T_g of 297 K was obtained Qi et al. [301]. To align the simulation with the experimental data from Liu et al., the material parameters were set to, $C_1 = 14.8$ and $C_2 = 317.4$ K. Similarly, for

comparison with Qi et al.'s experimental data, the simulation parameters were set to, $C_1 = 7$ and $C_2 = 297$ K. The simulation results exhibit acceptable agreement with experimental data, demonstrating a significant decrease in the elastic modulus of SMPs as temperature rises. Despite differences between simulations and experimental results, the qualitative behavior of the hydrogel and SMP can prove the working principle, making the simulations sufficient.

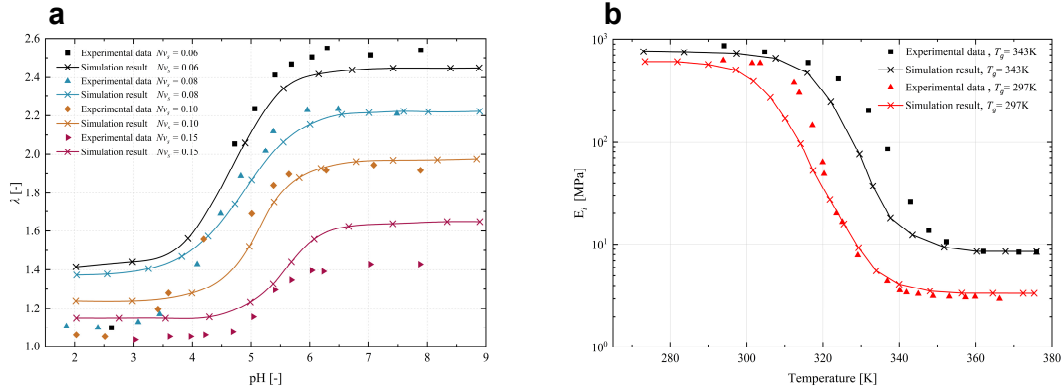


Figure 5.3. The comparison of smart materials' properties between experimental data and simulation results (a) The swelling ratio (λ) changes of hydrogel by pH (b) The elastic modulus (E_i) changes of SMPs by temperature

5.4 Results and discussion

In this section, we propose and analyze morphing structures composed of multiple intelligent units. Simulations are conducted for all cases across a pH range of 2 to 8. Initially, the temperature is set to 360K to ensure that the SMP remains in a rubbery state. After the hydrogel has fully swollen under a pH of 8, the temperature is lowered to 295K to lock the shape. The detailed parameters are provided in Table 5.1. Initially, the hydrogel is in a low-swelling state, while the temperature is maintained above the SMP transition temperature of 360 K to facilitate deformation. From steps 1 to 6, the temperature remains elevated, while the pH is gradually increased from 2 to 8, causing the hydrogel to swell. In the final step, the temperature is lowered below the SMP transition temperature to 295 K, allowing the SMP to enter a glassy state, thereby locking the morphed shape in place.

Table 5.1. The stimuli parameters during simulation steps

	Initial	Step 1	Step 2	Step 3	Step 4	Step 5	Step 6	Step 7
pH (-)	2	3	4	5	6	7	8	8
Temperature (K)	360	360	360	360	360	360	360	295

5.4.1 Case studies: bending, curling and elongation structures

Various building blocks can be developed by integrating basic intelligent units, such as bending, curling, and elongation configurations. Furthermore, to attain tailored deformation behaviors in different configurations, the primary design principle involves varying the thickness of the SMP frame, while maintaining the uniformity of other structural components. Specifically, the

thickness of SMP frame includes the thickness of ring shaped unit and the thickness of different side within each unit.

The building block of bending configuration is shown in Figure 5.4. The structural design is shown in Figure 5.4(a). Based on the intelligent unit, SMP rings of different thicknesses are used to overlap each other to form an overall structure. In the designed structure, the total layers in z direction (L_v) is used to show the length, and the total layers in x direction (L_h) is to describe the width. Besides, the diameter of each cylinder unit and height (h) of each block unit are 20 mm and 10 mm, respectively. The diameter difference ξ_t is illustrated as,

$$d_{i+1} - d_i = \xi_t \quad (5.16)$$

where d_i denotes the diameter of different hydrogel element.

The working principle of the bending structure is illustrated in Figure 5.4(b). Upon actuating the hydrogels with the rubbery state SMP, the block unit swells variably due to ξ_t . This differential swelling causes the morphing structure to bend in the x direction. The shape is then locked by lowering the temperature, transitioning the SMP to a glassy state. The bending performance is quantified by the bending angle (φ).

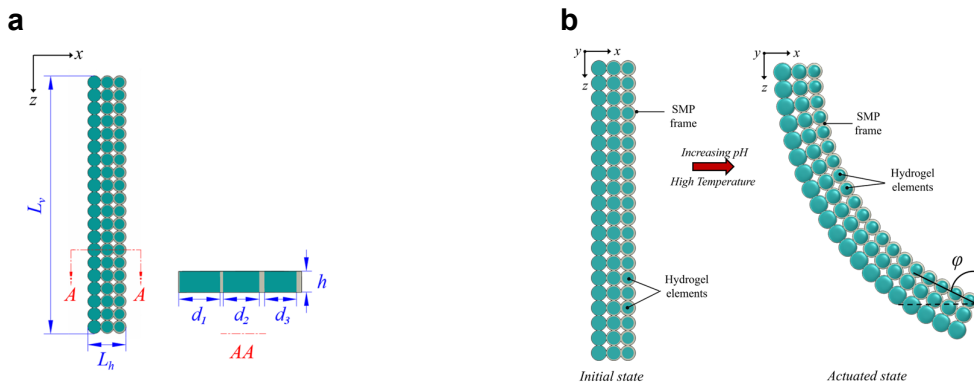


Figure 5.4. The shape-morphing structure: bending building block (a) structural design (b) working principle

The bending performance affected by different influential parameters is explored, shown in Figure 5.5. The bending performance affected by different structure layers is shown in Figure 5.5(a). The black curve represents the φ changing by L_v with L_h of 3, while the red curve represent the φ changing by L_h with L_v of 20. The φ increased linearly by increasing L_v , and can reach 65.3° when L_v is 20. Conversely, φ decreases sharply from 79.2° with increasing L_h , then stabilizes around 5° . Therefore, in practical applications of morphing structures, a larger bending angle can be achieved by increasing the number of vertical layers and reducing the number of horizontal layers. The bending performance affected by the thickness difference is shown in Figure 5.5(b). As ξ_t increased from 0.1 mm to 0.5 mm, φ rose sharply from 53.2° to 85.4° . Besides, as ξ_t further increased from 0.5 mm to 1 mm, φ gradually increased from 85.6° to 92.5° . Thus, increasing the thickness difference between SMP covers also improves the morphing structure's bending performance.

a

b

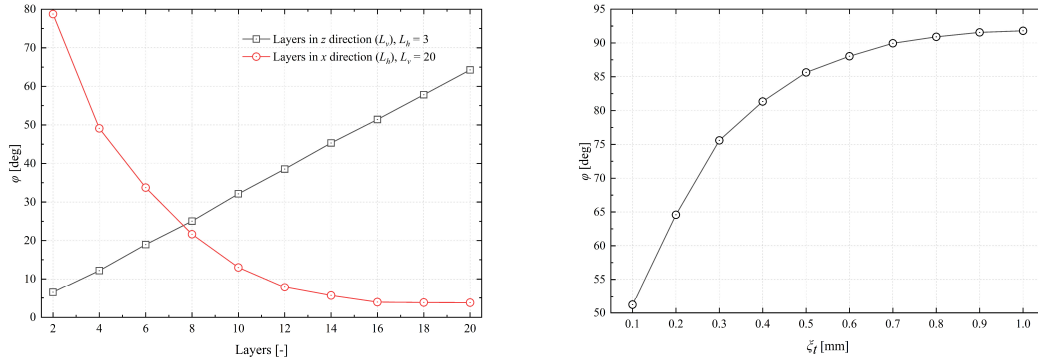


Figure 5.5. The bending performance affected by different influential parameters (a) The bending angle (φ) changes by building block layers (b) The bending angle (φ) changes by thickness difference (ξ_t) under the condition: $L_h = 3$, $L_v = 20$

In addition to bending, the structure need to achieve complicated deformation with increased degrees of freedom to satisfied the industrial requirements. The intelligent structure can also facilitate the assembly of the building block of curling configuration, was shown in Figure 5.6. The structural design is depicted in Figure 5.6(a). The building block of the curling configuration resembles a bending configuration but differs by using a cone frustum hydrogel unit with varying diameters at its top (d_i') and bottom (d_i) surfaces. Moreover, only the diameter on the top side will be changed in the curling configuration, while the diameter on the bottom side will remain consistent with the diameter used in the bending configuration. The thickness difference between two surface (ξ_d) can be expressed as,

$$d_i' - d_i = \xi_d \quad (5.17)$$

The working principle is shown in Figure 5.6(b). Initially, the morphing structure remains straight. Upon actuation of the hydrogel unit, volumetric changes induce bending in the x direction. Additionally, due to the cone frustum shape, differential swelling on the front and back sides causes bending in the y direction. Consequently, the morphing structure achieves a curling deformation by combining these bending behaviors in multiple directions, and the curling deformation is characterized by the displacements in the free end.

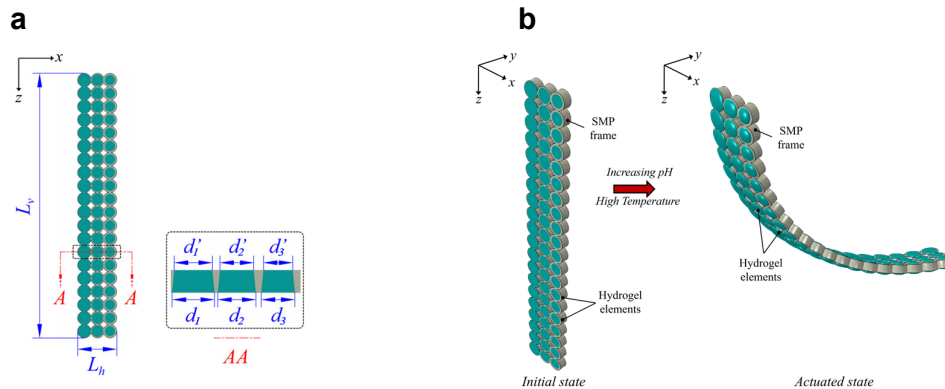


Figure 5.6. The shape-morphing structure: curling building block (a) structural design (b) working principle

The curling performance affected by different ξ_d is explored shown in Figure 5.7. Figure 5.7(a) shows the displacement ratio in the y direction along the structure. As ξ_d increases, the displacement in the y direction not only increases but does so at an accelerating rate. This indicates that increasing ξ_d significantly enhances bending deformation in the y direction. Figure 5.7(b) describes the displacement ratio in the x direction along the structure. As ξ_d increases, the displacement in the x direction gradually increases but remains minimal, indicating that ξ_d has a limited effect on bending deformation in the x direction. Combined with the bending behaviors shown in Figure 5.4, in the curling configuration, bending deformations in different directions appear relatively independent. Therefore, ξ_d and ξ_t are the independent input to design the different morphing structure of curling configuration with varying bending deformations in different directions.

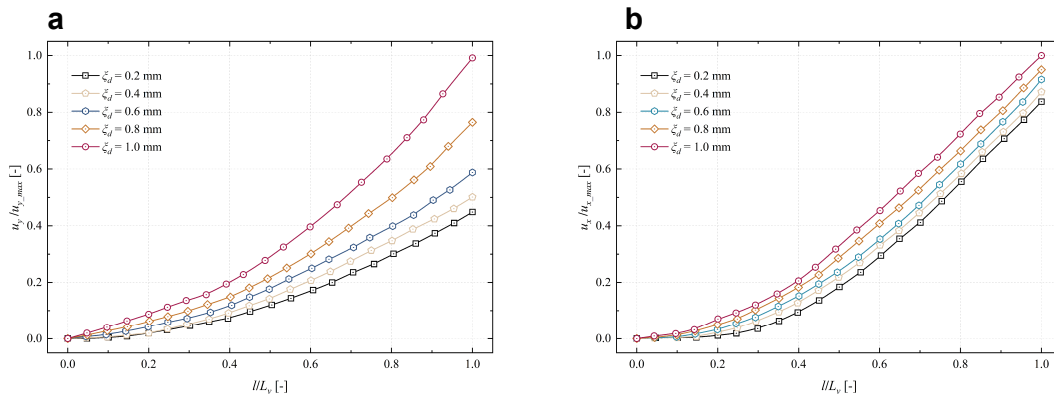


Figure 5.7. The curling performance affected by different diameter difference (ξ_d) (a) The displacement ratio in y direction (b) The displacement ratio in x direction

More complex deformations can be achieved through the curling configuration, as demonstrated in Figure 5.8. Figure 5.8(a) illustrates that by increasing the number of layers in the structure, a ring shape is formed. This ring-shaped structure is suitable for applications such as underwater pipeline installation and maintenance. Additionally, Figure 5.8(b) shows that by reversing the arrangement of the layers, an S-shaped structure is produced. This S-shaped structure is useful for seabed exploration.

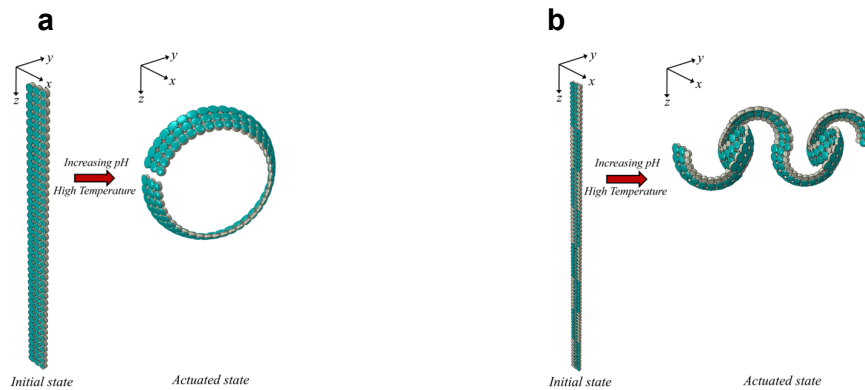


Figure 5.8. Different applications of curling configuration (a) Large deformation for pipeline installation and maintenance (b) Exploration of the space

Furthermore, the intelligent structure can form three-dimensional (3D) building block that achieve elongation deformations to satisfy the requirement of space exploration underwater, which shown in Figure 5.9. The structural design is shown in Figure 5.9(a). The intelligent units placed symmetrical in one layer and linked by SMP frame, and using multiple layers of units to form the 3D structure. The lengths of the structure in x direction and z direction are P_h and P_v , respectively. Besides, the distance between the SMP links is n of 28 mm, the diameters of cone frustum hydrogel unit at top and bottom side are d_e and d_e' , respectively, and set d_e' with a fixed value of 9.8 mm. The diameter difference is also expressed as ξ_d . The elongation configuration's working principle is illustrated in Figure 5.9(b). Initially, the structure is cylindrical. Upon activating the units, the structure elongates due to the swelling of the hydrogel units. Concurrently, the difference in diameter causes each branch to bend. Consequently, the actuated state results in an elongated dumbbell-like structure. The elongation performance is described by the changes in the length, which can be expressed as,

$$\begin{aligned}\Delta P_h &= P_h' - P_h, \\ \Delta P_v &= P_v' - P_v\end{aligned}\quad (5.18)$$

where P_h' and P_v' are the elongated length in x direction and z direction, respectively. In addition, the length change is normalized as a dimensionless number e' , which is expressed as $\Delta P/P$.

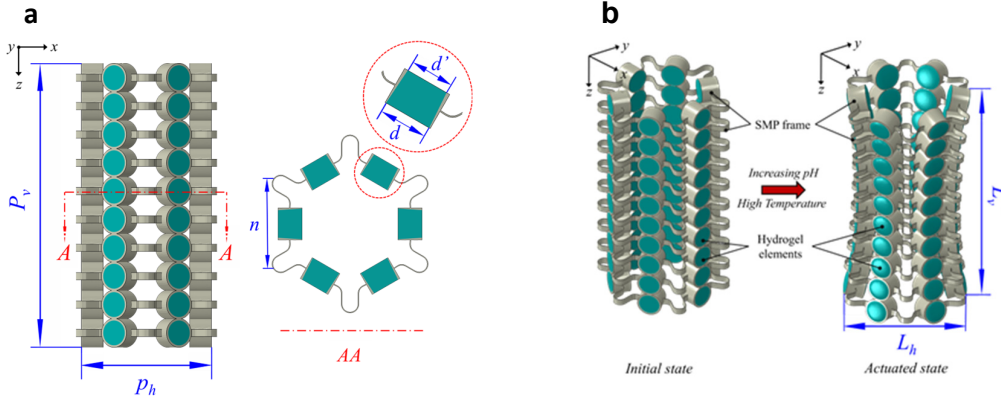


Figure 5.9. The shape-morphing structure: elongation mode (a) structural design (b) working principle

The elongation performance affected by actuator layers and ξ_d is shown in Figure 5.10. As the amount of layers increases, e' increases significantly in the x direction but less in the z direction, which indicates that the elongation in the vertical direction is largely independent of the structure's length, whereas the elongation in the horizontal direction is highly sensitive to variations in the structure's length. In addition, as ξ_d increases, e' decreases sharply from 0.0 mm to 0.3 mm and then gradually from 0.3 mm to 1.0 mm in the z direction. Conversely, e' increases sharply in the x direction. Thus, diameter differences negatively impact elongation in the vertical direction and affect elongation sensitivity in the horizontal direction.

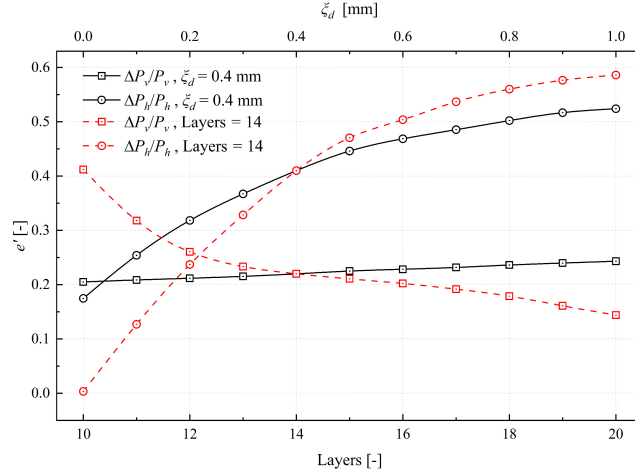


Figure 5.10. The elongation performance affected by actuator layers and actuator diameter difference (ξ_d)

5.4.2 Stiffness variation of the morphing structure

The SMP applied in the morphing structures is used for stabilizing the hydrogels and achieving the stiffness variation. The bending stiffness (S_a) of the structure of bending configuration is analyzed to evaluate the stiffness of the structure, which can be expressed as,

$$S_a = \frac{F_E L_s \sin \beta}{\theta} \quad (5.19)$$

as shown in Figure 5.11 (a), F_E illustrates the external force, L_s is the distance from the top end to the bending point. Thus, $F_E L_s \sin \beta$ is the external moment about the top end. In addition, θ illustrates the rotational angle caused by the external moment.

To evaluate the effects of the stiffness variation of SMP, a comprehensive comparison of proposed morphing structure and other actuators is analyzed in Figure 5.11(b), which includes particle-based actuator [281], particle jamming actuator [275], fiber-reinforced actuator [282], and pneumatic actuator [282]. Additionally, temperatures of 360 K and 295 K are established for the SMP in its rubbery and glassy states, respectively. The proposed morphing structure exhibits a stiffness in the glassy state that is 10 times greater than in the rubbery state, demonstrating the effectiveness of the phase transition in SMP for varying stiffness. Additionally, this structure surpasses others, maximum with a stiffness up to 1.2 times higher than the particle-based actuator, 1.35 times higher than the particle jamming actuator, 1.42 times higher than the fiber-reinforced actuator, and 11.3 times higher than the pneumatic actuator. These findings indicate that employing an SMP frame is a highly effective method for enhancing structural stiffness.

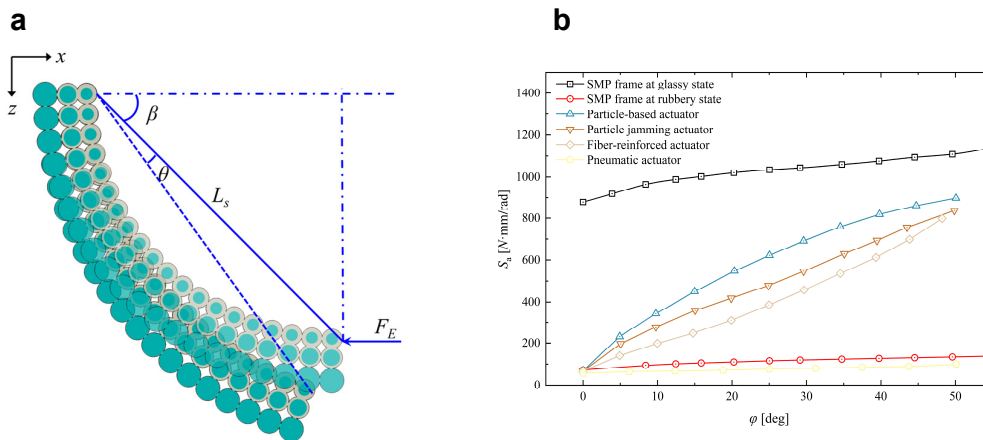


Figure 5.11. The bending stiffness illustration and analysis (a) *Illustration of the calculation of the bending stiffness* (b) *The bending stiffness (S_b) comparison of different actuators*

5.5 Conclusion

In this chapter, multiple smart materials, including smart hydrogel and shape memory polymer, are combined into a meta-structure to construct the mechanically intelligent morphing structure, enabling self-actuation and different deforming configurations.

The pH-sensitive hydrogel and shape memory polymer (SMP) are employed to create the morphing structures that enables self-actuation and stiffness variation. Self-actuation occurs through an increase in pH, while stiffness enhancement is achieved by lowering the temperature. The morphing structure is assembled by cylindrical building blocks which developed by model-based design. The simulation results relating to the hyperplastic behaviors of SMP and pH-sensitive hydrogels are matchable with experimental data, which proves the feasibility of the materials model.

The development of tailored morphing structures capable of bending, curling, and elongation is achieved through the use of variable intelligent structures with diverse designs. The bending and curling configurations utilize multilayer hydrogel units within a SMP frame, while the elongation configuration comprises hydrogel units, an SMP frame, and connecting elements. Bending performance is assessed by the bending angle, which increases with the number of vertical layers and thickness differences, but decreases with the number of horizontal layers. Curling performance is measured by displacements in various directions, predominantly influenced by axial thickness differences and minimally by vertical thickness differences. Elongation performance is evaluated by the elongation ratio, which increases horizontally with both thickness differences and the number of layers, but decreases vertically with thickness differences.

Using SMP as the morphing structure frame effectively enables stiffness variation. In its rubbery state, the bending stiffness of the proposed structure is slightly higher than that of a pneumatic actuator. However, once the SMP transitions to its glassy state, the bending stiffness

increases tenfold compared to the rubbery state, exceeding particle-based, particle jamming, and fiber-reinforced actuators.

The higher pH of seawater compared to air is ideal for actuating pH-sensitive hydrogels, and the waste heat generated during subsea operations can effectively drive SMPs. This makes the proposed structure highly suitable for underwater applications and subsea operations, supporting various morphing structures.

The proposed hydrogel-SMP-based building block enables morphing structures with self-actuation and variable stiffness, providing the foundation for mechanical intelligence. To apply this mechanical intelligence in practical soft robotic systems, synchronized operations are crucial. Therefore, the next chapter will bridge the gap between potential mechanical intelligence and practical applications. It will focus on designing and implementing a control system for morphing structures that integrates multiple smart materials responding to a unified stimulus, enabling cooperative actuation to perform specific tasks.

6 Integrated system design of the collaborative smart materials in a building block*

Chapter 5 discusses the development of morphing structures constructed using multiple smart materials, highlighting the potential to achieve mechanical intelligence through self-actuation and stiffness variation. To integrate mechanical intelligence into soft robotic systems, it is essential to realize synchronized operations. This requires the collaborative actuation of multiple smart materials and their integration, enabling controllable responses to a unified stimulus and ensuring the morphing structures achieve the desired deformations. The synergy between mechanically intelligent morphing structures and operational control brings them as a solution for executing specialized tasks, such as underwater exploration and precision gripping. To meet these requirements, this chapter presents the design and implementation of an integrated system for morphing structure based on multiple smart materials responding to a unified stimulus. Section 6.2 describes the integrated system, including structural design of the building block and the control circuit design for tailored temperatures. In Section 6.3, the numerical modeling is proposed to describe the properties smart materials, the experimental setup is proposed for manufacturing the morphing structure, and thermal control algorithm is designed for managing the temperature to achieve the cooperative actuating of shape memory materials. Section 6.4 verifies the feasibility of the proposed morphing structure and thermal control algorithm, then analyzes different performances of the integrated system embedded morphing structure. Finally, Section 6.5 gives the conclusions.

* This chapter is based on Q. Chen, R. Wu, D. Schott, and J. Jovanova, "Integration System Design of SMA-SMP Based Morphing Structure for Soft Robotics," submitted to IEEE/ASME transaction on mechatronics

6.1 Introduction

Shape memory materials are notable for their ability to remember and return to a pre-defined shape after undergoing significant deformation [302], when exposed to specific external stimuli. This unique property, observed in materials such as NiTi alloys and polylactic acid (PLA), has broad applications in industries including aerospace, automotive, and precision manufacturing [303]. Mechanistically, shape memory materials are categorized into two primary types: Shape Memory Alloys (SMAs) and Shape Memory Polymers (SMPs) [304]. SMAs are commonly used as soft actuators due to their relatively simple implementation, such as a bionic jellyfish robot is developed to produce contraction-recovery motion utilized SMA [305]. Although the kinematics and mechanical properties of SMA actuators can be measured and modeled during their transition to memory shapes, a major challenge remains: the limited number of stable states restricts their effectiveness as robotic actuators. SMPs have become widely used due to their low density and high biocompatibility. Lan et al. created a thermoset styrene-based SMP composite to construct a hinge mechanism for deploying a solar panel [306]. However, SMP actuators can only undergo passive shape changes without active self-actuation, which limits their use as primary actuators in adaptive soft robotic systems.

When designing controller logic, it is crucial to monitor the temperature of thermal-sensitive SMAs or SMPs to set operating conditions and prevent overheating that could cause memory loss [307]. Early studies utilized thermocouples to monitor SMA wire temperature [308], however, non-contact tools like infrared sensors and thermal imagers are now widely used. These tools enable precise measurement of temperature distribution across the target surface, allowing for accurate control over localized heating or cooling. This capability is especially beneficial for SMPs, which have low thermal conductivity. To advance beyond single-function, fixed behaviors typically managed by open-loop systems, closed-loop control is essential. This approach allows for the adjustment to uncertainties by using feedback to monitor and respond to changes in actuator deformation [237, 309, 310]. In morphing structures made from thermally-sensitive materials, external influences frequently affect the thermodynamic model, while the nonlinear behavior of shape memory materials complicates the ability of model predictive control (MPC) to accurately forecast system responses. Currently, no effective control methods or systems are specifically tailored for morphing structures that use multiple thermal response smart materials.

This chapter presents an integrated mechatronic system designed for a morphing structure based on SMP meta-structure and SMA springs, enabling comparative work of multiple smart materials for mechanical intelligence. The main contributions can be summarized as follows. First, a morphing structure incorporating multiple types of shape memory materials is proposed, which allows customizable deformations. Secondly, a temperature multi-functional thermal sensing and control system using unsupervised learning is introduced, enabling the synchronized operation of actuating the SMA springs and SMP frame. Then, by embedding the control system into the morphing structure, the integration system is developed that achieves coordinated control of SMA-SMP structure, allowing the execution of self-actuation and stiffness variation within the same stimulus. This system facilitates the collaborative dynamic

control of morphing structures using shape memory materials, paving the way for adaptive mechanical intelligence in soft robotic applications.

6.2 Design of the building block and integration system

6.2.1 Structural design

To enable adaptable deformation for soft robotics, the intelligent building block characterized by SMA springs and SMP meta-structure is proposed into a single structure connected by two polymethyl methacrylate (PMMA) plates. As shown in Figure 6.1(a), the design features an SMP structure with three SMA springs around it. The SMA springs provide movement force, while the SMP core acts as a switch, controlling the actuator's shape-locking ability through stiffness adjustment. Using a two-way shape memory effect, the SMA springs shift between high-temperature and low-temperature shapes [311]. Once the desired movement is achieved, the SMP core transitions from flexible to rigid, locking the structure's shape through precise temperature control [312]. Furthermore, the SMP structure is designed in a cylindrical shape to allow for movement in multiple directions. The working process is illustrated in Figure 6.1(b). Initially, the entire structure remains straight at room temperature (298 K). To begin the process, the SMP structure is heated to reduce its stiffness, allowing it to change shape. Next, by selectively heating three SMA springs, the structure bends in specific directions and angles as needed. Finally, the SMP structure is cooled to restore stiffness, which locks it into the new shape, which's bending performance is evaluated by bending angle (φ). Additionally, when the SMA springs return to room temperature, simply reheating the SMP structure enables it to revert to its original shape. Furthermore, the building block can transition from its initial state or between working configurations through a stepping process. As illustrated in Figure 6.1(b), once the building block reaches Working Configuration 1, it can lock into that shape. Then, by independently controlling the SMA springs, another SMA spring can be activated to transition to Working Configuration 2. This stepping mechanism enables the building block to switch between different configurations, supporting a wide range of shape transformations.

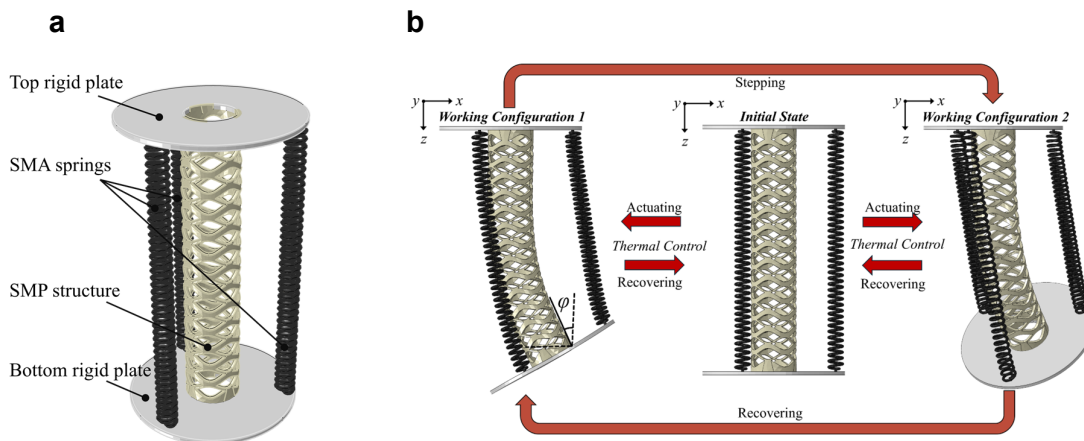


Figure 6.1. The proposed building block structure and working principle (a) *Demonstration the structure* (b) *Working process of the building block*

The detailed geometric parameters are presented in Figure 6.2. The cylinder has a length L of 200 mm, an inner diameter d_c of 35 mm, and a wall thickness t_p of 2.5 mm. The connection boards on both ends have a thickness t_c of 3 mm, with a total diameter D of 106 mm. The deployment holes for the SMP springs are uniformly distributed along a circle with a radius r_h of 45 mm. The SMP meta-structure is defined by a waved lattice unit. Each lattice unit has a total length l_m of 30 mm, with a middle gap length l_h of 21.35 mm. The upper layer of the lattice has a thickness t_u of 1.8 mm, while the lower layer has a thickness t_d of 4 mm.

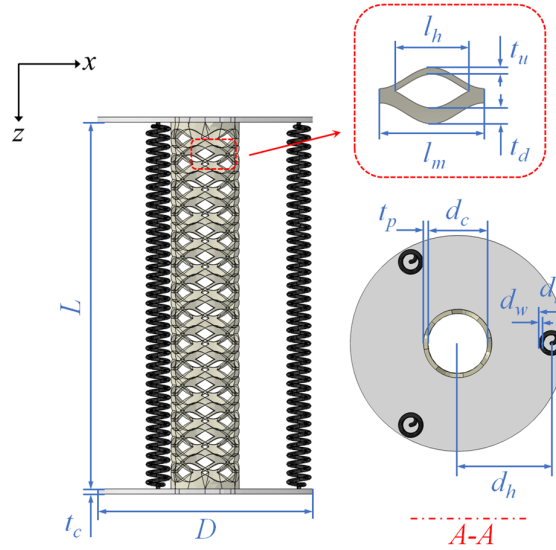


Figure 6.2. Geometric parameters

6.2.2 Control circuit design

The proposed design emphasizes temperature as the central factor influencing the system's performance, with heating and cooling identified as the main control actions. To preserve the deformed shape and prevent any loss of shape memory, the SMP structure requires precise temperature regulation. For this purpose, a Pulse Width Modulation (PWM) circuit, as illustrated in Figure 6.3(a), is utilized to maintain accurate temperature control. On the other hand, SMA springs do not require such strict temperature control. However, to achieve specific bending behaviors, SMA springs must undergo deformation through multiple steps. To facilitate this controlled deformation, a MOSFET-based switching circuit operating in a stepwise mode is employed, as shown in Figure 6.3(b). This setup allows the SMA springs to deform progressively, ensuring tailored bending responses without needing the precise temperature adjustments necessary for the SMP structure.

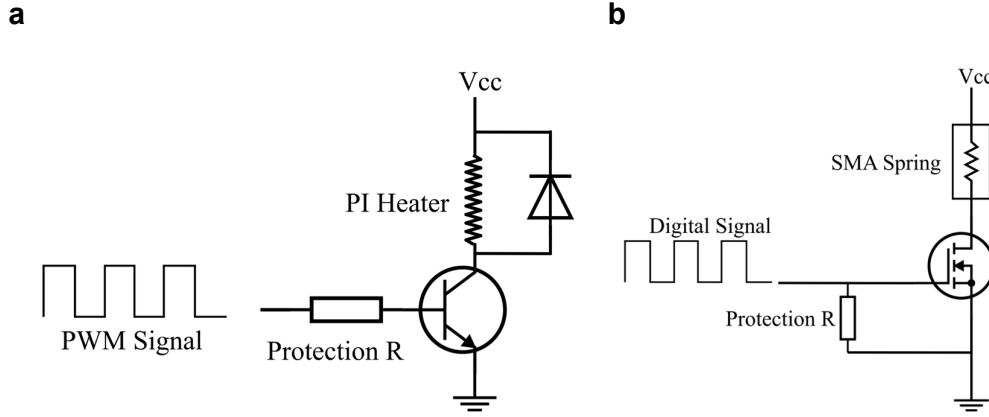


Figure 6.3. Control circuit design (a) *PWM control circuit for SMP* (b) *Switching control circuit for SMA*

6.3 Methodology

6.3.1 Numerical modeling

The finite element method (FEM) is used in this study to model smart materials and analyze the performance of proposed morphing structure [60]. To simulate SMA behavior, an isotropic thermo-mechanical constitutive model was implemented as an ABAQUS user-defined material (UMAT) [61, 62]. The Helmholtz free energy per unit reference volume is calculated as:

$$\psi = \psi^e + \psi^\xi + \psi^\tau \quad (6.1)$$

$$\psi^e = \widehat{\psi}^e(\mathbf{E}^e, \tau) = \frac{1}{2} \mathbf{E}^e \cdot \mathbb{C}[\mathbf{E}^e] - \mathbf{A}(\tau - \tau_0) \cdot \mathbb{C}[\mathbf{E}^e] \quad (6.2)$$

$$\psi^\xi = \widehat{\psi}^\xi(\tau, \xi) = \frac{\lambda_T}{\tau_T} (\tau - \tau_0) \xi \quad (6.3)$$

$$\psi^\tau = \widehat{\psi}^\tau(\tau) \quad (6.4)$$

In these expressions, ψ^e is the thermos-elastic free energy density, $\mathbf{E}^e = \frac{1}{2}(\mathbf{C}^e - \mathbf{I})$ denotes the elastic strain, and $\mathbf{C}^e = \mathbf{F}^{eT} \mathbf{F}^e$, demonstrates the elastic distortion. $\mathbb{C} = 2\mu \mathbb{I} + \left(\kappa - \frac{2\mu}{3}\right) \mathbf{I} \otimes \mathbf{I}$ is the fourth-order elastic moduli tensor where μ shows the shear modulus and κ shows the bulk modulus. $\mathbf{A} = \alpha \mathbf{I}$, is the second order thermal expansion tensor where α being the thermal expansion coefficient. τ shows the current temperature, and τ_0 represents the reference temperature. ψ^ξ shows the free energy density of phase transformation, ΔH_T shows the constant latent heat of phase transformation, $\xi \in [0, 1]$ denotes the martensitic volume fraction and $\tau_T = (M_s + A_s)/2$ denotes the transformation temperature, where M_s is the start temperature of martensite, A_s is the start temperature of austenite. In addition, ψ^τ represents the pure thermal free energy density.

According to the Helmholtz free energy, the stress tensor can be expressed as:

$$\mathbf{T} = \frac{\partial \psi}{\partial \mathbf{E}^e} = \mathbb{C}[\mathbf{E}^e - \mathbf{A}(\tau - \tau_0)] \quad (6.5)$$

And the elastic distortion can be considered as part of the total deformation gradient $\mathbf{F} = \mathbf{F}^e \mathbf{F}^{inel}$ where \mathbf{F}^{inel} is the inelastic transformation distortion being found from:

$$\dot{\mathbf{F}}^{inel} = \{\sqrt{1.5} \bar{\varepsilon}_t \dot{\xi} \mathbf{S}\} \mathbf{F}^{inel} \quad (6.6)$$

where $\mathbf{S} = \frac{sym(\mathbf{C}^e \mathbf{T})_{dev}}{|sym(\mathbf{C}^e \mathbf{T})_{dev}|}$ shows the inelastic flow direction and $\bar{\varepsilon}_t$ is the maximum transformation strain.

In this study, the SMA (Ni-Ti alloy) wires are with martensite start temperature $M_s = 325$ K, martensite finish temperature $M_f = 315$ K, austenite start temperature $A_s = 341$ K, and austenite finish temperature $A_f = 351$ K. In addition, elastic modulus of the alloy in martensite phase and in austenite phase are 28 GPa and 75 GPa, respectively.

To elucidate the mechanical behavior of SMP, the superimposed generalized Maxwell model and Williams-Landel-Ferry (WLF) equation within Abaqus finite element solver are utilized. The utilized constitutive equations for the multi-branch viscos-elasticity are as follows [243],

$$\sigma(t) = \varepsilon_0 E_n + \varepsilon_0 \sum_{i=1}^{n-1} E_i e^{-\frac{t}{\tau_i}} \quad (6.7)$$

where $\sigma(t)$ represents stress at time t , ε_0 is the strain at the initial time, E_n is the instantaneous modulus, E_i is the elastic modulus and τ_i is the relaxation time of the Maxwell element i . The relation of relaxation modulus E in the generalized Maxwell equation with time t is expressed as:

$$E(t) = E_n + \sum_{i=1}^{n-1} E_i e^{-\frac{t}{\tau_i}} \quad (6.8)$$

satisfying the limit condition:

$$\lim_{t \rightarrow \infty} E(t) = E_n \quad (6.9)$$

Performing relaxation experiments at different temperatures and using the time–temperature equivalence principle is crucial. This approach enables the transformation of the relaxation response curves of SMP from various temperatures into a unified relaxation response curve at a chosen reference temperature. According to the WLF equation [243], the connection between the relaxation time at the present temperature T and the relaxation time at the reference temperature of T_r is given by:

$$\lg \alpha_T = \lg \frac{\tau}{\tau_r} = \frac{-C_1(T - T_r)}{C_2 + (T - T_r)} \quad (6.10)$$

where α_T represents shift factor, C_1 and C_2 are material constant. It is assumed that the glass transition temperature T_g is equivalent to the T_r . Furthermore, Polylactic acid (PLA) was chosen

as the SMP in this study [297]. The viscoelastic and thermal property parameters are specified as follows, $T_g = 334$ K, $C_1 = 6.14$, and $C_2 = 293$ K [298]. At a temperature of 298 K, the material's elastic modulus was 1000 MPa, but it decreased by 60% when reaching the transition temperature.

6.3.2 Experimental setup

The SMP cylinder was produced using a Builder EXTREME 1500 PRO 3D printer with PLA filament. The SMA springs were made from a Ni-Ti alloy with a wire diameter of 2.3 mm, which has minimal decomposition tendencies, and were trained using the TWSME process [313]. The springs are designed to contract to 100 mm when heated and extend to 200 mm upon cooling. The upper and lower circular connectors, which secure the actuators, were laser cut from 3 mm thick PMMA plates. The cooling fan used is a Delta AFB0912HH, capable of a maximum airflow of approximately 58 CFM. As for the control part, the MLX90640 infrared thermal imaging sensor array is utilized, which provides a 32x24 temperature matrix and adjusts its measurements based on ambient temperature [314].

The connection of each component is shown in Figure 6.4(a). The SMA springs are directly powered and heated via Joule heating, and no additional cooling equipment is needed due to the relatively low cooling demands of the springs. Since SMP has poor electrical and thermal conductivity, an external heating element is required. Polyimide film heating pads (PI heaters), fabricated to match the inner surface of the SMP cylinder, were used. These heaters have very low stiffness, excellent insulation, and high thermal conductivity, and utilize thin etched stainless steel alloy sheets as heating elements. This design ensures the heaters have negligible impact on the structure's bending motion while preventing the SMP from exposure to any external electrical stimuli that could introduce errors. To accelerate cooling, a small fan is placed at the top of the cylinder, utilizing the air duct formed by the PI heaters. This setup also minimizes any cooling interference between the SMP and SMA. The sensor should be positioned at a distance of 50–100 mm from the cylinder, avoiding placement near the upper and lower ends. Additionally, the power system layout is illustrated in Figure 6.4(b). Each SMA spring is connected to a single power supply, with a maximum output of 5.0 V and 15.0 A, via a switching circuit. The PI heaters and cooling fan are connected to a separate power supply, capable of a maximum output of 18.0 V and 10.0 A, through a PWM circuit.

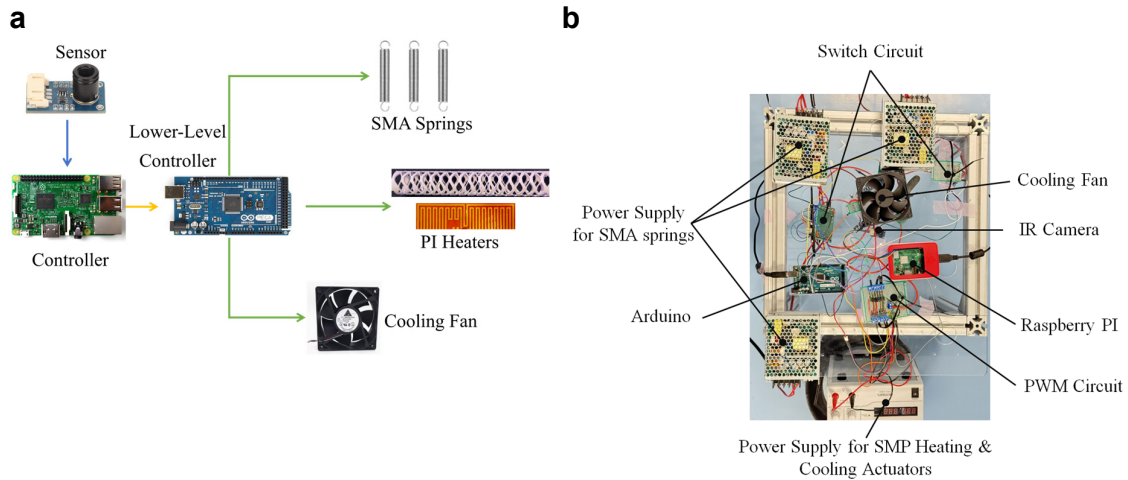


Figure 6.4. The experimental setup (a) connection of each component (b) layout of the power system

6.3.3 Sensing and control algorithm

Precise temperature control of the SMP is crucial for implementing the proposed solution. Accurate detection of the target area's temperature is necessary to establish a closed-loop control system. This section introduces a measurement solution tailored to the structure, referred to as the Multi-Target Thermal Sensing (MTTS) method.

6.3.3.1 Machine Learning-based Multi-Targets Thermal Sensing method

The resolution of 768 temperature data points in the temperature matrix provided by the sensor is still not enough to support the temperature calculation of a certain area. On the other hand, these few data points contain data from multiple layers and cannot be directly used for statistical calculations. Therefore, the first step is to develop the image processing which is imperative to obtain more accurate results. Based on the cubic interpolation [315], more obvious grid-like distribution of the sensing area will be obtained. Then, the K_m -means clustering algorithm, an unsupervised learning method, is utilized to partition the data into K_m distinct clusters based on inherent similarities. The algorithm operates solely on the statistical relationships among the features and the chosen value of K_m [316]. In this particular case, temperature is the only feature used in the clustering process. The first step of K_m -means involves initializing the cluster centroids by randomly selecting K_m data points from the temperature matrix and using their values as the initial centroids. In the second step, the Euclidean distance for each data point x_i to each centroid c_j is calculated using Equation (6.11), and each point is assigned to the cluster with the shortest distance.

$$d(x_i, c_j) = \sqrt{(x_i - c_j)^2} = |x_i - c_j| \quad (6.11)$$

Then, the third step updates the centroids: the mean of all temperature values within each cluster C_j is computed utilizing Equation (6.12), and this mean becomes the new centroid for the corresponding cluster,

$$c_{j-new} = \overline{x_{i \in C_j}} = \frac{1}{|C_j|} \sum_{x_i \in C_j} x_i \quad (6.12)$$

Finally, the second and third steps are repeated iteratively until the centroids converge and no longer exhibit significant changes. Mathematically, this process aims to minimize the sum of squared errors (SSE), as represented by Equation (6.13),

$$SSE = \sum_{j=1}^{K_m} \sum_{x_i \in C_j} (x_i - c_j)^2 \quad (6.13)$$

According to the meta-structure of the SMP and the heating process, the MTTs method is proposed based on the extraction process. The main sensing area is divided into five areas to detect the different zones. the first target region corresponds to areas where the PI heater group is exposed, with its average temperature termed the first target temperature. The second target region represents the outer surface, influenced by cylinder thickness and heat transfer, and its mean temperature is the second target temperature. Additional third to fifth areas express the cylindrical area with thermal inaccuracies for geometric factors, the radiation area capturing heat dissipation, and the background. The primary regions, including the first and second target regions, inform control integration, establishing a cross-sectional temperature range from first target temperature (maximum temperature in SMP) to second target temperature (minimum temperature in SMP). As a result, the SMP with varying thicknesses in the cylinder's cross section can be regarded as being at a temperature between the two target values.

6.3.3.2 Control algorithm and system

A basic control system was created to allow the morphing structure to carry out its intended functions. Additionally, this system includes an integrated interface, making it adaptable for future high-level control and interaction. The control system includes the closed-loop temperature control algorithm based on the SMP and the system's operating logic.

The system utilizes a Proportional-Integral-Derivative (PID) closed-loop control mechanism to maintain precise temperature regulation for the SMP-based meta-structure across nearly all operational modes. The basic output of PID controller is presented by Equation (6.14),

$$\begin{aligned} u(t) &= K_p e_p + K_i e_i + K_d e_d \\ &= K_p e(t) + K_i \int_0^t e(\tau) d\tau + K_d \frac{de(t)}{dt} \end{aligned} \quad (6.14)$$

In each mode, the temperature controller receives real-time measurement signals from a set of sensors. Using the proposed sensing system, it identifies the first target region and second target region, which are areas within the SMP structure that are crucial for the control system to achieve optimal temperature outcomes. These regions are weighted differently depending on the operational mode, allowing the system to adjust the temperature precisely according to the mode-specific requirements. Based on the current temperature $T_c(t)$ and target temperature T_t for the active mode, the control system calculates the current output $u(t)$. At any moment, the error is defined as,

$$e(t) = T_t - T_c(t) \quad (6.15)$$

considering the time step of a sensing interval Δt , the errors are typically calculated or estimated as follows,

$$\begin{cases} e_p(t) = e(t) \\ e_i(t) = \Delta t \sum_{\tau=0}^t e(\tau) \\ e_d(t) = \frac{e(t) - e(t-1)}{\Delta t} \end{cases} \quad (6.16)$$

The proposed output $u(t)$ is sent to an Arduino board, which then directs the actuators to modify the temperature. The PID control method continually adjusts the heating or cooling rates to minimize temperature deviation from the target, thus stabilizing the system's thermal response. This feedback loop enables fine-tuned control over the SMP structure, ensuring reliable and responsive operation.

In addition, The control system for the morphing structure's trunk is designed to function within five distinct operational modes, each serving a unique role in adapting the structure to varying tasks. Shown in Figure 6.5, upon system activation and initialization, the control logic enters one of these five modes, including standby, small stepping, large stepping, forming, and recovery modes. The mode selection process is influenced by both user input and pre-programmed criteria, allowing the system to dynamically switch modes in response to environmental conditions or task requirements. Each mode has specific parameters for temperature and actuator settings, optimized for the targeted behavior of the morphing structure. The transition between modes is managed seamlessly by the control system, which continuously monitors sensor data and user commands to adapt the system's behavior accordingly. The control interface also supports real-time adjustments by the user, offering flexibility for interactive and adaptive operation.

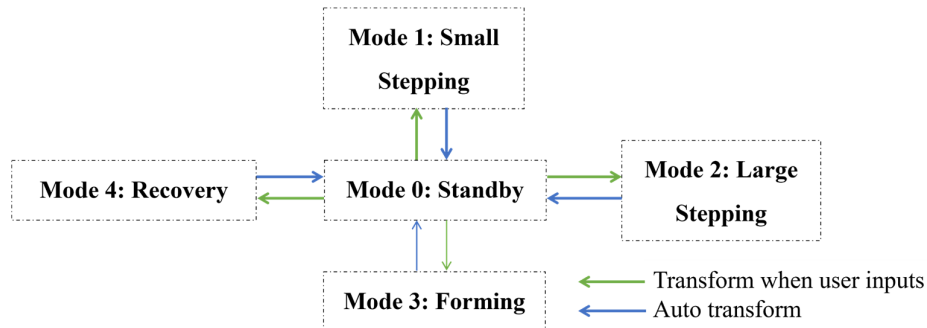


Figure 6.5. Five modes of the control system and their transformation relationships

6.4 Results and discussion

6.4.1 Verification of the control system and motions of morphing structure

To verify the MTTTS method, the temperature distribution of the heated SMP structure is evaluated. The initial data from the sensor comprises 768 temperature points, which is insufficient for precise area-based temperature calculations. The temperature distribution contour is shown in Figure 6.6(a), the left figure illustrates the original sensor data using a jet color palette, the middle figure shows the outcome after applying cubic interpolation, and the right figure depicts the identification mask. In the detection results, regions labeled 1 to 5 represent the first target region, the second target region, the cylindrical area, the radiation zone, and the background, respectively. Figure 6.6(b) displays the temperature monitoring curve for these areas. By employing the MTTTS method, real-time temperature detection is achieved, ensuring the temperature remains stable around the target value.

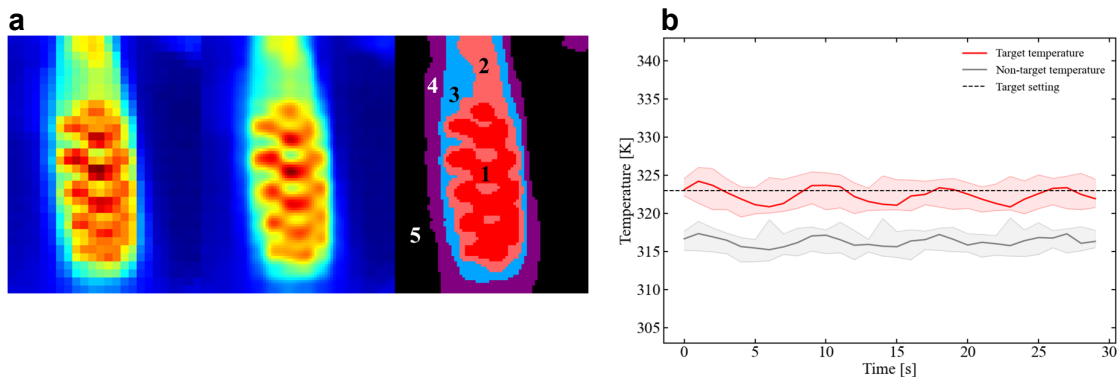


Figure 6.6. Verification of the temperature control system (a) *Identification masks based on MTTTS method* (b) *Temperature distribution detected by MTTTS method*

The bending performance is then evaluated by comparing simulation results with experimental data to confirm the feasibility of the building blocks. For this analysis, the maximum contraction of a single activated Shape Memory Alloy (SMA) spring is defined as the "fully loaded" state. The loading process is represented on a scale from 0 to 100%, indicating the percentage of the loading state relative to the current contraction level of the actuating SMA springs. Figure 6.7 presents a comparison of bending performance, illustrating the single-spring actuation mode in Figure 6.7(a) and the double-spring actuation mode in Figure 6.7(b). As shown in Figure 6.7(a), both the experimental and simulation results for the building block driven by a single spring exhibit similar trends, reaching a maximum bending angle of approximately 42° under full loading process. In particular, the numerical data show a linear increase as the loading progresses, whereas the experimental data initially rise more slowly, likely due to environmental factors. Additionally, the numerical results are generally slightly higher than the experimental ones. This discrepancy can be attributed to the rigid connections between parts in the experiment, which limit the bending performance to some extent. However, as the loading process approaches to 100%, the spring provides sufficient force, minimizing the impact of these connections on the experimental outcomes.

As illustrated in Figure 6.7(b), the distribution of double-spring actuation follows a similar trend, achieving a maximum bending angle of around 65° , indicating that the double-spring actuation mode allows for a greater range of motion. However, unlike the single-spring actuation mode, where the bending angle increases steadily throughout the loading process from 0 to 70% then get slowing. Up to 70%, the SMP structure approaches its stretching limit, which results in a slower increase in bending angle between 70% and 100% loading process. In addition, the experiment shows a difference in bending performance of 5° less than the simulation result, which is because the experimental conditions were less controlled than in simulations, resulting in a greater tendency for the SMP structure to fatigue.

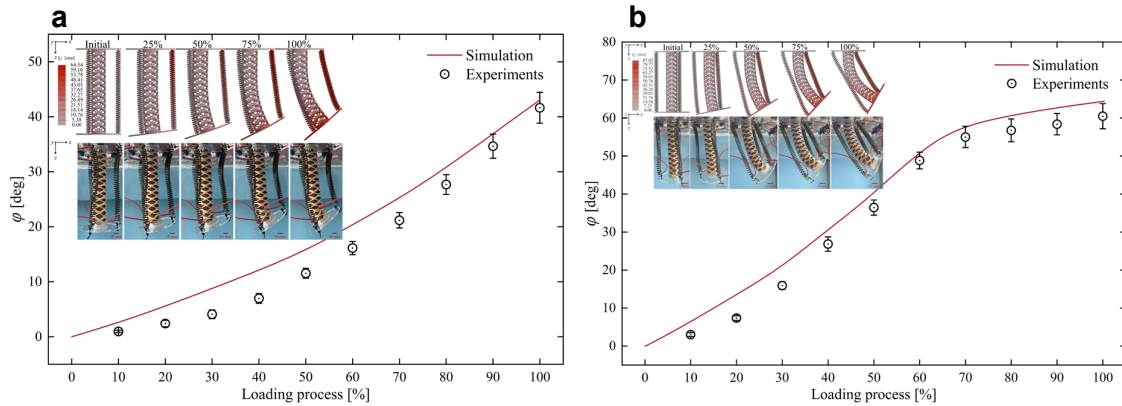


Figure 6.7. Validation of the bending performance (a) *Bending performances of the single-spring actuation* (b) *Bending performances of the double-spring actuation*

6.4.2 System Initialization and Standby Mode

When the control system is activated, as illustrated in Figure 6.8(a), the initialization process begins. Subsequently, Mode 0 is triggered, which can also activate automatically upon the conclusion of other modes. This mode manages the user interaction page to facilitate communication and preheats the SMP to a maximum temperature of 323K. Once an available command is successfully executed, Mode 0 concludes and transitions to the designated mode. The thermal experiment results, presented in Figure 6.8(b), demonstrate that it takes approximately 10 seconds to raise the temperature from room temperature (about 298K) to the target level. Once the target temperature is reached, it is maintained consistently during the preheating phase, in preparation for the subsequent indexing and related actions.

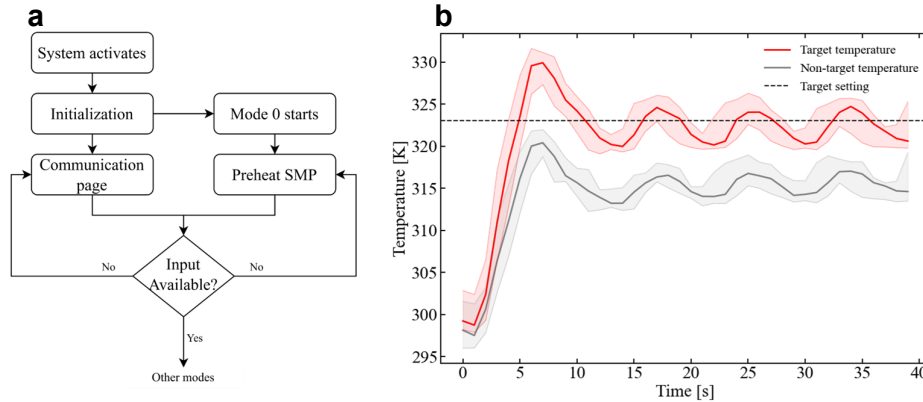


Figure 6.8. Workflow of initialization and standby mode (a) *Flowchart of the working process* (b) *Temperature distribution of the initialization*

6.4.3 Analysis of working modes

During operation, the smart building block performs three key processes: a stepping process for deformation, a forming process to lock its shape by adjusting stiffness, and a recovering process for recovery. These processes are efficiently coordinated by the integrated control system. This section explains these processes in detail, categorized into specific working modes. Furthermore, the structural stiffness, represented as bending stiffness (k_b) is calculated using the method outlined in [109].

The stepping process evaluated by stepping mode, which is shown in Figure 6.9. In the stepping mode, the deformation can pause at any step. This allows posture adjustments from any position without resetting to the initial state. The workflow and temperature distribution are shown in Figure 6.9(a), begin by heating the SMP cylinder to a minimum temperature of 358K. This ensures low stiffness across all layers, preventing resistance to bending and minimizing the risk of cylinder failure. Once the SMP cylinder reaches the target temperature range, the specified SMA springs are sequentially activated with short intervals between steps, while the PI heaters maintain the cylinder's temperature at approximately 358K to ensure stability.

The bending performance and stiffness variations during the stepping mode are illustrated in Figure 6.9(b). The entire process costs 30 seconds and consists of four stepping phases, each lasting 6 seconds, and three pulsing phases, each lasting 2 seconds. During each 6-second stepping phase, the bending angle gradually increases for both the double-spring and single-spring actuating configurations. However, during the 2-second pulsing phases, the bending angle decreases by approximately 2° to 4° . This reduction occurs because, during pulsing, the SMA spring stops heating, while the SMP core remains at a high temperature of 358 K. As a result, the SMP core tends to revert to its original state, leading to a decrease in the bending angle. Additionally, although the double-spring and single-spring actuation modes exhibit different bending angles throughout the stepping phases, their stiffness levels remain consistently low. This is attributed to the SMP core always being in a rubbery state with a low elastic modulus, meaning that the stiffness is primarily determined by the PI heater.

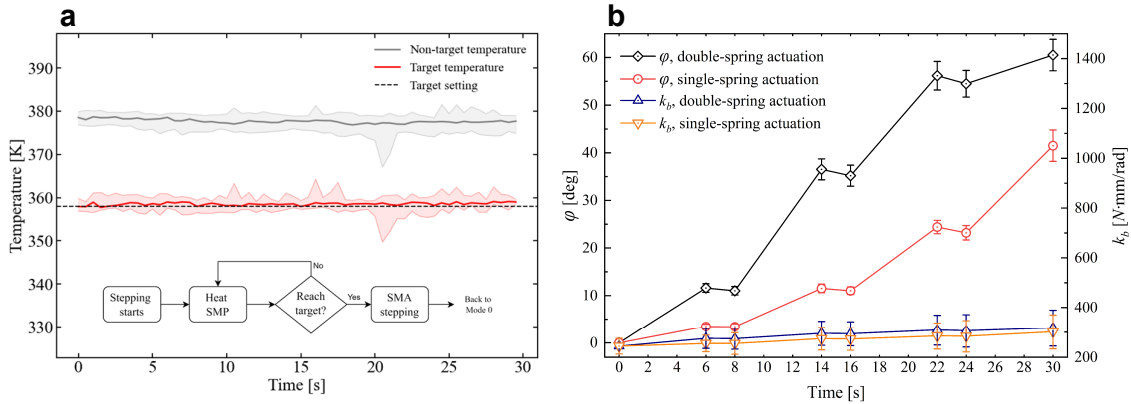


Figure 6.9. Workflow and performance of the building block in stepping mode (a) Working flowchart and temperature distribution (b) Bending performance and stiffness variation of different actuating modes

The forming process and recovering process are evaluated by forming mode and recovering mode, which is shown in Figure 6.10. The workflow and temperature distribution of forming mode are shown in Figure 6.10(a). This mode involves a straightforward process of cooling the SMP cylinder to a minimum temperature of 323K, monitored via thermal detection. Using the air duct formed by the PI heater group on the inner surface of the cylinder, cooling occurs uniformly from top to bottom. The cylinder cools gradually from the inside to the outside, during which a phenomenon known as "hot zone inversion" occurs. This refers to the reversal of positions between the first and second target regions.

The bending performance and stiffness variations of the double-spring actuation during the forming mode are presented in Figure 6.10(b). Initially, the bending stiffness of the material is relatively low due to the heated state of the SMP core. As the temperature gradually drops to the transition range, occurring between 10 and 45 seconds, there is a substantial increase in bending stiffness. By 50 seconds, the stiffness reaches 1400 N·mm/rad, representing a 4.5-fold rise compared to heated state. In addition, the bending angle decreases slightly by 5° (0–20 seconds) as the SMA springs stop actuating, allowing the trend of recovery of the SMP core at high temperatures.

Furthermore, the workflow and temperature distribution of recovering mode are shown in Figure 6.10(c). The initial step is similar to the stepping mode, involving heating the SMP cylinder to a target temperature of 358K, which takes approximately 25 seconds. Once the target temperature is reached, a short pulse is applied to all SMA springs to eliminate stress-induced martensite. This is followed by cooling the cylinder to its initial shape at room temperature, with the PI heaters maintaining temperature stability throughout the process. The bending performance and stiffness variations of the double-spring actuation during the recovering mode are presented in Figure 6.10(d). In this mode, the SMA is also in inactivated state. The bending stiffness decrease sharply from 5 to 20 seconds because of the quick temperature increasing process. Then from 25 to 40 seconds the bending stiffness keeps lower for SMP core being heated. However, as the bending stiffness decreases, the bending angle does not drop suddenly. Instead, it gradually decreases during the first 15 seconds and then declines linearly from 15 to 30 seconds. This delay happens because the bending angle takes time to respond to changes in

bending stiffness. The shape-memory effect is triggered only after the SMP core is fully heated above its transition temperature. At this point, the bending angle begins to decrease and progressively recover to the initial state.

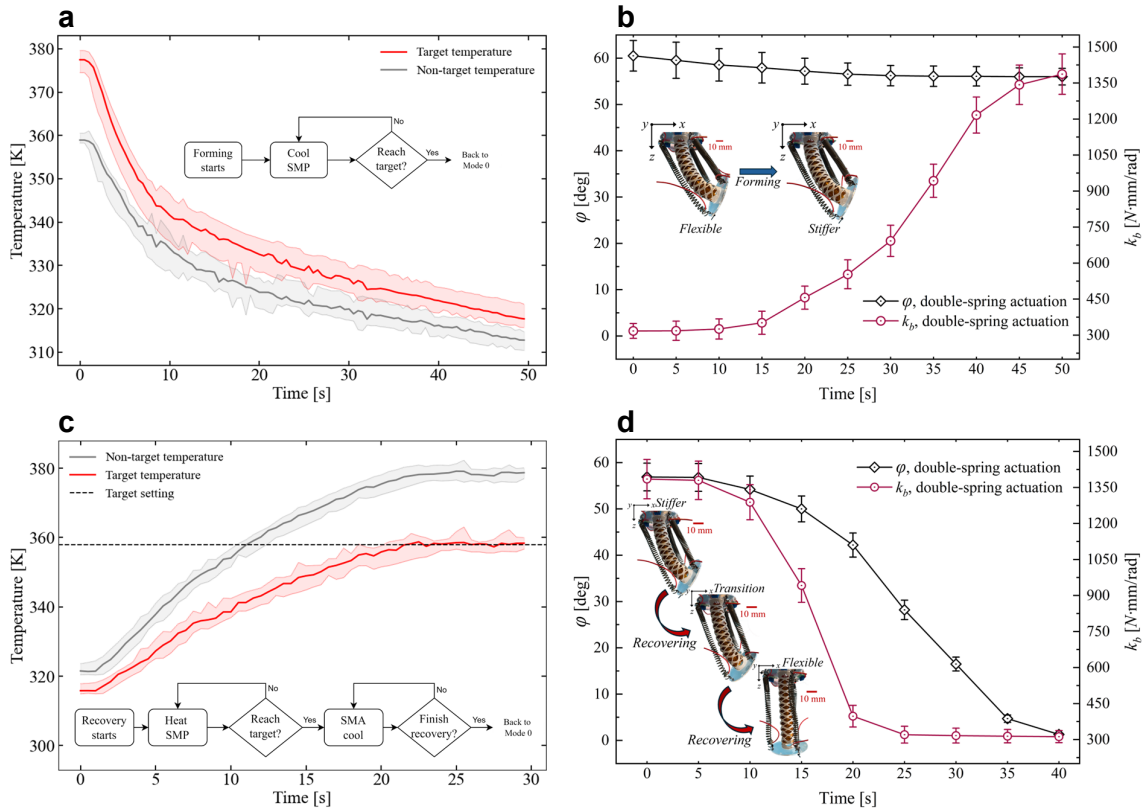


Figure 6.10. Workflow and performance of the building block in forming and recovering mode (a) Working flowchart and temperature distribution of forming mode (b) Bending performance and stiffness variation of forming mode (c) Working flowchart and temperature distribution of recovering mode (d) Bending performance and stiffness variation of recovering mode

6.5 Conclusion

In this chapter, a shape memory materials based morphing structure embedded with thermal control system is proposed that enables self-actuation, stiffness variation, and specified deforming modes.

An integrated system is developed by embedding a thermal control system into the SMA-SMP based morphing structure. The structure characterized by SMA springs and SMP frame achieves self-actuation and stiffness variation via the shape memory effects. In addition, the embedded thermal control system allows the SMA springs and SMP frame actuating comparatively by the temperature stimulus, enabling the morphing structure to execute multiple actions by consistent operation.

A numerical model integrating SMA springs with SMP structure was successfully developed. The simulation results closely matched the experimental data, verifying the feasibility of proposed morphing structure. Specifically, the structure achieved a maximum bending angle of 65° with double-spring actuation and 42° with single-spring actuation. By incorporating the MMTS method with a PID control algorithm, a comprehensive integration system was developed, capable of supporting multiple working modes to achieve diverse functionalities. In stepping mode, the system enabled precise step-by-step actuation, completing full loading within 30 seconds within four stepping steps of 6 seconds each and three pulsing steps of 2 seconds each.

The use of stepping mode enables the morphing structure to effectively transition between shapes by self-actuation, whether starting from its initial state or an existing configuration. The forming and recovery modes facilitated shape locking and recovery, with braking times of 50 and 40 seconds, respectively. In the locked state, the bending stiffness increased by up to 4.5 times. In addition, the recovery process exhibited a slight hysteresis, requiring approximately 15 seconds longer than the stiffness adjustment to fully restore the initial posture. The integration system improves the controllability and versatility of the morphing structure, providing valuable insights for developing mechanical intelligence with efficient self-actuation and reliable control.

However, the current control system cannot fully compensate for the target deformation. Our next step involves incorporating posture detection to achieve precise shaping of the morphing structure's deformation. Additionally, the current cooling actuators are inefficient, resulting in excessive braking time. Future work will focus on optimizing the morphing structure's design and integrating actuators with significantly improved cooling performance.

7 Conclusions and Recommendations

7.1 Conclusions

This thesis is aimed to develop a design framework on integrating mechanically intelligent morphing structures into soft robotics, addressing key challenges in adaptive performance and multiple functionalities. To achieve the adaptive performance, the morphing structures embedded with smart materials have been designed by the design framework. The morphing structures are constructed by the building blocks, which have been proposed as the smart unit enabling self-actuation. To develop multiple functionalities, an integration system was introduced to coordinate multiple smart materials within these building blocks, facilitating collaborative and tailored behaviors. The research questions formulated in Chapter 1 are addressed below.

Q1: What is the state-of-the-art of smart materials? How are they classified, what are their properties and how are they modeled?

Smart materials are classified based on how they react to external factors like temperature, light, pressure, electric fields, or magnetic fields. Smart materials show various properties stimulated by different stimuli. Hydrogels show the volume change actuated by temperature, pH, humidity, or chemical reactions. Shape memory materials can achieve the shape memory effect or stiffness variation by temperature change. Piezoelectric materials generate the electricity by external stress. Light, electric, and magnetic responded materials can change the shape by inner mechanical strain.

Modeling approaches offer solutions for understanding the properties of smart materials. Commonly used techniques include the finite element method (FEM), molecular dynamics (MD), and phase field modeling (PFM). FEM emphasizes macroscale analysis, MD operates at

the atomic to nanoscale level, and PFM focuses on the mesoscale. Among them, FEM is widely utilized for designing structures involving smart materials. A crucial aspect of FEM analysis for smart materials is selecting the appropriate constitutive models, mainly including thermally dependent viscoelastic or hyper/super-elastic models for shape memory materials, free energy models for hydrogels, and rheological models for electro/magneto-rheological fluids.

Q2: How can smart materials be applied into the development of a model-based design framework?

The concept of building blocks, which refers as the modular units, is induced to support the model-based design framework developing smart materials based structure. The building blocks are constructed by integrating the structural geometry, smart material, and external stimuli. Numerical methods, such as the finite element method (FEM) and the coupled method of finite element and discrete element method (FEM-DEM), and multibody dynamics (MBD) offer significant approaches to build model-based design framework.

In the design process, the building blocks function as responsive elements, adapting to the selected structures, materials, and external stimuli. During the implementation of the model-based design framework, these building blocks need to adapt to changing conditions, ensuring they continue to function under new requirements. The selected numerical methods serve as tools to evaluate the proposed building blocks. For instance, if the environmental change involves temperature variations, SMPs can be chosen as the material. In this case, the structural design of the building block would be tailored to agree with the specific properties of SMPs. Similarly, if humidity is a key environmental factor, hydrogels would be a suitable material choice, and the building block would be designed to satisfy the characteristics of hydrogels. By employing variable building blocks, it is possible to tailor the functions of these components to specific applications. Particle-based building blocks, for example, demonstrate substantial deformation capabilities and can increase stiffness. Temperature-sensitive hydrogels exhibit active deformation properties, making the building blocks suitable for applications such as elongation and grasping. A hybrid design combining SMP and smart hydrogel can further enhance these actuators by offering both active deformation and stiffness control, enabling functions such as grasping, installation, and maintenance while improving the adaptability of the modular building blocks.

Q3: How can the model-based design framework be utilized to design mechanically intelligent morphing structure?

A novel conceptual design of a particle-based soft building block through model-based design framework is proposed. First, the rigid-particle based actuator is proposed based on the particle jamming effect, which is characterized by a dual-deformable chamber structure filled with tailored particles. Then, a novel building block was proposed to explore the potential of smart hydrogel as actuating method on the soft grippers. The proposed soft gripper is characterized by flexible structure and temperature-sensitive smart hydrogel particles. The simulation results for both the rigid and hydrogel particle based designs are validated through experiments, confirming the feasibility of the model-based design framework.

In the design of rigid particle building block, the specific results have shown that both the shrinkage mode and expansion mode of the actuator can achieve the bending behaviors of different particle diameter ratios and different actuator lengths. In addition, the larger bending angle and more significant deflection can be achieved by increasing the particle diameter ratio, the actuator length, and the elastic modulus of the membrane.

In the design of smart hydrogel-based building block, increasing the number of particle layers is essential to improve the bending performance. Alternatively, the material of the structure could be made more flexible. Another option is to adjust the strain layer design to include specific shaped gaps. In addition, bending stiffness grows as the angle increases, but structures with gaps reduce stiffness, while rigidly covered membranes enhance it. Implementing variable stiffness strips significantly boosts bending stiffness, achieving a thirty-fold increase at most, demonstrating a relative improvement compared to other enhanced actuators.

The particle jamming effect, enabling the transition of the particles packing state, is an approach to achieving mechanical intelligence when integrated with novel designs. The effect enables a structure to transition between soft and rigid states, allowing for shape and stiffness changes. During the design process, the model-based design frameworks provide a frame for evaluating the verifications of these designs.

Q4: How can the morphing structure achieve self-actuation by integrating multiple smart materials?

The pH-sensitive hydrogel and shape memory polymer (SMP) are employed to create the morphing structures that enables self-actuation and stiffness variation. Self-actuation occurs through an increase in pH, while stiffness enhancement is achieved by lowering the temperature. The morphing structure is assembled by cylindrical building blocks which developed by model-based design. Each material contributes unique property, including shape change or stiffness variation. By integrating these properties through different stimuli, the actuation process can occur without the need for an external power source.

The development of tailored morphing structures capable of bending, curling, and elongation is achieved through the use of variable intelligent structures with diverse designs. The bending and curling configurations utilize multilayer hydrogel units within a SMP frame, while the elongation configuration comprises hydrogel units, an SMP frame, and connecting elements. Bending performance is assessed by the bending angle, which increases with the number of vertical layers and thickness differences, but decreases with the number of horizontal layers. Curling performance is measured by displacements in various directions, predominantly influenced by axial thickness differences and minimally by vertical thickness differences. Elongation performance is evaluated by the elongation ratio, which increases horizontally with both thickness differences and the number of layers, but decreases vertically with thickness differences.

Using SMP as the morphing structure frame effectively enables stiffness variation. In its rubbery state, the bending stiffness of the proposed structure is slightly higher than that of a pneumatic actuator. However, once the SMP transitions to its glassy state, the bending stiffness

increases tenfold compared to the rubbery state, exceeding particle-based, particle jamming, and fiber-reinforced actuators. The higher pH of seawater compared to air is ideal for actuating pH-sensitive hydrogels, and the waste heat generated during subsea operations can effectively drive SMPs. This makes the proposed structure highly suitable for underwater applications and subsea operations, supporting various morphing structures.

Q5: How to develop an integrated system with multiple smart materials to respond collaboratively to the same stimulus, enabling multifunctionality for mechanical intelligence?

An integrated system is developed by embedding a thermal control system into the SMA-SMP based morphing structure. The structure characterized by SMA springs and SMP frame achieves self-actuation and stiffness variation via the shape memory effects. In addition, the embedded thermal control system allows the SMA springs and SMP frame actuating comparatively by the temperature stimulus, enabling the morphing structure to execute multiple actions by consistent operation.

Specifically, the structure achieved a maximum bending angle of 65° with double-spring actuation and 42° with single-spring actuation. In addition, by incorporating the MMTS method with a PID control algorithm, a comprehensive thermal control system was developed, capable of supporting multiple working modes to achieve diverse functionalities. In stepping mode, the system enabled precise step-by-step actuation, completing full loading within 30 seconds within four stepping steps of 6 seconds each and three pulsing steps of 2 seconds each. The use of stepping mode enables the morphing structure to effectively transition between shapes by self-actuation, whether starting from its initial state or an existing configuration. The forming and recovery modes facilitated shape locking and recovery, with braking times of 50 and 40 seconds, respectively. In the locked state, the bending stiffness increased by up to 4.5 times. The integration system improves the controllability and versatility of the morphing structure, providing valuable insights for developing mechanical intelligence with efficient self-actuation and reliable control.

7.2 Recommendations

Developing the integrated mechanical intelligence within smart morphing structures on model-based design framework is the main focus of this thesis. To bring the designs effectively applied into industries, further research is needed to consider accuracy, stability, and reliability.

1. Time-dependent numerical models for smart materials

Time-dependent numerical models are crucial for analyzing and predicting the behavior of smart materials more accurate. Existing simulation models primarily offer static descriptions of material states, where the response is based on external stimuli without accounting for time dependencies. However, in practical applications, the influence of time on performance efficiency must be considered. For instance, in situations requiring rapid response times (on the order of seconds), using hydrogel as an actuating material may not be suitable. Currently, numerical models lack the ability to assess time-sensitive factors. Therefore, it is essential to

develop time-dependent numerical models to accurately predict the deformation of smart material-based morphing structures, particularly in applications that demand quick response times.

2. Dynamic control for stability of mechanical intelligence

Develop a robust and adaptive control system that quickly responds to external stimuli. This system enables mechanically intelligent soft robots to manage real-time responses in dynamic and uncertain environments. While current control algorithm is based on the transitions of steady states, future work could enhance dynamic control by integrating machine learning algorithms to add the feedback system. The dynamic control system enables real-time monitoring and feedback of the structure, providing early warnings of potential risks to improve the stability. Such stable systems are crucial for scaling soft robotics applications in industrial settings where conditions fluctuate rapidly, such as dangerous material handling or field-based inspections in maritime or offshore engineering.

3. Fatigue analysis for improved durability and reliability

Conduct extensive fatigue analysis on the smart materials and morphing structures to assess their performance and lifetime in continuous or repetitive industrial applications. This could predict how these materials and structures degrade over time, especially under varying load conditions. For instance, in repetitive pick-and-place operations, materials subject to constant deformation may experience fatigue, requiring replacement or reconfiguration. State-of-the-art structural health monitoring and maintenance strategies could help to achieve smart materials embedded systems to operate reliably for longer periods, especially important for high-demand manufacturing and automation.

Implementing these recommendations will enhance the model-based design framework and its smart morphing structures by improving dynamic control and enabling comprehensive fatigue analysis. These advancements will prepare structures designed with the framework for industrial applications by increasing their scalability. Additionally, future research in these areas will support the development of versatile and durable soft robotic systems capable of long-term operation, making them a practical solution for various industries.

Bibliography

- [1] A. Billard, and D. Kragic, “Trends and challenges in robot manipulation,” *Science*, vol. 364, no. 6446, pp. eaat8414, 2019.
- [2] D. Rus, and M. T. Tolley, “Design, fabrication and control of soft robots,” *Nature*, vol. 521, no. 7553, pp. 467-475, 2015.
- [3] S. Aracri, J. Hughes, C. Della Santina, J. Jovanova, S. Hoh, D. S. Garcia Morales, R. Barcaro, Y. J. Tan, V. G. Kortman, and A. Sakes, “Soft Robotics: A Route to Equality, Diversity, and Inclusivity in Robotics,” *Soft Robotics*, 2024.
- [4] C. Lee, M. Kim, Y. J. Kim, N. Hong, S. Ryu, H. J. Kim, and S. Kim, “Soft robot review,” *International Journal of Control, Automation and Systems*, vol. 15, pp. 3-15, 2017.
- [5] E. Roels, S. Terryn, F. Iida, A. W. Bosman, S. Norvez, F. Clemens, G. Van Assche, B. Vanderborght, and J. Brancart, “Processing of self-healing polymers for soft robotics,” *Advanced Materials*, vol. 34, no. 1, pp. 2104798, 2022.
- [6] E. Brown, N. Rodenberg, J. Amend, A. Mozeika, E. Steltz, M. R. Zakin, H. Lipson, and H. M. Jaeger, “Universal robotic gripper based on the jamming of granular material,” *Proceedings of the National Academy of Sciences*, vol. 107, no. 44, pp. 18809-18814, 2010.
- [7] A. Lotfiani, H. Zhao, Z. Shao, and X. Yi, “Torsional stiffness improvement of a soft pneumatic finger using embedded skeleton,” *Journal of Mechanisms and Robotics*, vol. 12, no. 1, pp. 011016, 2020.
- [8] Y. Zhang, P. Li, J. Quan, L. Li, G. Zhang, and D. Zhou, “Progress, challenges, and prospects of soft robotics for space applications,” *Advanced Intelligent Systems*, vol. 5, no. 3, pp. 2200071, 2023.
- [9] L. C. Zhao, H. X. Zou, K. X. Wei, S. X. Zhou, G. Meng, and W. M. Zhang, “Mechanical intelligent energy harvesting: from methodology to applications,” *Advanced Energy Materials*, vol. 13, no. 29, pp. 2300557, 2023.
- [10] A. Khaheshi, and H. Rajabi, “Mechanical intelligence (mi): A bioinspired concept for transforming engineering design,” *Advanced Science*, vol. 9, no. 32, pp. 2203783, 2022.

- [11] T. Wang, C. Pierce, V. Kojouharov, B. Chong, K. Diaz, H. Lu, and D. I. Goldman, "Mechanical intelligence simplifies control in terrestrial limbless locomotion," *Science Robotics*, vol. 8, no. 85, pp. eadi2243, 2023.
- [12] V. G. Kortman, B. Mazzolai, A. Sakes, and J. Jovanova, "Perspectives on intelligence in soft robotics," *Advanced Intelligent Systems*, pp. 2400294, 2024.
- [13] S. Kim, C. Laschi, and B. Trimmer, "Soft robotics: a bioinspired evolution in robotics," *Trends in biotechnology*, vol. 31, no. 5, pp. 287-294, 2013.
- [14] J. Sun, E. Lerner, B. Tighe, C. Middlemist, and J. Zhao, "Embedded shape morphing for morphologically adaptive robots," *Nature Communications*, vol. 14, no. 1, pp. 6023, 2023.
- [15] D. Hwang, E. J. Barron III, A. T. Haque, and M. D. Bartlett, "Shape morphing mechanical metamaterials through reversible plasticity," *Science robotics*, vol. 7, no. 63, pp. eabg2171, 2022.
- [16] A. Iannarelli, M. Ghaffarian Niasar, and R. Ross, "Frequency-independent breakdown strength of dielectric elastomers under AC stress," *Applied Physics Letters*, vol. 115, no. 9, 2019.
- [17] S. Liang, Y. Tu, Q. Chen, W. Jia, W. Wang, and L. Zhang, "Microscopic hollow hydrogel springs, necklaces and ladders: a tubular robot as a potential vascular scavenger," *Materials Horizons*, vol. 6, no. 10, pp. 2135-2142, 2019.
- [18] Q. Ge, A. H. Sakhaei, H. Lee, C. K. Dunn, N. X. Fang, and M. L. Dunn, "Multimaterial 4D printing with tailorable shape memory polymers," *Scientific reports*, vol. 6, no. 1, pp. 31110, 2016.
- [19] B. R. Donovan, V. M. Matavulj, S. k. Ahn, T. Guin, and T. J. White, "All-optical control of shape," *Advanced Materials*, vol. 31, no. 2, pp. 1805750, 2019.
- [20] Q. Ze, X. Kuang, S. Wu, J. Wong, S. M. Montgomery, R. Zhang, J. M. Kovitz, F. Yang, H. J. Qi, and R. Zhao, "Magnetic shape memory polymers with integrated multifunctional shape manipulation," *Advanced Materials*, vol. 32, no. 4, pp. 1906657, 2020.
- [21] R. Wang, Y. Guan, H. Song, X. Li, X. Li, Z. Shi, and X. Song, "A formal model-based design method for robotic systems," *IEEE Systems Journal*, vol. 13, no. 1, pp. 1096-1107, 2018.
- [22] S. K. Rout, M. R. Bisram, and J. Cao, "Methods for numerical simulation of knit based morphable structures: knitmorphs," *Scientific reports*, vol. 12, no. 1, pp. 6630, 2022.
- [23] S. Wang, and J. C. Brigham, "A computational framework for the optimal design of morphing processes in locally activated smart material structures," *Smart Materials and Structures*, vol. 21, no. 10, pp. 105016, 2012.
- [24] S. Bahl, H. Nagar, I. Singh, and S. Sehgal, "Smart materials types, properties and applications: A review," *Materials Today: Proceedings*, vol. 28, pp. 1302-1306, 2020.
- [25] A. A. Basheer, "Advances in the smart materials applications in the aerospace industries," *Aircraft Engineering and Aerospace Technology*, vol. 92, no. 7, pp. 1027-1035, 2020.
- [26] M. Ammar, A. Haleem, M. Javaid, S. Bahl, S. B. Garg, A. Shamoan, and J. Garg, "Significant applications of smart materials and Internet of Things (IoT) in the automotive industry," *Materials Today: Proceedings*, vol. 68, pp. 1542-1549, 2022.
- [27] K. A. Hoffmann, T. G. Chen, M. R. Cutkosky, and D. Lentink, "Bird-inspired robotics principles as a framework for developing smart aerospace materials," *Journal of Composite Materials*, vol. 57, no. 4, pp. 679-710, 2023.
- [28] M. Su, and Y. Song, "Printable smart materials and devices: strategies and applications," *Chemical reviews*, vol. 122, no. 5, pp. 5144-5164, 2021.

- [29] J. F. McCabe, Z. Yan, O. Al Naimi, G. Mahmoud, and S. Rolland, "Smart materials in dentistry," *Australian dental journal*, vol. 56, pp. 3-10, 2011.
- [30] H. M. El-Husseiny, E. A. Mady, L. Hamabe, A. Abugomaa, K. Shimada, T. Yoshida, T. Tanaka, A. Yokoi, M. Elbadawy, and R. Tanaka, "Smart/stimuli-responsive hydrogels: Cutting-edge platforms for tissue engineering and other biomedical applications," *Materials Today Bio*, vol. 13, pp. 100186, 2022.
- [31] J. Jones, "Towards programmable smart materials: Dynamical reconfiguration of emergent transport networks," *Int. J. Unconv. Comput.*, vol. 7, no. 6, pp. 423-447, 2011.
- [32] I. N. Qader, K. Mediha, F. Dagdelen, and Y. Aydoğdu, "A review of smart materials: researches and applications," *El-Cezeri*, vol. 6, no. 3, pp. 755-788, 2019.
- [33] M. A. Ward, and T. K. Georgiou, "Thermoresponsive polymers for biomedical applications," *Polymers*, vol. 3, no. 3, pp. 1215-1242, 2011.
- [34] M. Mrinalini, and S. Prasanthkumar, "Recent advances on stimuli-responsive smart materials and their applications," *ChemPlusChem*, vol. 84, no. 8, pp. 1103-1121, 2019.
- [35] H. Tzou, H.-J. Lee, and S. Arnold, "Smart materials, precision sensors/actuators, smart structures, and structronic systems," *Mechanics of Advanced Materials and Structures*, vol. 11, no. 4-5, pp. 367-393, 2004.
- [36] J. Ahn, J. Gu, J. Choi, C. Han, Y. Jeong, J. Park, S. Cho, Y. S. Oh, J. H. Jeong, and M. Amjadi, "A Review of Recent Advances in Electrically Driven Polymer-Based Flexible Actuators: Smart Materials, Structures, and Their Applications," *Advanced Materials Technologies*, vol. 7, no. 11, pp. 2200041, 2022.
- [37] M. J. Hawkins, P. Soon-Shiong, and N. Desai, "Protein nanoparticles as drug carriers in clinical medicine," *Advanced drug delivery reviews*, vol. 60, no. 8, pp. 876-885, 2008.
- [38] Y. Yin, and J. A. Rogers, "Introduction: smart materials," 5, ACS Publications, 2022, pp. 4885-4886.
- [39] M. Yildirim, and Z. Candan, "Smart materials: The next generation in science and engineering," *Materials Today: Proceedings*, 2023.
- [40] H. C. Kim, S. Mun, H.-U. Ko, L. Zhai, A. Kafy, and J. Kim, "Renewable smart materials," *Smart Materials and Structures*, vol. 25, no. 7, pp. 073001, 2016.
- [41] M. F. Ashby, H. Shercliff, and D. Cebon, *Materials: engineering, science, processing and design*: Butterworth-Heinemann, 2018.
- [42] F. P. Morais, and J. M. Curto, "Challenges in computational materials modelling and simulation: A case-study to predict tissue paper properties," *Heliyon*, vol. 8, no. 5, 2022.
- [43] J. Merodio, and R. W. Ogden, "Constitutive modelling of solid continua," 2020.
- [44] Q. Guo, W. Yao, W. Li, and N. Gupta, "Constitutive models for the structural analysis of composite materials for the finite element analysis: A review of recent practices," *Composite Structures*, vol. 260, pp. 113267, 2021.
- [45] M. Enyan, Z. Bing, J. N. O. Amu-Darko, E. Issaka, S. L. Otoo, and M. F. Agyemang, "Advances in smart materials soft actuators on mechanisms, fabrication, materials, and multifaceted applications: A review," *Journal of Thermoplastic Composite Materials*, pp. 08927057241248028, 2024.
- [46] B. Sun, "Smart materials and structures," *South Africa: Cape Town: Cape Peninsula University of Technology Lecture at Swiss Federal Institute of Technology Zurich (ETH)*, 2015.
- [47] A. Mukherjee, P. Srivastava, and J. K. Sandhu, "Application of smart materials in civil engineering: A review," *Materials Today: Proceedings*, vol. 81, pp. 350-359, 2023.

- [48] N. Jain, S. N. Ovhal, V. Patil, and K. N. Kartik, "Smart materials—A state-of-the-art-review," *Materials Today: Proceedings*, vol. 82, pp. 381-389, 2023.
- [49] P. Yang, F. Zhu, Z. Zhang, Y. Cheng, Z. Wang, and Y. Li, "Stimuli-responsive polydopamine-based smart materials," *Chemical Society Reviews*, vol. 50, no. 14, pp. 8319-8343, 2021.
- [50] S. Kamila, "Introduction, classification and applications of smart materials: an overview," *American Journal of Applied Sciences*, vol. 10, no. 8, pp. 876, 2013.
- [51] A. Behera, and A. Behera, "Piezoelectric materials," *Advanced Materials: An Introduction to Modern Materials Science*, pp. 43-76, 2022.
- [52] Y. Meng, G. Chen, and M. Huang, "Piezoelectric materials: Properties, advancements, and design strategies for high-temperature applications," *Nanomaterials*, vol. 12, no. 7, pp. 1171, 2022.
- [53] C. Boerkamp, T. L. Costa, and J. Jovanova, "Design of a Flexible Transducer Array and Characterisation of Piezoelectric Sensors for Curvature Compensation." p. V001T08A002.
- [54] H. Kulkarni, K. Zohaib, A. Khusru, and K. S. Aiyappa, "Application of piezoelectric technology in automotive systems," *Materials Today: Proceedings*, vol. 5, no. 10, pp. 21299-21304, 2018.
- [55] A. K. Mishra, V. J. K. Priya, K. Pradeep, J. S. Vaishnav, and G. Kabhilesh, "Smart materials for ultrasonic piezoelectric composite transducer: A short review," *Materials Today: Proceedings*, vol. 62, pp. 2064-2069, 2022.
- [56] Y. Wu, Y. Ma, H. Zheng, and S. Ramakrishna, "Piezoelectric materials for flexible and wearable electronics: A review," *Materials & Design*, vol. 211, pp. 110164, 2021.
- [57] M. C. Sekhar, E. Veena, N. S. Kumar, K. C. B. Naidu, A. Mallikarjuna, and D. B. Basha, "A review on piezoelectric materials and their applications," *Crystal Research and Technology*, vol. 58, no. 2, pp. 2200130, 2023.
- [58] M. Habib, I. Lantgios, and K. Hornbostel, "A review of ceramic, polymer and composite piezoelectric materials," *Journal of Physics D: Applied Physics*, vol. 55, no. 42, pp. 423002, 2022.
- [59] H. Shih, D. Rushon, H. Tzou, W. Zheng, and K. Uchino, "Photostriction and its use in actuation of flexible structures," *Journal of Engineering Technology*, vol. 25, no. 1, pp. 20, 2008.
- [60] B. Kundys, "Photostrictive materials," *Applied Physics Reviews*, vol. 2, no. 1, 2015.
- [61] Z. Song, Z. Zhang, Y. Yu, and D. Lin, "Photostriction effect and electric properties of La-doped PMN-PT transparent ferroelectric ceramics," *International Journal of Smart and Nano Materials*, vol. 15, no. 2, pp. 296-311, 2024.
- [62] M. Rahman, "Experimental investigation of photostrictive materials for MEMS application," *Open Access Library Journal*, vol. 4, no. 11, pp. 1, 2017.
- [63] H. Zhang, and N.-G. Park, "Polarons in perovskite solar cells: effects on photovoltaic performance and stability," *Journal of Physics: Energy*, vol. 5, no. 2, pp. 024002, 2023.
- [64] S. Zhao, Y. Zhang, S. Kitipornchai, and J. Yang, "Opto-electro-thermo-mechanical behaviours of perovskite plates," *International Journal of Mechanical Sciences*, vol. 267, pp. 109016, 2024.
- [65] C. Chen, and Z. Yi, "Photostrictive effect: characterization techniques, materials, and applications," *Advanced Functional Materials*, vol. 31, no. 22, pp. 2010706, 2021.
- [66] M. Shahinpoor, "Review of Electrostrictive Materials," 2020.
- [67] Y. Shkel, "Electrostriction: material parameters and stress/strain constitutive relations," *Philosophical Magazine*, vol. 87, no. 11, pp. 1743-1767, 2007.

- [68] G. Bocchetta, G. Fiori, S. A. Sciuto, and A. Scorza, "Performance of smart materials-based instrumentation for force measurements in biomedical applications: A methodological review." p. 261.
- [69] M. Sobczyk, S. Wiesenhütter, J. R. Noennig, and T. Wallmersperger, "Smart materials in architecture for actuator and sensor applications: A review," *Journal of Intelligent Material Systems and Structures*, vol. 33, no. 3, pp. 379-399, 2022.
- [70] V. Mouet, B. Apffel, and E. Fort, "Comprehensive refractive manipulation of water waves using electrostriction," *Proceedings of the National Academy of Sciences*, vol. 120, no. 6, pp. e2216828120, 2023.
- [71] N. Bassiri-Gharb, S. Trolier-McKinstry, and D. Damjanovic, "Strain-modulated piezoelectric and electrostrictive nonlinearity in ferroelectric thin films without active ferroelastic domain walls," *Journal of Applied Physics*, vol. 110, no. 12, 2011.
- [72] Z. Hou, R. Xiong, H. Wu, Z. Wang, B. Su, R. Su, X. Long, and C. He, "Ultralow Hysteresis and a Giant Electrostrictive Coefficient in Pb (Mg_{1/3}Nb_{2/3}) O₃-Based Ferroelectric Crystals," *Crystal Growth & Design*, 2024.
- [73] A.-G. Olabi, and A. Grunwald, "Design and application of magnetostrictive materials," *Materials & Design*, vol. 29, no. 2, pp. 469-483, 2008.
- [74] C.-h. Lin, and Y.-Z. Lin, "Analysis of nonlinear piezomagnetism for magnetostrictive terfenol-D composites," *Journal of Magnetism and Magnetic Materials*, vol. 540, pp. 168490, 2021.
- [75] Z. Liu, W. Liu, P. Wang, Z. Li, Y. Xu, X. Yang, and F. Shu, "High-precision position tracking control of giant magnetostrictive actuators using fractional-order sliding mode control with inverse prandtl-ishlinskii compensator," *International Journal of Precision Engineering and Manufacturing*, vol. 24, no. 3, pp. 379-393, 2023.
- [76] A. Behera, *Advanced materials: an introduction to modern materials science*: Springer Nature, 2021.
- [77] C. Gao, Z. Zeng, S. Peng, and C. Shuai, "Magnetostrictive alloys: Promising materials for biomedical applications," *Bioactive Materials*, vol. 8, pp. 177, 2022.
- [78] B. Li, T. Zhang, C. Jiang, and J. Gu, "Low eddy current loss of Terfenol-D/epoxy particulate magnetostrictive composites prepared using the particle phosphatizing treatment method," *Journal of Magnetism and Magnetic Materials*, vol. 508, pp. 166869, 2020.
- [79] L. Chen, R. Liu, and X. Shi, *Thermoelectric materials and devices*: Elsevier, 2020.
- [80] M. Mukherjee, A. Srivastava, and A. K. Singh, "Recent advances in designing thermoelectric materials," *Journal of Materials Chemistry C*, vol. 10, no. 35, pp. 12524-12555, 2022.
- [81] P. K. Singh, V. Rao, and D. Dwivedi, "Recent trend and future prospectus of smart and composite materials: A Review," *Amorphous Semiconductor Research Laboratory*, 2015.
- [82] L. Yang, Z. G. Chen, M. S. Dargusch, and J. Zou, "High performance thermoelectric materials: progress and their applications," *Advanced Energy Materials*, vol. 8, no. 6, pp. 1701797, 2018.
- [83] M. d'Angelo, C. Galassi, and N. Lecis, "Thermoelectric Materials and Applications: A Review," *Energies*, vol. 16, no. 17, pp. 6409, 2023.
- [84] A. E. Shalan, N. Peřinka, E. S. A. Serea, and M. F. Sanad, "Advances in thermochromic and thermoelectric materials," *Advanced Lightweight Multifunctional Materials*, pp. 153-186: Elsevier, 2021.
- [85] Z. Soleimani, S. Zoras, B. Ceranic, S. Shahzad, and Y. Cui, "A review on recent developments of thermoelectric materials for room-temperature applications," *Sustainable Energy Technologies and Assessments*, vol. 37, pp. 100604, 2020.

- [86] M. Očko, S. Žonja, and M. Ivanda, "Thermoelectric materials: problems and perspectives." pp. 16-21.
- [87] C. Gu, A.-B. Jia, Y.-M. Zhang, and S. X.-A. Zhang, "Emerging electrochromic materials and devices for future displays," *Chemical Reviews*, vol. 122, no. 18, pp. 14679-14721, 2022.
- [88] R. J. Mortimer, "Electrochromic materials," *Annual review of materials research*, vol. 41, no. 1, pp. 241-268, 2011.
- [89] J. Niu, Y. Wang, X. Zou, Y. Tan, C. Jia, X. Weng, and L. Deng, "Infrared electrochromic materials, devices and applications," *Applied Materials Today*, vol. 24, pp. 101073, 2021.
- [90] H. Fu, L. Zhang, Y. Dong, C. Zhang, and W. Li, "Recent advances in electrochromic materials and devices for camouflage applications," *Materials Chemistry Frontiers*, vol. 7, no. 12, pp. 2337-2358, 2023.
- [91] V. Rai, R. S. Singh, D. J. Blackwood, and D. Zhili, "A review on recent advances in electrochromic devices: a material approach," *Advanced Engineering Materials*, vol. 22, no. 8, pp. 2000082, 2020.
- [92] A. V. Shchegolkov, S.-H. Jang, A. V. Shchegolkov, Y. V. Rodionov, A. O. Sukhova, and M. S. Lipkin, "A brief overview of electrochromic materials and related devices: A nanostructured materials perspective," *Nanomaterials*, vol. 11, no. 9, pp. 2376, 2021.
- [93] R. Kumar, D. K. Pathak, and A. Chaudhary, "Current status of some electrochromic materials and devices: a brief review," *Journal of Physics D: Applied Physics*, vol. 54, no. 50, pp. 503002, 2021.
- [94] Y. Huang, B. Wang, F. Chen, Y. Han, W. Zhang, X. Wu, R. Li, Q. Jiang, X. Jia, and R. Zhang, "Electrochromic materials based on ions insertion and extraction," *Advanced Optical Materials*, vol. 10, no. 4, pp. 2101783, 2022.
- [95] H. Tian, and J. Zhang, *Photochromic materials: preparation, properties and applications*: John Wiley & Sons, 2016.
- [96] Y. Ke, J. Chen, G. Lin, S. Wang, Y. Zhou, J. Yin, P. S. Lee, and Y. Long, "Smart windows: electro-, thermo-, mechano-, photochromics, and beyond," *Advanced Energy Materials*, vol. 9, no. 39, pp. 1902066, 2019.
- [97] M. Irie, T. Seki, and Y. Yokoyama, *New frontiers in photochromism*: Springer, 2013.
- [98] A. L. Leistner, and Z. L. Pianowski, "Smart photochromic materials triggered with visible light," *European Journal of Organic Chemistry*, vol. 2022, no. 19, pp. e202101271, 2022.
- [99] J. Zhang, Q. Zou, and H. Tian, "Photochromic materials: more than meets the eye," *Advanced Materials*, vol. 25, no. 3, pp. 378-399, 2013.
- [100] Y. Ru, Z. Shi, J. Zhang, J. Wang, B. Chen, R. Huang, G. Liu, and T. Yu, "Recent progress of photochromic materials towards photocontrollable devices," *Materials Chemistry Frontiers*, vol. 5, no. 21, pp. 7737-7758, 2021.
- [101] B. Zhang, Y. Xie, J. Zhou, K. Wang, and Z. Zhang, "State-of-the-art robotic grippers, grasping and control strategies, as well as their applications in agricultural robots: A review," *Computers and Electronics in Agriculture*, vol. 177, pp. 105694, 2020.
- [102] C. Löwenberg, M. Balk, C. Wischke, M. Behl, and A. Lendlein, "Shape-memory hydrogels: evolution of structural principles to enable shape switching of hydrophilic polymer networks," *Accounts of chemical research*, vol. 50, no. 4, pp. 723-732, 2017.
- [103] S. Cai, and Z. Suo, "Mechanics and chemical thermodynamics of phase transition in temperature-sensitive hydrogels," *Journal of the Mechanics and Physics of Solids*, vol. 59, no. 11, pp. 2259-2278, 2011.

- [104] L. Li, J. M. Scheiger, and P. A. Levkin, "Design and applications of photoresponsive hydrogels," *Advanced Materials*, vol. 31, no. 26, pp. 1807333, 2019.
- [105] T. Dutta, P. Chaturvedi, I. Llamas-Garro, J. S. Velázquez-González, R. Dubey, and S. K. Mishra, "Smart materials for flexible electronics and devices: hydrogel," *RSC advances*, vol. 14, no. 19, pp. 12984-13004, 2024.
- [106] B. Tian, and J. Liu, "Smart stimuli-responsive chitosan hydrogel for drug delivery: A review," *International Journal of Biological Macromolecules*, vol. 235, pp. 123902, 2023.
- [107] Y. Liang, J. He, and B. Guo, "Functional hydrogels as wound dressing to enhance wound healing," *ACS nano*, vol. 15, no. 8, pp. 12687-12722, 2021.
- [108] Y. Chen, Y. Zhang, H. Li, J. Shen, F. Zhang, J. He, J. Lin, B. Wang, S. Niu, and Z. Han, "Bioinspired hydrogel actuator for soft robotics: Opportunity and challenges," *Nano Today*, vol. 49, pp. 101764, 2023.
- [109] Q. Chen, D. Schott, and J. Jovanova, "Model-Based Design of Variable Stiffness Soft Gripper Actuated by Smart Hydrogels," *Soft Robotics*, 2024.
- [110] J. Zhang, W. Huang, H. Lu, and L. Sun, "Thermo-/chemo-responsive shape memory/change effect in a hydrogel and its composites," *Materials & Design*, vol. 53, pp. 1077-1088, 2014.
- [111] B. Xue, J. Gu, L. Li, W. Yu, S. Yin, M. Qin, Q. Jiang, W. Wang, and Y. Cao, "Hydrogel tapes for fault-tolerant strong wet adhesion," *Nature Communications*, vol. 12, no. 1, pp. 7156, 2021.
- [112] P. Kaur, R. Agrawal, F. M. Pfeffer, R. Williams, and H. B. Bohidar, "Hydrogels in agriculture: Prospects and challenges," *Journal of Polymers and the Environment*, vol. 31, no. 9, pp. 3701-3718, 2023.
- [113] P. Sikdar, M. M. Uddin, T. M. Dip, S. Islam, M. S. Hoque, A. K. Dhar, and S. Wu, "Recent advances in the synthesis of smart hydrogels," *Materials Advances*, vol. 2, no. 14, pp. 4532-4573, 2021.
- [114] A. M. Qazi, S. H. Mahmood, A. Haleem, S. Bahl, M. Javaid, and K. Gopal, "The impact of smart materials, digital twins (DTs) and Internet of things (IoT) in an industry 4.0 integrated automation industry," *Materials Today: Proceedings*, vol. 62, pp. 18-25, 2022.
- [115] I. Abavisani, O. Rezaifar, and A. Kheyroddin, "Multifunctional properties of shape memory materials in civil engineering applications: A state-of-the-art review," *Journal of Building Engineering*, vol. 44, pp. 102657, 2021.
- [116] K. Otsuka, and C. M. Wayman, *Shape memory materials*: Cambridge university press, 1999.
- [117] J. M. Jani, M. Leary, A. Subic, and M. A. Gibson, "A review of shape memory alloy research, applications and opportunities," *Materials & Design (1980-2015)*, vol. 56, pp. 1078-1113, 2014.
- [118] A. Spaggiari, D. Castagnetti, N. Golinelli, E. Dragoni, and G. Scirè Mammano, "Smart materials: Properties, design and mechatronic applications," *Proceedings of the institution of mechanical engineers, part l: journal of materials: design and applications*, vol. 233, no. 4, pp. 734-762, 2019.
- [119] C. Wayman, "Shape memory alloys," *MRS bulletin*, vol. 18, no. 4, pp. 49-56, 1993.
- [120] S. A. Raza, M. I. Khan, M. Ahmad, D. Tahir, A. Iltaf, and R. B. Naqvi, "Effect of nano-silica volume reinforcement on the microstructure, mechanical, phase distribution and electrochemical behavior of pre-alloyed titanium-nickel (Ti-Ni) powder," *Key Engineering Materials*, vol. 875, pp. 60-69, 2021.

- [121] A. Riccio, A. Sellitto, S. Ameduri, A. Concilio, and M. Arena, "Shape memory alloys (SMA) for automotive applications and challenges," *Shape Memory Alloy Engineering*, pp. 785-808, 2021.
- [122] J. W. Sohn, J. S. Ruth, D.-G. Yuk, and S.-B. Choi, "Application of Shape Memory Alloy Actuators to Vibration and Motion Control of Structural Systems: A Review," *Applied Sciences*, vol. 13, no. 2, pp. 995, 2023.
- [123] L. Matuszewski, "Application of shape memory alloys in pipeline couplings for shipbuilding," *Polish Maritime Research*, vol. 27, no. 3, pp. 82-88, 2020.
- [124] G. S. Rajput, J. Vora, P. Prajapati, and R. Chaudhari, "Areas of recent developments for shape memory alloy: A review," *Materials Today: Proceedings*, vol. 62, pp. 7194-7198, 2022.
- [125] M. Balasubramanian, R. Srimath, L. Vignesh, and S. Rajesh, "Application of shape memory alloys in engineering—A review." p. 012078.
- [126] L. Cao, L. Wang, C. Zhou, X. Hu, L. Fang, Y. Ni, C. Lu, and Z. Xu, "Surface Structures, Particles, and Fibers of Shape-Memory Polymers at Micro-/Nanoscale," *Advances in Polymer Technology*, vol. 2020, no. 1, pp. 7639724, 2020.
- [127] T. Dayyoub, A. V. Maksimkin, O. V. Filippova, V. V. Tcherdyntsev, and D. V. Telyshev, "Shape memory polymers as smart materials: a review," *Polymers*, vol. 14, no. 17, pp. 3511, 2022.
- [128] Y. Xia, Y. He, F. Zhang, Y. Liu, and J. Leng, "A review of shape memory polymers and composites: mechanisms, materials, and applications," *Advanced materials*, vol. 33, no. 6, pp. 2000713, 2021.
- [129] G. J. Berg, M. K. McBride, C. Wang, and C. N. Bowman, "New directions in the chemistry of shape memory polymers," *Polymer*, vol. 55, no. 23, pp. 5849-5872, 2014.
- [130] T. Mu, L. Liu, X. Lan, Y. Liu, and J. Leng, "Shape memory polymers for composites," *Composites Science and Technology*, vol. 160, pp. 169-198, 2018.
- [131] Y. Liu, H. Du, L. Liu, and J. Leng, "Shape memory polymers and their composites in aerospace applications: a review," *Smart materials and structures*, vol. 23, no. 2, pp. 023001, 2014.
- [132] H. Gao, J. Li, F. Zhang, Y. Liu, and J. Leng, "The research status and challenges of shape memory polymer-based flexible electronics," *Materials Horizons*, vol. 6, no. 5, pp. 931-944, 2019.
- [133] D. Rahmatabadi, K. Soltanmohammadi, M. Pahlavani, M. Aberoumand, E. Soleyman, I. Ghasemi, M. Baniassadi, K. Abrinia, M. Bodaghi, and M. Baghani, "Shape memory performance assessment of FDM 3D printed PLA-TPU composites by Box-Behnken response surface methodology," *The International Journal of Advanced Manufacturing Technology*, vol. 127, no. 1, pp. 935-950, 2023.
- [134] M. A. Kouka, F. Abbassi, M. Habibi, F. Chabert, A. Zghal, and C. Garnier, "4D printing of shape memory polymers, blends, and composites and their advanced applications: a comprehensive literature review," *Advanced Engineering Materials*, vol. 25, no. 4, pp. 2200650, 2023.
- [135] F. Momeni, X. Liu, and J. Ni, "A review of 4D printing," *Materials & design*, vol. 122, pp. 42-79, 2017.
- [136] M. Aberoumand, K. Soltanmohammadi, D. Rahmatabadi, E. Soleyman, I. Ghasemi, M. Baniassadi, K. Abrinia, M. Bodaghi, and M. Baghani, "4D printing of polyvinyl chloride (PVC): a detailed analysis of microstructure, programming, and shape memory performance," *Macromolecular Materials and Engineering*, vol. 308, no. 7, pp. 2200677, 2023.

- [137] R. Noroozi, A. Zolfagharian, M. Fotouhi, and M. Bodaghi, "4D-printed shape memory polymer: Modeling and fabrication," *Smart materials in additive manufacturing*, pp. 195-228: Elsevier, 2022.
- [138] A. Kantaros, T. Ganetsos, and D. Piromalis, "4D Printing: Technology Overview and Smart Materials Utilized," *Kantaros, A., Ganetsos, T. & Piromalis, D.(2023). 4D Printing: Technology Overview and Smart Materials Utilized. Journal of Mechatronics and Robotics*, vol. 7, no. 1, pp. 1-14, 2023.
- [139] C. A. Spiegel, M. Hackner, V. P. Bothe, J. P. Spatz, and E. Blasco, "4D printing of shape memory polymers: from macro to micro," *Advanced Functional Materials*, vol. 32, no. 51, pp. 2110580, 2022.
- [140] A. Lai, Z. Du, C. L. Gan, and C. A. Schuh, "Shape memory and superelastic ceramics at small scales," *Science*, vol. 341, no. 6153, pp. 1505-1508, 2013.
- [141] E. Moshkelgosha, and M. Mamivand, "Three-dimensional phase field modeling of fracture in shape memory ceramics," *International Journal of Mechanical Sciences*, vol. 204, pp. 106550, 2021.
- [142] M. A. Zaeem, N. Zhang, and M. Mamivand, "A review of computational modeling techniques in study and design of shape memory ceramics," *Computational Materials Science*, vol. 160, pp. 120-136, 2019.
- [143] T. C. Halsey, "Electrorheological fluids," *Science*, vol. 258, no. 5083, pp. 761-766, 1992.
- [144] S. Gawade, and A. Jadhav, "A review on electro rheological (ER) fluids and its applications," *International Journal of Engineering Research & Technology*, vol. 1, no. 10, pp. 1-7, 2012.
- [145] Y. Seo, "A new yield stress scaling function for electrorheological fluids," *Journal of Non-Newtonian Fluid Mechanics*, vol. 166, no. 3-4, pp. 241-243, 2011.
- [146] Q. Lu, W. J. Han, and H. J. Choi, "Smart and functional conducting polymers: application to electrorheological fluids," *Molecules*, vol. 23, no. 11, pp. 2854, 2018.
- [147] V. Chauhan, A. Kumar, and R. Sham, "Magnetorheological fluids: A comprehensive review," *Manufacturing Review*, vol. 11, pp. 6, 2024.
- [148] H. Eshgarf, A. A. Nadooshan, and A. Raisi, "An overview on properties and applications of magnetorheological fluids: Dampers, batteries, valves and brakes," *Journal of Energy Storage*, vol. 50, pp. 104648, 2022.
- [149] M. Kumar, A. Kumar, R. K. Bharti, H. Yadav, and M. Das, "A review on rheological properties of magnetorheological fluid for engineering components polishing," *Materials Today: Proceedings*, vol. 56, pp. A6-A12, 2022.
- [150] F. Narita, and M. Fox, "A review on piezoelectric, magnetostrictive, and magnetoelectric materials and device technologies for energy harvesting applications," *Advanced Engineering Materials*, vol. 20, no. 5, pp. 1700743, 2018.
- [151] P. Pei, and Y. Peng, "Constitutive modeling of magnetorheological fluids: A review," *Journal of Magnetism and Magnetic Materials*, vol. 550, pp. 169076, 2022.
- [152] X. Dong, C. Niu, and M. Qi, "Enhancement of electrorheological performance of electrorheological elastomers by improving TiO₂ particles/silicon rubber interface," *Journal of Materials Chemistry C*, vol. 4, no. 28, pp. 6806-6815, 2016.
- [153] K. Kshirsagar, P. Shah, and R. Sekhar, "Model based design in industrial automation." pp. 1-6.
- [154] M. Ahmad, "Importance of Modeling and Simulation of Materials in Research," *Journal of Modeling and Simulation of Materials*, vol. 1, no. 1, pp. 1-2, 2018.
- [155] S. Clark, A. Latz, and B. Horstmann, "A review of model-based design tools for metal-air batteries," *Batteries*, vol. 4, no. 1, pp. 5, 2018.

- [156] W. Y. Wang, J. Li, W. Liu, and Z.-K. Liu, "Integrated computational materials engineering for advanced materials: A brief review," *Computational Materials Science*, vol. 158, pp. 42-48, 2019.
- [157] Z. Chen, J. Huo, L. Hao, and J. Zhou, "Multiscale modeling and simulations of responsive polymers," *Current Opinion in Chemical Engineering*, vol. 23, pp. 21-33, 2019.
- [158] V. Singh, S. Patra, N. A. Murugan, D.-C. Toncu, and A. Tiwari, "Recent trends in computational tools and data-driven modeling for advanced materials," *Materials Advances*, vol. 3, no. 10, pp. 4069-4087, 2022.
- [159] F. L. Matthews, G. Davies, D. Hitchings, and C. Soutis, *Finite element modelling of composite materials and structures*: Elsevier, 2000.
- [160] W. B. Zimmerman, *Multiphysics modeling with finite element methods*: World Scientific Publishing Company, 2006.
- [161] L. Sabat, and C. K. Kundu, "History of finite element method: a review," *Recent Developments in Sustainable Infrastructure: Select Proceedings of ICRDSI 2019*, pp. 395-404, 2020.
- [162] P. M. Kurowski, *Finite element analysis for design engineers*: SAE International, 2022.
- [163] Z. Gronostajski, "The constitutive equations for FEM analysis," *Journal of Materials Processing Technology*, vol. 106, no. 1-3, pp. 40-44, 2000.
- [164] A. Saltelli, A. Jakeman, S. Razavi, and Q. Wu, "Sensitivity analysis: A discipline coming of age," *Environmental Modelling & Software*, vol. 146, pp. 105226, 2021.
- [165] M. Firoozan, M. Baniassadi, M. Baghani, and A. Chortos, "In silico optimization of aligned fiber electrodes for dielectric elastomer actuators," *Scientific Reports*, vol. 14, no. 1, pp. 4703, 2024.
- [166] F. Chen, K. Liu, Q. Pan, S. Chen, and X. Zhu, "An integrated design and fabrication strategy for planar soft dielectric elastomer actuators," *IEEE/ASME Transactions on Mechatronics*, vol. 26, no. 5, pp. 2629-2640, 2020.
- [167] F. M. Aliabadi, "Boundary element methods," *Encyclopedia of continuum mechanics*, pp. 182-193: Springer, 2020.
- [168] W. S. Hall, and W. Hall, *Boundary element method*: Springer, 1994.
- [169] J. H. Ferziger, M. Perić, and R. L. Street, *Computational methods for fluid dynamics*: springer, 2019.
- [170] C. R. Maliska, *Fundamentals of Computational Fluid Dynamics*: Springer, 2023.
- [171] S. Karabasov, D. Nerukh, A. Hoekstra, B. Chopard, and P. V. Coveney, "Multiscale modelling: approaches and challenges," *Philosophical Transactions of the Royal Society A: Mathematical, Physical and Engineering Sciences*, vol. 372, no. 2021, pp. 20130390, 2014.
- [172] J. Fish, G. J. Wagner, and S. Keten, "Mesoscopic and multiscale modelling in materials," *Nature materials*, vol. 20, no. 6, pp. 774-786, 2021.
- [173] A. Dequidt, S. Garruchet, B. Latour, N. Martzel, R. Blaak, E. Munch, N. Seeboth, and P. Malfreyt, "A Multiscale Modelling Approach for the Design of new Polymer Materials," *Computer Aided Chemical Engineering*, pp. 25-30: Elsevier, 2020.
- [174] B. Go, J. Kim, S. Lee, Y. Oh, J. Moon, and H. Chung, "Multiscale phase behaviors of nematic solids: a short review," *Multiscale Science and Engineering*, vol. 4, no. 1, pp. 28-36, 2022.
- [175] R. Khare, and D. S. Devarajan, "Molecular simulations of nanocolloids," *Current opinion in chemical engineering*, vol. 16, pp. 86-91, 2017.

- [176] X. Shi, and F. Tian, "Multiscale modeling and simulation of nano-carriers delivery through biological barriers—a review," *Advanced Theory and Simulations*, vol. 2, no. 1, pp. 1800105, 2019.
- [177] Y. Higuchi, "Fracture processes of crystalline polymers using coarse-grained molecular dynamics simulations," *Polymer Journal*, vol. 50, no. 8, pp. 579-588, 2018.
- [178] R. E. Rudd, and J. Q. Broughton, "Coarse-grained molecular dynamics and the atomic limit of finite elements," *Physical review B*, vol. 58, no. 10, pp. R5893, 1998.
- [179] A. Bratek-Skicki, "Towards a new class of stimuli-responsive polymer-based materials—Recent advances and challenges," *Applied Surface Science Advances*, vol. 4, pp. 100068, 2021.
- [180] P. Espanol, and P. B. Warren, "Perspective: Dissipative particle dynamics," *The Journal of chemical physics*, vol. 146, no. 15, 2017.
- [181] K. P. Santo, and A. V. Neimark, "Dissipative particle dynamics simulations in colloid and Interface science: A review," *Advances in colloid and interface science*, vol. 298, pp. 102545, 2021.
- [182] X. Li, Z. Hu, Y. Wang, C. Qin, Z. Xu, X. Chen, S. Wu, Y. Tu, and Y. Wang, "Microscopic mechanism study of the rheological behavior of non-Newtonian fluids based on dissipative particle dynamics," *Soft Matter*, vol. 19, no. 2, pp. 258-267, 2023.
- [183] R. Qin, and H. Bhadeshia, "Phase field method," *Materials science and technology*, vol. 26, no. 7, pp. 803-811, 2010.
- [184] D. Tourret, H. Liu, and J. LLorca, "Phase-field modeling of microstructure evolution: Recent applications, perspectives and challenges," *Progress in Materials Science*, vol. 123, pp. 100810, 2022.
- [185] L.-Q. Chen, and Y. Zhao, "From classical thermodynamics to phase-field method," *Progress in Materials Science*, vol. 124, pp. 100868, 2022.
- [186] I. Steinbach, "Phase-field models in materials science," *Modelling and simulation in materials science and engineering*, vol. 17, no. 7, pp. 073001, 2009.
- [187] J. Chaboche, and G. Cailletaud, "Integration methods for complex plastic constitutive equations," *Computer methods in applied mechanics and engineering*, vol. 133, no. 1-2, pp. 125-155, 1996.
- [188] M. Baghani, M. Baniassadi, and Y. Rémond, *Computational modeling of intelligent soft matter: shape memory polymers and hydrogels*: Elsevier, 2023.
- [189] D. Roylance, "Constitutive equations," *Department of Materials Science and Engineering Massachusetts Institute of Technology Cambridge, MA*, vol. 2139, 2000.
- [190] S. Wheeler, and D. Karube, "Constitutive modelling," 1996.
- [191] W.-F. Chen, and A. F. Saleeb, *Constitutive equations for engineering materials: Elasticity and modeling*: Elsevier, 2013.
- [192] L. Brinson, and M. Huang, "Simplifications and comparisons of shape memory alloy constitutive models," *Journal of intelligent material systems and structures*, vol. 7, no. 1, pp. 108-114, 1996.
- [193] V. Buljak, and G. Ranzi, *Constitutive modeling of engineering materials: Theory, computer implementation, and parameter identification*: Academic Press, 2021.
- [194] N. Şarlı, G. D. Yıldız, Y. G. Yıldız, and N. K. Yağcı, "Magnetic properties of the martensitic transformations with twinned and detwinned," *Physica B: Condensed Matter*, vol. 553, pp. 161-168, 2019.
- [195] L. C. Brinson, "One-dimensional constitutive behavior of shape memory alloys: thermomechanical derivation with non-constant material functions and redefined martensite internal variable," *Journal of intelligent material systems and structures*, vol. 4, no. 2, pp. 229-242, 1993.

- [196] C. Cisse, W. Zaki, and T. B. Zineb, "A review of constitutive models and modeling techniques for shape memory alloys," *International Journal of Plasticity*, vol. 76, pp. 244-284, 2016.
- [197] J. G. Boyd, and D. C. Lagoudas, "A thermodynamical constitutive model for shape memory materials. Part I. The monolithic shape memory alloy," *International journal of plasticity*, vol. 12, no. 6, pp. 805-842, 1996.
- [198] N. Z. Shapiro, and L. S. Shapley, "Mass action laws and the Gibbs free energy function," *Journal of the Society for Industrial and Applied Mathematics*, vol. 13, no. 2, pp. 353-375, 1965.
- [199] F. Auricchio, and L. Petrini, "A three-dimensional model describing stress-temperature induced solid phase transformations: solution algorithm and boundary value problems," *International journal for numerical methods in engineering*, vol. 61, no. 6, pp. 807-836, 2004.
- [200] W. Zaki, and Z. Moumni, "A three-dimensional model of the thermomechanical behavior of shape memory alloys," *Journal of the Mechanics and Physics of Solids*, vol. 55, no. 11, pp. 2455-2490, 2007.
- [201] W. Zaki, C. Morin, and Z. Moumni, "A simple 1D model with thermomechanical coupling for superelastic SMAs." p. 012149.
- [202] Z. Moumni, W. Zaki, Q. S. Nguyen, and W. Zhang, "Modeling of materials capable of solid–solid phase transformation. Application to the analytical solution of the semi-infinite mode III crack problem in a phase-changing solid," *International Journal of Non-Linear Mechanics*, vol. 69, pp. 146-156, 2015.
- [203] M. Zare, M. P. Prabhakaran, N. Parvin, and S. Ramakrishna, "Thermally-induced two-way shape memory polymers: Mechanisms, structures, and applications," *Chemical Engineering Journal*, vol. 374, pp. 706-720, 2019.
- [204] R. Huang, S. Zheng, Z. Liu, and T. Y. Ng, "Recent advances of the constitutive models of smart materials—Hydrogels and shape memory polymers," *International Journal of Applied Mechanics*, vol. 12, no. 02, pp. 2050014, 2020.
- [205] W. Zhao, L. Liu, X. Lan, J. Leng, and Y. Liu, "Thermomechanical constitutive models of shape memory polymers and their composites," *Applied Mechanics Reviews*, vol. 75, no. 2, pp. 020802, 2023.
- [206] Y. Li, S.-S. Guo, Y. He, and Z. Liu, "A simplified constitutive model for predicting shape memory polymers deformation behavior," *International Journal of Computational Materials Science and Engineering*, vol. 4, no. 01, pp. 1550001, 2015.
- [207] J. Diani, Y. Liu, and K. Gall, "Finite strain 3D thermoviscoelastic constitutive model for shape memory polymers," *Polymer Engineering & Science*, vol. 46, no. 4, pp. 486-492, 2006.
- [208] Z. Pan, and Z. Liu, "A novel fractional viscoelastic constitutive model for shape memory polymers," *Journal of Polymer Science Part B: Polymer Physics*, vol. 56, no. 16, pp. 1125-1134, 2018.
- [209] A. Shukla, and J. Prajapati, "On a generalization of Mittag-Leffler function and its properties," *Journal of mathematical analysis and applications*, vol. 336, no. 2, pp. 797-811, 2007.
- [210] Y. Liu, K. Gall, M. L. Dunn, A. R. Greenberg, and J. Diani, "Thermomechanics of shape memory polymers: uniaxial experiments and constitutive modeling," *International Journal of Plasticity*, vol. 22, no. 2, pp. 279-313, 2006.
- [211] Y. Li, J. Hu, and Z. Liu, "A constitutive model of shape memory polymers based on glass transition and the concept of frozen strain release rate," *International Journal of Solids and Structures*, vol. 124, pp. 252-263, 2017.

- [212] M. Freutel, H. Schmidt, L. Dürselen, A. Ignatius, and F. Galbusera, "Finite element modeling of soft tissues: material models, tissue interaction and challenges," *Clinical Biomechanics*, vol. 29, no. 4, pp. 363-372, 2014.
- [213] B. Kim, S. B. Lee, J. Lee, S. Cho, H. Park, S. Yeom, and S. H. Park, "A comparison among Neo-Hookean model, Mooney-Rivlin model, and Ogden model for chloroprene rubber," *International Journal of Precision Engineering and Manufacturing*, vol. 13, pp. 759-764, 2012.
- [214] N. Neuberger, and B. Eichinger, "Critical experimental test of the Flory-Rehner theory of swelling," *Macromolecules*, vol. 21, no. 10, pp. 3060-3070, 1988.
- [215] W. Hong, Z. Liu, and Z. Suo, "Inhomogeneous swelling of a gel in equilibrium with a solvent and mechanical load," *International Journal of Solids and Structures*, vol. 46, no. 17, pp. 3282-3289, 2009.
- [216] F. Horkay, "Polyelectrolyte gels: a unique class of soft materials," *Gels*, vol. 7, no. 3, pp. 102, 2021.
- [217] S. Zheng, and Z. Liu, "Constitutive model of salt concentration-sensitive hydrogel," *Mechanics of Materials*, vol. 136, pp. 103092, 2019.
- [218] F. Ofridam, M. Tarhini, N. Lebaz, É. Gagnière, D. Mangin, and A. Elaissari, "pH-sensitive polymers: Classification and some fine potential applications," *Polymers for Advanced Technologies*, vol. 32, no. 4, pp. 1455-1484, 2021.
- [219] R. Marcombe, S. Cai, W. Hong, X. Zhao, Y. Lapusta, and Z. Suo, "A theory of constrained swelling of a pH-sensitive hydrogel," *Soft Matter*, vol. 6, no. 4, pp. 784-793, 2010.
- [220] M. A. Haq, Y. Su, and D. Wang, "Mechanical properties of PNIPAM based hydrogels: A review," *Materials Science and Engineering: C*, vol. 70, pp. 842-855, 2017.
- [221] Z. Ding, W. Toh, J. Hu, Z. Liu, and T. Y. Ng, "A simplified coupled thermo-mechanical model for the transient analysis of temperature-sensitive hydrogels," *Mechanics of Materials*, vol. 97, pp. 212-227, 2016.
- [222] T. SURYAPRABHA, C. CHOI, Z. A. CHANDIO, L. R. MSALILWA, T. YUN, J. Y. CHEONG, and B. HWANG, "A Brief Review of Surface Modification of Carbonyl Iron Powders (CIPs) for Magnetorheological Fluid Applications," *Journal of Polymer Materials*, vol. 40, no. 3-4, pp. 191-204, 2023.
- [223] M. Osial, A. Pregowska, M. Warczak, and M. Giersig, "Magnetorheological fluids: A concise review of composition, physicochemical properties, and models," *Journal of Intelligent Material Systems and Structures*, vol. 34, no. 16, pp. 1864-1884, 2023.
- [224] X. Peng, and H. Li, "Analysis of the magnetomechanical behavior of MRFs based on micromechanics incorporating a statistical approach," *Smart Materials and structures*, vol. 16, no. 6, pp. 2477, 2007.
- [225] C. Zhao, X. Peng, J. Huang, and N. Hu, "An enhanced dipole model based micro-macro description for constitutive behavior of MRFs," *Computers Materials and Continua*, vol. 30, no. 3, pp. 219, 2012.
- [226] C.-w. Guo, F. Chen, Q.-r. Meng, and Z.-x. Dong, "Yield shear stress model of magnetorheological fluids based on exponential distribution," *Journal of magnetism and magnetic materials*, vol. 360, pp. 174-177, 2014.
- [227] Z.-D. Xu, and B.-B. Chen, "Experimental and numerical study on magnetorheological fluids based on mixing coated magnetic particles," *Journal of Materials in Civil Engineering*, vol. 28, no. 5, pp. 04015198, 2016.
- [228] F.-H. Xu, Z.-D. Xu, X.-C. Zhang, Y.-Q. Guo, and Y. Lu, "A compact experimentally validated model of magnetorheological fluids," *Journal of Vibration and Acoustics*, vol. 138, no. 1, pp. 011017, 2016.

- [229] J. Zhang, W. Song, Z. Peng, J. Gao, N. Wang, S.-B. Choi, and G.-W. Kim, "Microstructure simulation and constitutive modelling of magnetorheological fluids based on the hexagonal close-packed structure," *Materials*, vol. 13, no. 7, pp. 1674, 2020.
- [230] D. Kumar, and S. Sarangi, "Constitutive modeling of an electro-magneto-rheological fluid," *Scientific Reports*, vol. 12, no. 1, pp. 4584, 2022.
- [231] A. Albu-Schaffer, O. Eiberger, M. Grebenstein, S. Haddadin, C. Ott, T. Wimbock, S. Wolf, and G. Hirzinger, "Soft robotics," *IEEE Robotics & Automation Magazine*, vol. 15, no. 3, pp. 20-30, 2008.
- [232] A. Chen, R. Yin, L. Cao, C. Yuan, H. Ding, and W. Zhang, "Soft robotics: Definition and research issues." pp. 366-370.
- [233] S. J. A. Koh, C. Keplinger, T. Li, S. Bauer, and Z. Suo, "Dielectric elastomer generators: How much energy can be converted?," *IEEE/ASME Transactions on mechatronics*, vol. 16, no. 1, pp. 33-41, 2010.
- [234] F. Chen, and M. Y. Wang, "Simulation of networked dielectric elastomer balloon actuators," *IEEE Robotics and Automation Letters*, vol. 1, no. 1, pp. 221-226, 2016.
- [235] J. Bishop-Moser, and S. Kota, "Design and modeling of generalized fiber-reinforced pneumatic soft actuators," *IEEE Transactions on Robotics*, vol. 31, no. 3, pp. 536-545, 2015.
- [236] Y. Li, Y. Chen, Y. Yang, and Y. Wei, "Passive particle jamming and its stiffening of soft robotic grippers," *IEEE Transactions on robotics*, vol. 33, no. 2, pp. 446-455, 2017.
- [237] P. Polygerinos, Z. Wang, J. T. Overvelde, K. C. Galloway, R. J. Wood, K. Bertoldi, and C. J. Walsh, "Modeling of soft fiber-reinforced bending actuators," *IEEE Transactions on Robotics*, vol. 31, no. 3, pp. 778-789, 2015.
- [238] L. Gharavi, M. Zareinejad, and A. Ohadi, "Dynamic Finite-Element analysis of a soft bending actuator," *Mechatronics*, vol. 81, pp. 102690, 2022.
- [239] F. Xu, K. Ma, Q. Jiang, and J. Guo-Ping, "Kinematic modelling and experimental testing of a particle-jamming soft robot based on a DEM-FEM coupling method," *Bioinspiration & Biomimetics*, 2023.
- [240] W. Guo, M. Li, and J. Zhou, "Modeling programmable deformation of self-folding all-polymer structures with temperature-sensitive hydrogels," *Smart Materials and Structures*, vol. 22, no. 11, pp. 115028, 2013.
- [241] S. Haseebuddin, K. Raju, and M. Yaseen, "Applicability of the WLF equation to polyurethane polyols and film properties of their resins," *Progress in organic coatings*, vol. 30, no. 1-2, pp. 25-30, 1997.
- [242] N. M. Rudolph, A. C. Agudelo, J. C. Granada, H. E. Park, and T. A. Osswald, "WLF model for the pressure dependence of zero shear viscosity of polycarbonate," *Rheologica Acta*, vol. 55, pp. 673-681, 2016.
- [243] I. M. Ward, and J. Sweeney, *Mechanical properties of solid polymers*: John Wiley & Sons, 2012.
- [244] P. A. Cundall, and O. D. Strack, "A discrete numerical model for granular assemblies," *geotechnique*, vol. 29, no. 1, pp. 47-65, 1979.
- [245] M. Dratt, and A. Katterfeld, "Coupling of FEM and DEM simulations to consider dynamic deformations under particle load," *Granular Matter*, vol. 19, no. 3, pp. 49, 2017.
- [246] A. Jiang, T. Ranzani, G. Gerboni, L. Lekstutyte, K. Althoefer, P. Dasgupta, and T. Nanayakkara, "Robotic granular jamming: Does the membrane matter?," *Soft Robotics*, vol. 1, no. 3, pp. 192-201, 2014.

- [247] Y. Wei, Y. Chen, Y. Yang, and Y. Li, "A soft robotic spine with tunable stiffness based on integrated ball joint and particle jamming," *Mechatronics*, vol. 33, pp. 84-92, 2016.
- [248] J. R. Amend, E. Brown, N. Rodenberg, H. M. Jaeger, and H. Lipson, "A positive pressure universal gripper based on the jamming of granular material," *IEEE transactions on robotics*, vol. 28, no. 2, pp. 341-350, 2012.
- [249] A. Jiang, G. Xynogalas, P. Dasgupta, K. Althoefer, and T. Nanayakkara, "Design of a variable stiffness flexible manipulator with composite granular jamming and membrane coupling." pp. 2922-2927.
- [250] J. Amend, N. Cheng, S. Fakhouri, and B. Culley, "Soft robotics commercialization: Jamming grippers from research to product," *Soft robotics*, vol. 3, no. 4, pp. 213-222, 2016.
- [251] A. H. Karoyo, and L. D. Wilson, "A review on the design and hydration properties of natural polymer-based hydrogels," *Materials*, vol. 14, no. 5, pp. 1095, 2021.
- [252] H. Yang, W. R. Leow, T. Wang, J. Wang, J. Yu, K. He, D. Qi, C. Wan, and X. Chen, "3D printed photoresponsive devices based on shape memory composites," *Advanced Materials*, vol. 29, no. 33, pp. 1701627, 2017.
- [253] F. Ongaro, S. Scheggi, C. Yoon, F. v. den Brink, S. H. Oh, D. H. Gracias, and S. Misra, "Autonomous planning and control of soft untethered grippers in unstructured environments," *Journal of micro-bio robotics*, vol. 12, pp. 45-52, 2017.
- [254] H. Mazaheri, and A. Khodabandehloo, "Behavior of an FG temperature-responsive hydrogel bilayer: Analytical and numerical approaches," *Composite Structures*, vol. 301, pp. 116203, 2022.
- [255] Z. Chen, Y. Li, and Q. Li, "Hydrogel-driven origami metamaterials for tunable swelling behavior," *Materials & Design*, vol. 207, pp. 109819, 2021.
- [256] J. Zheng, P. Xiao, X. Le, W. Lu, P. Théato, C. Ma, B. Du, J. Zhang, Y. Huang, and T. Chen, "Mimosa inspired bilayer hydrogel actuator functioning in multi-environments," *Journal of Materials Chemistry C*, vol. 6, no. 6, pp. 1320-1327, 2018.
- [257] S. G. Fitzgerald, G. W. Delaney, and D. Howard, "A Review of Jamming Actuation in Soft Robotics." p. 104.
- [258] T. Beléndez, C. Neipp, and A. Beléndez, "Large and small deflections of a cantilever beam," *European journal of physics*, vol. 23, no. 3, pp. 371, 2002.
- [259] L. Chen, "An integral approach for large deflection cantilever beams," *International Journal of Non-Linear Mechanics*, vol. 45, no. 3, pp. 301-305, 2010.
- [260] R. Khandan, S. Noroozi, P. Sewell, and J. Vinney, "The development of laminated composite plate theories: a review," *Journal of Materials Science*, vol. 47, no. 16, pp. 5901-5910, 2012.
- [261] P. White, S. Latscha, and M. Yim, "Modeling of a dielectric elastomer bender actuator." pp. 245-269.
- [262] Z. Ding, Z. Liu, J. Hu, S. Swaddiwudhipong, and Z. Yang, "Inhomogeneous large deformation study of temperature-sensitive hydrogel," *International Journal of Solids and Structures*, vol. 50, no. 16-17, pp. 2610-2619, 2013.
- [263] M. Dratt, and A. Katterfeld, "Coupling of FEM and DEM simulations to consider dynamic deformations under particle load," *Granular Matter*, vol. 19, no. 3, pp. 1-15, 2017.
- [264] J. R. Williams, E. Perkins, and B. Cook, "A contact algorithm for partitioning N arbitrary sized objects," *Engineering Computations*, 2004.
- [265] M. Zang, W. Gao, and Z. Lei, "A contact algorithm for 3D discrete and finite element contact problems based on penalty function method," *Computational Mechanics*, vol. 48, no. 5, pp. 541-550, 2011.

- [266] H. A. Navarro, and M. P. de Souza Braun, "Determination of the normal spring stiffness coefficient in the linear spring–dashpot contact model of discrete element method," *Powder technology*, vol. 246, pp. 707-722, 2013.
- [267] K. Han, D. Peric, D. Owen, and J. Yu, "A combined finite/discrete element simulation of shot peening processes–Part II: 3D interaction laws," *Engineering Computations*, 2000.
- [268] L. Marechal, P. Balland, L. Lindenroth, F. Petrou, C. Kontovounisios, and F. Bello, "Toward a common framework and database of materials for soft robotics," *Soft robotics*, vol. 8, no. 3, pp. 284-297, 2021.
- [269] P. J. Flory, and J. Rehner Jr, "Statistical mechanics of cross-linked polymer networks II. Swelling," *The journal of chemical physics*, vol. 11, no. 11, pp. 521-526, 1943.
- [270] P. J. Flory, "Thermodynamics of high polymer solutions," *The Journal of chemical physics*, vol. 10, no. 1, pp. 51-61, 1942.
- [271] M. L. Huggins, "A revised theory of high polymer solutions," *Journal of the American Chemical Society*, vol. 86, no. 17, pp. 3535-3540, 1964.
- [272] F. Afroze, E. Nies, and H. Berghmans, "Phase transitions in the system poly (N-isopropylacrylamide)/water and swelling behaviour of the corresponding networks," *Journal of Molecular Structure*, vol. 554, no. 1, pp. 55-68, 2000.
- [273] W. Hong, X. Zhao, J. Zhou, and Z. Suo, "A theory of coupled diffusion and large deformation in polymeric gels," *Journal of the Mechanics and Physics of Solids*, vol. 56, no. 5, pp. 1779-1793, 2008.
- [274] R. S. Rivlin, "Large elastic deformations of isotropic materials IV. Further developments of the general theory," *Philosophical transactions of the royal society of London. Series A, Mathematical and physical sciences*, vol. 241, no. 835, pp. 379-397, 1948.
- [275] Y. Li, Y. Chen, Y. Yang, and Y. Li, "Soft robotic grippers based on particle transmission," *IEEE/ASME Transactions on Mechatronics*, vol. 24, no. 3, pp. 969-978, 2019.
- [276] K. S. Oh, J. S. Oh, H. S. Choi, and Y. C. Bae, "Effect of cross-linking density on swelling behavior of NIPA gel particles," *Macromolecules*, vol. 31, no. 21, pp. 7328-7335, 1998.
- [277] A. Suzuki, and T. Ishii, "Phase coexistence of neutral polymer gels under mechanical constraint," *The Journal of chemical physics*, vol. 110, no. 4, pp. 2289-2296, 1999.
- [278] E. R. Dougherty, S. Kim, and Y. Chen, "Coefficient of determination in nonlinear signal processing," *Signal Processing*, vol. 80, no. 10, pp. 2219-2235, 2000.
- [279] H. Wang, Z. Chen, and S. Zuo, "Flexible manipulator with low-melting-point alloy actuation and variable stiffness," *Soft Robotics*, vol. 9, no. 3, pp. 577-590, 2022.
- [280] Y. Hao, J. Gao, Y. Lv, and J. Liu, "Low melting point alloys enabled stiffness tunable advanced materials," *Advanced Functional Materials*, vol. 32, no. 25, pp. 2201942, 2022.
- [281] Q. Chen, D. Schott, and J. Jovanova, "Conceptual design of a novel particle-based soft grasping gripper," *Journal of Mechanisms and Robotics*, vol. 16, no. 5, 2024.
- [282] P. Jiang, Y. Yang, M. Z. Chen, and Y. Chen, "A variable stiffness gripper based on differential drive particle jamming," *Bioinspiration & biomimetics*, vol. 14, no. 3, pp. 036009, 2019.
- [283] E. Sachyani Keneth, A. Kamyshny, M. Totaro, L. Beccai, and S. Magdassi, "3D printing materials for soft robotics," *Advanced Materials*, vol. 33, no. 19, pp. 2003387, 2021.
- [284] M. P. Lutolf, "Spotlight on hydrogels," *Nature materials*, vol. 8, no. 6, pp. 451-453, 2009.

- [285] Y. Mao, Z. Ding, C. Yuan, S. Ai, M. Isakov, J. Wu, T. Wang, M. L. Dunn, and H. J. Qi, "3D printed reversible shape changing components with stimuli responsive materials," *Scientific reports*, vol. 6, no. 1, pp. 24761, 2016.
- [286] J. Duan, X. Liang, K. Zhu, J. Guo, and L. Zhang, "Bilayer hydrogel actuators with tight interfacial adhesion fully constructed from natural polysaccharides," *Soft Matter*, vol. 13, no. 2, pp. 345-354, 2017.
- [287] Y. Takashima, S. Hatanaka, M. Otsubo, M. Nakahata, T. Kakuta, A. Hashidzume, H. Yamaguchi, and A. Harada, "Expansion-contraction of photoresponsive artificial muscle regulated by host-guest interactions," *Nature communications*, vol. 3, no. 1, pp. 1270, 2012.
- [288] E. Palleau, D. Morales, M. D. Dickey, and O. D. Velev, "Reversible patterning and actuation of hydrogels by electrically assisted ionoprinting," *Nature communications*, vol. 4, no. 1, pp. 2257, 2013.
- [289] Q. Shen, S. Trabia, T. Stalbaum, V. Palmre, K. Kim, and I.-K. Oh, "A multiple-shape memory polymer-metal composite actuator capable of programmable control, creating complex 3D motion of bending, twisting, and oscillation," *Scientific reports*, vol. 6, no. 1, pp. 24462, 2016.
- [290] B. Aksoy, and H. Shea, "Multistable shape programming of variable-stiffness electromagnetic devices," *Science Advances*, vol. 8, no. 21, pp. eabk0543, 2022.
- [291] M. Y. Khalid, Z. U. Arif, A. Al Rashid, S. M. Z. S. Bukhari, M. Hossain, and M. Koç, "Shape-memory and self-healing properties of sustainable cellulosic nanofibers-based hybrid materials for novel applications," *Giant*, pp. 100299, 2024.
- [292] F. Gandhi, and S.-G. Kang, "Beams with controllable flexural stiffness," *Smart Materials and Structures*, vol. 16, no. 4, pp. 1179, 2007.
- [293] W. Wang, C. Y. Yu, P. A. Abrego Serrano, and S.-H. Ahn, "Shape memory alloy-based soft finger with changeable bending length using targeted variable stiffness," *Soft robotics*, vol. 7, no. 3, pp. 283-291, 2020.
- [294] F. Ganji, F. S. Vasheghani, and F. E. Vasheghani, "Theoretical description of hydrogel swelling: a review," 2010.
- [295] S. M. Flory, T. J. Phillips Jr, R. E. Reidenbach, and D. P. Robin, "A multidimensional analysis of selected ethical issues in accounting," *Accounting Review*, pp. 284-302, 1992.
- [296] C. Huggins, R. Stevens, and C. V. Hodges, "Studies on prostatic cancer: II. The effects of castration on advanced carcinoma of the prostate gland," *Archives of surgery*, vol. 43, no. 2, pp. 209-223, 1941.
- [297] M. Y. Khalid, Z. U. Arif, R. Noroozi, M. Hossain, S. Ramakrishna, and R. Umer, "3D/4D printing of cellulose nanocrystals-based biomaterials: Additives for sustainable applications," *International Journal of Biological Macromolecules*, pp. 126287, 2023.
- [298] J. Wang, R. Kean, J. Randall, and D. Giles, "The effect of crystallinity on the rheological behavior of poly (lactide)," *International Journal of Polymer Analysis and Characterization*, vol. 4, no. 5, pp. 393-405, 1998.
- [299] M. Al-Rubaii, T. Pinto, C. Qian, and X. Tan, "Soft actuators with stiffness and shape modulation using 3D-printed conductive polylactic acid material," *Soft robotics*, vol. 6, no. 3, pp. 318-332, 2019.
- [300] G. M. Eichenbaum, P. F. Kiser, A. V. Dobrynin, S. A. Simon, and D. Needham, "Investigation of the swelling response and loading of ionic microgels with drugs and proteins: The dependence on cross-link density," *Macromolecules*, vol. 32, no. 15, pp. 4867-4878, 1999.

- [301] H. J. Qi, T. D. Nguyen, F. Castro, C. M. Yakacki, and R. Shandas, "Finite deformation thermo-mechanical behavior of thermally induced shape memory polymers," *Journal of the Mechanics and Physics of Solids*, vol. 56, no. 5, pp. 1730-1751, 2008.
- [302] R. Casati, F. Passaretti, and A. Tuissi, "Effect of electrical heating conditions on functional fatigue of thin NiTi wire for shape memory actuators," *Procedia Engineering*, vol. 10, pp. 3423-3428, 2011.
- [303] R. Bogue, "Shape-memory materials: a review of technology and applications," *Assembly Automation*, vol. 29, no. 3, pp. 214-219, 2009.
- [304] M. Bashir, C. F. Lee, and P. Rajendran, "Shape memory materials and their applications in aircraft morphing: an introspective study," *ARPJ. Eng. Appl. Sci*, vol. 12, no. 19, pp. 5434-5446, 2017.
- [305] A. Villanueva, C. Smith, and S. Priya, "A biomimetic robotic jellyfish (Robojelly) actuated by shape memory alloy composite actuators," *Bioinspiration & biomimetics*, vol. 6, no. 3, pp. 036004, 2011.
- [306] X. Lan, Y. Liu, H. Lv, X. Wang, J. Leng, and S. Du, "Fiber reinforced shape-memory polymer composite and its application in a deployable hinge," *Smart Materials and Structures*, vol. 18, no. 2, pp. 024002, 2009.
- [307] C. Tang, T. Wang, W. Huang, L. Sun, and X. Gao, "Temperature sensors based on the temperature memory effect in shape memory alloys to check minor over-heating," *Sensors and Actuators A: Physical*, vol. 238, pp. 337-343, 2016.
- [308] K. Kuribayashi, "Improvement of the response of an SMA actuator using a temperature sensor," *The International Journal of Robotics Research*, vol. 10, no. 1, pp. 13-20, 1991.
- [309] F. Largilliere, V. Verona, E. Coevoet, M. Sanz-Lopez, J. Dequidt, and C. Duriez, "Real-time control of soft-robots using asynchronous finite element modeling." pp. 2550-2555.
- [310] O. Goury, and C. Duriez, "Fast, generic, and reliable control and simulation of soft robots using model order reduction," *IEEE Transactions on Robotics*, vol. 34, no. 6, pp. 1565-1576, 2018.
- [311] Z. Wang, X. Zu, X. Feng, S. Zhu, J. Bao, and L. Wang, "Characteristics of two-way shape memory TiNi springs driven by electrical current," *Materials & design*, vol. 25, no. 8, pp. 699-703, 2004.
- [312] M. Behl, M. Y. Razzaq, and A. Lendlein, "Multifunctional shape-memory polymers," *Advanced materials*, vol. 22, no. 31, pp. 3388-3410, 2010.
- [313] W. Huang, and W. Toh, "Training two-way shape memory alloy by reheat treatment," *Journal of materials science letters*, vol. 19, no. 17, pp. 1549-1550, 2000.
- [314] E. M. Gorostiza, J. L. Lázaro Galilea, F. J. Meca Meca, D. Salido Monzú, F. Espinosa Zapata, and L. Pallarés Puerto, "Infrared sensor system for mobile-robot positioning in intelligent spaces," *Sensors*, vol. 11, no. 5, pp. 5416-5438, 2011.
- [315] P. Adesso, M. Longo, R. Montone, R. Restaino, and G. Vivone, "Interpolation and combination rules for the temporal and spatial enhancement of SEVIRI and MODIS thermal image sequences," *International Journal of Remote Sensing*, vol. 38, no. 7, pp. 1889-1911, 2017.
- [316] C. W. Chen, J. Luo, and K. J. Parker, "Image segmentation via adaptive K-mean clustering and knowledge-based morphological operations with biomedical applications," *IEEE transactions on image processing*, vol. 7, no. 12, pp. 1673-1683, 1998.

Nomenclature

Symbol	Unit	Definition
C_1, C_2	-	material constant
C_{A^-}	mol/m ³	fixed charge group concentration
C_{AH}	mol/m ³	associated acidic group concentration
C_{H^+}, C_+, C_-	mol/m ³	nominal concentrations of hydrogen ions, mobile cations, anions
c_{H^+}, c_+, c_-	mol/m ³	true concentrations of cations, anions and hydrogen ions inside
$\bar{c}_{H^+}, \bar{c}_+, \bar{c}_-$	mol/m ³	true concentrations of cations, anions and hydrogen ions outside
C_s	mol/m ³	concentration of solvent
d_i	mm	diameter of different hydrogel element
E_n	MPa	instantaneous modulus
E_i	MPa	elastic modulus
e'	-	dimensionless number represent length change
F_{ik}	-	deformation gradient of the network
F_E	N	external force
f	-	number of acidic groups on a polymer chain
K_a	-	constant of acidic dissociation
h	mm	height of each block unit

k	$\text{J}\cdot\text{K}^{-1}$	Boltzmann constant
L_h, L_v	-	total layers in horizontal direction, total layers in vertical direction
L_s	mm	distance from the top end to the bending point
N	-	the polymer chains number divided by the volume of the dry network
N_A	mol^{-1}	Avogadro number
v_s	m^3	single molecule volume
S_a	$\text{N}\cdot\text{mm}/\text{rad}$	bending stiffness
T	K	absolute temperature
T_g	K	glass transition temperature
T_r	K	reference temperature
t	S	time
P_h, P_v	mm	The lengths of the structure in horizontal and vertical direction
W	J/m^3	free energy density
μ_s	J/mol	chemical potential
Π_{sol}, Π_{ion}	Pa	osmotic pressures from polymer-solvent, ion-solvent mixtures
ε_0	-	strain at the initial time
ψ^e	-	thermos-elastic free energy density
ξ_t	mm	diameter difference
ξ_d	mm	thickness difference between two surface
τ_T	K	transformation temperature
θ	deg	rotational angle caused by the external moment
φ	deg	bending angle

Acknowledgements

As I reach the culmination of my PhD journey, I reflect on the many people who have supported and guided me throughout this process. This dissertation is a testament to years of effort and the contributions of the individuals who stood by me.

First and foremost, I would like to express my sincerest gratitude to my promotor, Prof. dr. ir. D. L. Schott. Your unconditional support, intellectual guidance, and faith in my abilities have been in shaping this work. Your vast knowledge and meticulous attention to detail set a standard that I have strived to meet throughout my research. Your encouragement to think critically and break boundaries has not only enhanced the quality of this dissertation but has also profoundly influenced my academic and professional development. Thank you for believing in me and for providing a steady anchor during this challenging journey.

I also want to sincerely thank my daily supervisor, Dr. J. Jovanova, for the incredible support and guidance throughout my research. Your knowledge and patience made a big difference, and I truly appreciated how you were always available to help whenever I needed it. Your flexible approach to our daily discussions and the constructive feedback you provided gave me confidence and a sense of security as I worked through challenges. You not only helped me understand the technical and complex aspects of my research but also taught me how to manage the ups and downs of PhD life with a steady mind. Your genuine interest in my progress and dedication to scientific work inspired me to keep pushing forward. I feel very fortunate to have had your guidance and support every step of the way, and I am deeply grateful for all you have done for me.

I am deeply grateful to my parents for their unconditional love and support. Mom and Dad, your belief in me and the values you instilled in me have been the foundation of everything I've accomplished. Your encouragement and the sacrifices you made made this achievement possible, and I dedicate this work to you. To my girlfriend, Yaxuan, thank you for your love, patience, and understanding. Your constant support and encouragement have been my strength

throughout this journey. You stood by me through every challenge, and I am so thankful to have you in my life.

To my colleagues in the Adaptive Metastructures, Mechanisms, and Machines research group—Ana, Vera, Hao, Christof, Chamod, Amy, and Zhaorui—thank you for your collaboration and the many thought-provoking discussions that helped shape this work. To my colleagues in the Machines & Materials Interactions research group—Marcel, Raisa, Wenhua, Marc, Ahmed, Hesam, and Javier—thank you for your support and companionship. Your teamwork and friendship have been truly appreciated.

I want to thank the secretaries, especially Gracia, Emiel, Patty, Pauline, and Tessa, as well as the managers and secretaries of the M&TT department, for their daily support and for organizing activities during the holidays. I also want to thank the technical support team, Vittorio, Bart, and Ed, for their help with my daily experiments.

I would also like to thank my master’s supervisors, Prof. Shidong Fan, and Dr. Ting Xiong, for guiding me and supporting my journey toward pursuing a PhD. I want to express my gratitude to my close friends, Ruihan, Shaoli, Haoran, Guangyuan, and Longji. Your belief in me and your encouragement have been a big source of motivation for this achievement.

I’m thankful to my colleagues Xiaohuan, Mingxin, Zhe, Jian, Xin, Rongxin, Yimeng, Pan, Xiuhan, Nikos, Simeon, Bin, and Dridri for the fun lunches and activities we enjoyed together. I also want to thank my friends Haowen, Yifeng, Dequan, Shihao, Yiran, Ding, Feng, and everyone in the Punch basketball club. Playing basketball with you every week has been one of the best parts of my time here.

Finally, I want to thank everyone who contributed to my PhD experience, directly or indirectly. From professors and mentors to administrative staff, your support has meant so much. I am also grateful to the researchers whose work provided the foundation for my own. This dissertation is the result of many contributions, and I feel honored to be part of this academic community. I dedicate this dissertation to everyone who believed in me. Thank you for being part of my journey.

March 20, 2025, Qianyi Chen, Delft

Curriculum Vitae

Qianyi Chen received the B.Sc. degree in Oil and Gas Storage and Transportation Engineering at Wuhan University of Technology, Wuhan, China, from September 2013 to June 2017. At the same year, he started his master in Traffic and Transportation Engineering at the Key Laboratory of Water Transportation Facility Maintenance and Safety, Wuhan University of Technology, China, from September 2017 to June 2020. Qianyi Chen started his PhD research in April 2021 at the Department of Maritime Technology and Transport, Faculty of Mechanical Engineering, Delft University of Technology, the Netherlands, under the supervision of Prof. dr. ir. D. L. Schott and the co-promotor Dr. J. Jovanova. His research interests include finite element method, numerical modelling, morphology, soft robotics, and smart materials.

Publications

Journal papers

1. Chen Q, Schott D, Jovanova J. Model-Based Design of Variable Stiffness Soft Gripper Actuated by Smart Hydrogels. *Soft Robotics*. 2024 April.
2. Chen QY, He YP, Xiong T, Li MZ, Liu WH. Study on the dynamic characteristics of the overflow advection and diffusion of trailing suction hopper dredgers based on CFD. *Ocean Engineering*. 2022 May 15;252:111263.
3. Chen Q, Xiong T, Zhang X, Jiang P. Study of the hydraulic transport of non-spherical particles in a pipeline based on the CFD-DEM. *Engineering Applications of Computational Fluid Mechanics*. 2020 Jan 1;14(1):53-69.
4. Chen Q, Schott D, Jovanova J. Model-based design of a mechanically intelligent shape-morphing structure. *Scientific Reports* 2024 Oct.10.1038/s41598-024-74379-4

5. Chen Q, Kalpoe T, Jovanova J. Design of mechanically intelligent structures: Review of modeling stimuli-responsive materials for adaptive structures. *Heliyon*. 2024 Jul 8.
6. Chen Q, Schott D, Jovanova J. Conceptual Design of a Novel Particle-Based Soft Grasping Gripper. *Journal of Mechanisms and Robotics*. 2024 May 1;16(5).

Conference papers

1. Chen Q, Schott D, Jovanova J. Are active soft particles suitable for particle jamming actuators?. In 2023 IEEE International Conference on Soft Robotics (RoboSoft) 2023 Apr 3 (pp. 1-6). IEEE.
2. Chen Q, Kalpoe T, Jovanova J. Modelling Programmable Deformation of Particle-Based Structure with Smart Hydrogels. In 2024 6th International Conference on Reconfigurable Mechanisms and Robots (ReMAR) 2024 Jun 23 (pp. 633-639). IEEE.

Samenvatting

Zachte robotica, een multidisciplinair ingenieursveld, is ontstaan uit de vraag naar flexibiliteit en aanpassingsvermogen om taken uit te voeren in ongestructureerde omgevingen. Er blijven echter nog steeds aanzienlijke uitdagingen bestaan, waaronder het conflict tussen stijfheid en flexibiliteit, multifunctionaliteit en adaptief vermogen. Het concept van mechanische intelligentie, het direct integreren van intelligentie in structuren door middel van hun ontwerp, biedt een alternatieve manier om deze beperkingen aan te pakken, naast complexe assemblages en controlesystemen. Om mechanische intelligentie te bereiken, biedt het integreren van slimme materialen in morphing-structuren een potentiële ontwerpbenadering. Er is echter een gebrek aan een ontwerpkader om meerdere slimme materialen, stimuli en structureel ontwerp te integreren om de ontwikkeling van mechanische intelligentie te ondersteunen. Daarom is het onderzoeksdoel van dit proefschrift om een op modellen gebaseerd ontwerpkader te ontwikkelen voor mechanisch intelligente morphing-structuren. Dit zal het mogelijk maken om slimme materialen te integreren in zachte robotica voor het uitvoeren van adaptieve functies.

Slimme materialen hebben een aanzienlijk potentieel voor geavanceerde technische toepassingen vanwege hun vermogen om te reageren op externe stimuli zoals temperatuur, licht, druk, elektrische en magnetische velden. Deze materialen kunnen een breed scala aan aanpasbaar gedrag vertonen dat functionaliteiten mogelijk maakt zoals variabele stijfheid en/of op maat gemaakte vervorming. De niet-lineaire aard van slimme materialen en hun complexe wisselwerking met de omgeving vormen echter uitdagingen bij het nauwkeurig modelleren van deze interactie. Modelleringsbenaderingen kunnen bijdragen aan nieuwe oplossingen door het niet-lineaire gedrag van slimme materialen te beschrijven. Deze inzichten vormen de basis voor ontwerpkaders die het ontwerp van mechanisch intelligente structuren mogelijk maken.

In dit proefschrift wordt een modelgebaseerd ontwerpkader voor het ontwerp van mechanisch intelligente morphing-structuren voorgesteld. Het kader integreert slimme materiaaleigenschappen, structurele geometrie en externe stimuli in modulaire "bouwstenen". Deze bouwstenen worden voorgesteld als de fundamenten voor het creëren van adaptieve morphing-structuren. Numerieke methoden, waaronder de eindige-elementenmethode (FEM),

de discrete-elementenmethode (DEM) en de koppelingsmethode, worden gebruikt om interacties tussen materialen en externe stimuli te simuleren. Met behulp van dit kader werd een conceptueel ontwerp voor buigende bouwstenen met variabele stijfheid ontwikkeld. Door stijve deeltjes of slimme hydrogels te gebruiken, zijn deze buigende bouwstenen in staat tot omkeerbare vervormingen en variërende stijfheid. De bevindingen tonen aan dat grotere buighoeken in het op stijve deeltjes gebaseerde ontwerp worden bereikt door de deeltjesdiameterverhouding en membraanstijfheid te vergroten, terwijl in het op hydrogeldeeltjes gebaseerde ontwerp grotere buighoeken worden bereikt door meer deeltjeslagen toe te voegen of de membraanstijfheid te verlagen. Bovendien resulteert het op stijve deeltjes gebaseerde ontwerp in een zesvoudige toename van de stijfheid. Voor het op hydrogel gebaseerde ontwerp werd, in combinatie met legeringstrips met een laag smeltpunt, een twintigvoudige toename van de stijfheid aangetoond.

Voortbouwend op het conceptuele ontwerp werd de integratie van meerdere slimme materialen in één bouwsteen gerealiseerd via het modelgebaseerde ontwerpkader, waardoor de morphing-structuur zelfactuatie en adaptief gedrag kan vertonen. Door pH-gevoelige hydrogels en vormgeheugenpolymeren (SMP's) te combineren, worden de bouwstenen samengevoegd tot een morphing-structuur. In deze morphing-structuur wordt zelfactuatie geactiveerd door een pH toename, terwijl de stijfheid wordt verhoogd door de temperatuur te verlagen. De structuur is in staat tot het uitvoeren van verschillende vervormingen, waaronder buigen, krullen en verlengen, waarbij de geometrische parameters van het SMP-frame een belangrijke rol spelen in dit gedrag. Bovendien neemt de buigstijfheid met een factor tien toe in vergelijking met de rubberachtige toestand wanneer de SMP overgaat naar zijn glasachtige toestand.

Voortbouwend op het ontwerp van meerdere slimme materialen is een geïntegreerd systeem ontwikkeld om collaboratieve werking mogelijk te maken door een thermisch controlesysteem te integreren in een op een structuur met vormgeheugen. Dit systeem maakt gecoördineerde reacties op dezelfde externe stimulus mogelijk. De structuur, die is voorzien van veren van vormgeheugenlegering (SMA) en een SMP-frame, bereikt zelfactuatie en stijfheidsvariatie door de vormgeheugeneffecten. Het geïntegreerde thermische controlesysteem stelt de materialen in staat om te reageren op temperatuurveranderingen, waardoor de morphing-structuur een verschillende acties kan uitvoeren met consistente werking. Met behulp van dit geïntegreerde systeem kan de morphing-structuur een reeks bewegingen ondergaan, waaronder buigen, stijfheidsverbetering en herstel, allemaal binnen een continue cyclus van 110 seconden.

Concluderend toont het voorgestelde modelgebaseerde ontwerpkader de haalbaarheid voor het ontwikkelen van mechanisch intelligente morphingstructuren. Het kader integreert systematisch slimme materialen en structurele geometrieën in de morphingstructuren die worden aangestuurd door externe stimuli, waardoor zelfactuatie en adaptieve functionaliteit mogelijk worden. Bovendien vergroot de gesynchroniseerde werking van het geïntegreerde systeem het potentieel voor praktische toepassingen van mechanisch intelligente morphingstructuren op het gebied van zachte robotica. Toekomstig werk zou zich moeten richten op het verbeteren van de nauwkeurigheid van de numerieke modellering en het ontwikkelen van een dynamisch controlesysteem voor stabiliteit. Bovendien is een

vermoeidheidsanalyse essentieel voor het verbeteren van de levensduur in industriële toepassingen.

TRAIL Thesis Series

The following list contains the most recent dissertations in the TRAIL Thesis Series. For a complete overview of more than 400 titles, see the TRAIL website: www.rsTRAIL.nl.

The TRAIL Thesis Series is a series of the Netherlands TRAIL Research School on transport, infrastructure and logistics.

Chen, Q., *Towards Mechanical Intelligence in Soft Robotics: Model-based design of mechanically intelligent structures*, T2025/10, April 2025, TRAIL Thesis Series, the Netherlands

Eftekhar, Z., *Exploring the Spatial and Temporal Patterns in Travel Demand: A data-driven approach*, T2025/9, June 2025, TRAIL Thesis Series, the Netherlands

Reddy, N., *Human Driving Behavior when Interacting with Automated Vehicles and the Implications on Traffic Efficiency*, T2025/8, May 2025, TRAIL Thesis Series, the Netherlands

Durand, A., *Lost in Digitalisation? Navigating public transport in the digital era*, T2025/7, May 2025, TRAIL Thesis Series, the Netherlands

Dong, Y., *Safe, Efficient, and Socially Compliant Automated Driving in Mixed Traffic: Sensing, Anomaly Detection, Planning and Control*, T2025/6, May 2025, TRAIL Thesis Series, the Netherlands

Droffelaar, I.S. van, *Simulation-optimization for Fugitive Interception*, T2025/5, May 2025, TRAIL Thesis Series, the Netherlands

Fan, Q., *Fleet Management Optimisation for Ride-hailing Services: from mixed traffic to fully automated environments*, T2025/4, April 2025, TRAIL Thesis Series, the Netherlands

Hagen, L. van der, *Machine Learning for Time Slot Management in Grocery Delivery*, T2025/3, March 2025, TRAIL Thesis Series, the Netherlands

- Schilt, I.M. van, *Reconstructing Illicit Supply Chains with Sparse Data: a simulation approach*, T2025/2, January 2025, TRAIL Thesis Series, the Netherlands
- Ruijter, A.J.F. de, *Two-Sided Dynamics in Ridesourcing Markets*, T2025/1, January 2025, TRAIL Thesis Series, the Netherlands
- Fang, P., *Development of an Effective Modelling Method for the Local Mechanical Analysis of Submarine Power Cables*, T2024/17, December 2024, TRAIL Thesis Series, the Netherlands
- Zattoni Scroccaro, P., *Inverse Optimization Theory and Applications to Routing Problems*, T2024/16, October 2024, TRAIL Thesis Series, the Netherlands
- Kapousizis, G., *Smart Connected Bicycles: User acceptance and experience, willingness to pay and road safety implications*, T2024/15, November 2024, TRAIL Thesis Series, the Netherlands
- Lyu, X., *Collaboration for Resilient and Decarbonized Maritime and Port Operations*, T2024/14, November 2024, TRAIL Thesis Series, the Netherlands
- Nicolet, A., *Choice-Driven Methods for Decision-Making in Intermodal Transport: Behavioral heterogeneity and supply-demand interactions*, T2024/13, November 2024, TRAIL Thesis Series, the Netherlands
- Kougiatsos, N., *Safe and Resilient Control for Marine Power and Propulsion Plants*, T2024/12, November 2024, TRAIL Thesis Series, the Netherlands
- Uijtdewilligen, T., *Road Safety of Cyclists in Dutch Cities*, T2024/11, November 2024, TRAIL Thesis Series, the Netherlands
- Liu, X., *Distributed and Learning-based Model Predictive Control for Urban Rail Transit Networks*, T2024/10, October 2024, TRAIL Thesis Series, the Netherlands
- Clercq, G. K. de, *On the Mobility Effects of Future Transport Modes*, T2024/9, October 2024, TRAIL Thesis Series, the Netherlands
- Dreischerf, A.J., *From Caveats to Catalyst: Accelerating urban freight transport sustainability through public initiatives*, T2024/8, September 2024, TRAIL Thesis Series, the Netherlands
- Zohoori, B., *Model-based Risk Analysis of Supply Chains for Supporting Resilience*, T2024/7, October 2024, TRAIL Thesis Series, the Netherlands
- Poelman, M.C., *Predictive Traffic Signal Control under Uncertainty: Analyzing and Reducing the Impact of Prediction Errors*, T2024/6, October 2024, TRAIL Thesis Series, the Netherlands
- Berge, S.H., *Cycling in the age of automation :Enhancing cyclist interaction with automated vehicles through human-machine interfaces*, T2024/5, September 2024, TRAIL Thesis Series, the Netherlands
- Wu, K., *Decision-Making and Coordination in Green Supply Chains with Asymmetric Information*, T2024/4, July 2024, TRAIL Thesis Series, the Netherlands



TRAIL

Summary

This thesis presents a model-based design framework for incorporating mechanical intelligence into soft robotics. By integrating smart materials with morphing structures, the framework enhances the adaptability of soft robotic systems. The embedded mechanical intelligence enables the synchronization of multiple smart materials, facilitating self-actuation and customized deformations. This approach advances the development of autonomous and adaptive soft robotic systems.

About the Author

Qianyi Chen began his Ph.D. research in 2021 at the Department of Maritime and Transportation Technology at Delft University of Technology, Netherlands. Before that, he earned his M.Sc. degree from Wuhan University of Technology, China, in 2020.

TRAIL Research School ISBN 978-90-5584-365-7



Radboud University



rijksuniversiteit
 groningen



UNIVERSITY OF TWENTE.



Technische Universiteit
 Eindhoven
 University of Technology

Invitation

You are cordially invited to attend the public defence of my Ph.D. dissertation titled:

Towards Mechanical Intelligence In Soft Robotics: Model-based Design of Mechanically Intelligent Structures

The defence will take place on Wednesday, 30 April 2025 at 10:00 in the Senaatszaal of the Aula Congress Centre at Delft University of Technology, Mekelweg 5, Delft.

Prior to the defence, at 09:30, I will give a brief presentation about my research.

A reception will be held directly after the defence.

Qianyi Chen

陈芊屹

Q.Chen-5@tudelft.nl
